



AFRL-RY-WP-TR-2009-1315

LIQUID CRYSTAL BASED OPTICAL PHASED ARRAY FOR STEERING LASERS

Lei Shi and Philip Bos

Kent State University

**OCTOBER 2009
Final Report**

Approved for public release; distribution unlimited.

See additional restrictions described on inside pages

STINFO COPY

**AIR FORCE RESEARCH LABORATORY
SENSORS DIRECTORATE
WRIGHT-PATTERSON AIR FORCE BASE, OH 45433-7320
AIR FORCE MATERIEL COMMAND
UNITED STATES AIR FORCE**

NOTICE AND SIGNATURE PAGE

Using Government drawings, specifications, or other data included in this document for any purpose other than Government procurement does not in any way obligate the U.S. Government. The fact that the Government formulated or supplied the drawings, specifications, or other data does not license the holder or any other person or corporation; or convey any rights or permission to manufacture, use, or sell any patented invention that may relate to them.

This report was cleared for public release by the Wright-Patterson Public Affairs Office and is available to the general public, including foreign nationals. Copies may be obtained from the Defense Technical Information Center (DTIC) (<http://www.dtic.mil>).

AFRL-RZ-WP-TR-2009-1315 HAS BEEN REVIEWED AND IS APPROVED FOR PUBLICATION IN ACCORDANCE WITH THE ASSIGNED DISTRIBUTION STATEMENT.

*//signature//

TIMOTHY FINEGAN, Project Engineer
EO Combat ID Branch (RYJM)
EO Sensor Technology Division (RYJ)

//signature//

ROBERT J. FELDMANN, Chief
EO Combat ID Branch (RYJM)
EO Sensor Technology Division (RYJ)

//signature//

COL. BRIAN C. FORD, Division Chief
EO Sensor Technology Division (RYJ)
Sensors Directorate (RY)

This report is published in the interest of scientific and technical information exchange, and its publication does not constitute the Government's approval or disapproval of its ideas or findings.

*Disseminated copies will show “//signature//” stamped or typed above the signature blocks.

REPORT DOCUMENTATION PAGE				Form Approved OMB No. 0704-0188	
<p>The public reporting burden for this collection of information is estimated to average 1 hour per response, including the time for reviewing instructions, searching existing data sources, gathering and maintaining the data needed, and completing and reviewing the collection of information. Send comments regarding this burden estimate or any other aspect of this collection of information, including suggestions for reducing this burden, to Department of Defense, Washington Headquarters Services, Directorate for Information Operations and Reports (0704-0188), 1215 Jefferson Davis Highway, Suite 1204, Arlington, VA 22202-4302. Respondents should be aware that notwithstanding any other provision of law, no person shall be subject to any penalty for failing to comply with a collection of information if it does not display a currently valid OMB control number. PLEASE DO NOT RETURN YOUR FORM TO THE ABOVE ADDRESS.</p>					
1. REPORT DATE (DD-MM-YY) October 2009		2. REPORT TYPE Final		3. DATES COVERED (From - To) 01 April 2000 – 30 June 2009	
4. TITLE AND SUBTITLE LIQUID CRYSTAL BASED OPTICAL PHASED ARRAY FOR STEERING LASERS				5a. CONTRACT NUMBER	
				5b. GRANT NUMBER F33615-00-1-1681	
				5c. PROGRAM ELEMENT NUMBER 63739E	
6. AUTHOR(S) Lei Shi and Philip Bos				5d. PROJECT NUMBER ARPS	
				5e. TASK NUMBER NJ	
				5f. WORK UNIT NUMBER ARPSNJ05	
7. PERFORMING ORGANIZATION NAME(S) AND ADDRESS(ES) Kent State University Horning Rd Kent OH 44242-0001				8. PERFORMING ORGANIZATION REPORT NUMBER	
9. SPONSORING/MONITORING AGENCY NAME(S) AND ADDRESS(ES) Air Force Research Laboratory Sensors Directorate Wright-Patterson Air Force Base, OH 45433-7320 Air Force Materiel Command United States Air Force				10. SPONSORING/MONITORING AGENCY ACRONYM(S) AFRL/RJYM	
				11. SPONSORING/MONITORING AGENCY REPORT NUMBER(S) AFRL-RY-WP-TR-2009-1315	
12. DISTRIBUTION/AVAILABILITY STATEMENT Approved for public release; distribution unlimited.					
13. SUPPLEMENTARY NOTES PAO case number 88 ABW-09-4722; cleared 06 November 2009. Report contains color.					
14. ABSTRACT Beam steering technologies are attracting more and more research interests and attention because of the benefits of fast tuning, light weight, and synergy with adaptive optics. The liquid crystal OPA technology has been considered for small angle beam steering because of the small pitch, low driving voltages, large birefringence, flexibility, and electrical control. However, the large area resets of the phase profile caused by the fringe fields degrade the achievable device efficiency. Decentered micro-Lens Arrays (DLAs) are excellent as a candidate for moderate angle beam steering, but have mechanical deficiencies. When the micro-lens arrays are transformed and encoded into liquid crystal devices, we can replace the mechanical motion of lenslet with electrical control of the voltage profile precisely. In this work, we develop a liquid crystal tunable polarization grating device characterized with continuous angular tuning capability and high efficiency.					
15. SUBJECT TERMS Decentered Lens Array, DLA, Optical Phased Array, OPA, beam steering, laser steering					
16. SECURITY CLASSIFICATION OF:			17. LIMITATION OF ABSTRACT: SAR	18. NUMBER OF PAGES 196	19a. NAME OF RESPONSIBLE PERSON (Monitor) Timothy Finegan 19b. TELEPHONE NUMBER (Include Area Code) (937) 255-9614, ext. 215
a. REPORT Unclassified	b. ABSTRACT Unclassified	c. THIS PAGE Unclassified			

Table of Contents

Chapter 1: Introduction	1
Chapter 2: Liquid Crystal Decentered Micro-Lens Array	17
Chapter 3: Tunable Liquid Crystal Polarization Gratings.....	68
Chapter 4: Dynamics Modeling of Dual Frequency LCPGs	110
Appendix	146
References	186

Chapter 1

Introduction

1.1 Introduction to beam steering technology

Laser beams with high accuracy, high efficiency, agile pointing, fast speed, and controllable direction to a desired target is an important topic in such fields as free space communications, projection displays, fiber-optical switches or connectors, optical data storage, and other general industrial applications.¹⁻⁶ For example as shown in Fig. [1.1](#), beam steering is one of the key techniques to direct the laser beam (data carrier) from one node in the communication links to another remote node, or delivery the light from the transmitter to the receiver precisely and efficiently in the free space communication. Beam steering device also plays an important role in military applications such as laser guided weapons, laser radar, range determination, and directed-energy weapons, etc.⁷

In terms of beam steering, the direction of the main lobe of a radiation pattern is changed by switching antenna elements or by varying the refractive index of the medium through which the beam is transmitted or by the use of mirrors or lenses.⁸

The most traditional and common method of implementing beam steering is the using of macroscopic mechanically controlled pivoting planar mirrors that have already been a mature technology for many years. The steering speed of the approach is severely limited by the mechanical movements of driven mirrors. The resulting devices are also excessively expensive, heavy, bulky and high power consumption.

Other beam steering methods such as acousto-optic modulator, has such problems as a very limited angular range, slow switching speed. It is very critical for such applications as aerospace systems to both keep costs down and have wide angular range and high steering efficiency. To resolve these limitations, several beam steering technologies have been proposed and developed, such as DMD/DLP by Texas Instruments technology,⁹⁻¹¹ grating light valve,¹² inorganic digital light deflector.¹³⁻¹⁶

The micro beam steering technologies are attracting more and more researches' interests and attentions because of the nature of fast tuning, agile, light weight, changes adaptive, etc. There are currently several implementations of beam steering, such as deformable micro-electrical mirrors (MEMS),¹⁷⁻²⁰ liquid crystal optical phased array (OPA),²¹⁻²³ and lenslet arrays.²⁴ The MEMS technology is fast and reflective. However, it has issues with fill factors and pitch, and only suitable for fine angle steering that is less than 1 degree. The liquid crystal OPA technology has been considered for small angle beam steering because of the small pitch, low driving voltages, large birefringence, flexibility, and electrical control. Nevertheless, the large area resets of the phase profile caused by the fringe fields degrade the achievable device efficiency.²⁵ Lenslet arrays (Decentered micro-Lens Arrays, DLAs) are excellent candidate for moderate angle beam steering, while it also has the limitations with mechanical motion that downgrade the performance of steering speed. When the micro-lens arrays are transformed and encoded into liquid crystal devices, we can replace the mechanical motion of lenslet with electrical control of the voltage profile precisely. In the recent work, we develop a liquid crystal tunable polarization grating

device characterized with continuous angular tuning capability and high efficiency.

1.2 Liquid crystal beam steering devices

Liquid crystal (LC) technology has become a promising and excellent candidate for non-mechanical optical beam steering components because of low driving voltage, large birefringence, and low cost fabrication techniques.²¹

In general, the concept of the common LC beam steering devices can be regarded as a blazed phase gratings (in Fig. 1.2). The LC device with controlled applied voltage profile or cell thickness profile led to the linear phase profile of the transmitted or reflected light exiting from the device. This repeated periodically phase across the entire cell forms a saw-tooth periodic phase characteristic of a blazed grating.

Liquid crystal based beam steering devices usually follow the basic idea of generating a linear change of optical path difference (OPD) across the aperture, which tilts the incident phase front and thereby steers the optical beam.²⁶ The steering angle is determined by the magnitude of phase gradient caused by the spatially varying retardation $\Delta n \cdot d$ (Δn is the effective birefringence, and d is the LC cell thickness). Either the variation of Δn or linear changing of gap d will result in the spatially varying optical phase retardation. This phase profile is imposed on the incident optical beam will steer the light to the designed direction.

Three major approaches are typically considered to implement the liquid crystal beam steering capability. They are liquid crystal digital beam deflector, liquid crystal optical phase arrays, and liquid crystal decentered micro-lens arrays. Furthermore, we

have developed a tunable liquid crystal polarization gratings device with angular tunability and high diffraction efficiency starting from the concept of Pancharatnam QHQ plate.²⁷

1.3 Liquid crystal prisms

One approach, first pursued by several research groups like W. Thust, Chuck Titus, et al., is prismatic liquid crystal digital beam deflector as shown in Fig. [1.3](#) which consists of cascaded binary light switches.²⁸⁻³¹ In each switch, it is consisted with a polarization rotation switch and a passive birefringent deflecting element. The incident light with linear polarization with e-mode or o-mode is first guided into the polarization rotation switch. The o-mode light unalter the polarization state after propagating through the switch, while the e-mode will be rotated the plane of polarization by 90 degrees. The resulting light is then transmitted into the passive birefringent deflecting prism. The prism consists of a birefringent medium (e.g. liquid crystal) and a means of supporting glass substrates. The optic axis of the birefringent medium is oriented parallel to the vertex of the prism. When light of polarization parallel to the optic axis is received by the prism, its path is deflected. The angular separation between these two deflections is the characteristic angular deflection of that prism. Stacking N such binary switches together can create a device that is capable of deflecting light of 2^N angles. However, the efficiency of this kind of device is limited by the losses caused by the prism array. And no efficient treatment has been found to resolve this problem till now.

1.4 Liquid crystal optical phased arrays

In 1970s, a lot of LC beam steering concepts were developed based on the liquid crystal materials sandwiched between two substrates, having a common electrode on one side, and multi parallel stripe electrodes on the other side. Individual voltages can be applied on the stripes electrodes and common electrodes. Then the spatial variation of the refractive index can be formed. In this approach, Δn is varied to achieve a gradient, however to achieve a large gradient over a large aperture with a continuous phase profile requires a large value of d . The large value of d leads to slow response, absorption and scattering of light by the device. In 1990s, OPA technology was first introduced into beam steering by Paul F. McManamon et al.²⁵ As shown in Fig. 1.4, the OPA approach fixes the problem of large d , found in the simple approach by introducing “resets” into the phase profile whose OPD step is an integer number of wavelengths of the light being considered. These resets, if mathematically ideal, would not be a large problem for a single frequency wavefront, however in real devices it is well known that they degrade the achievable device efficiency. The first OPA devices were described by McManamon et al. with an efficiency of 85% for steering 1 μ m radiation to 1.5°.²⁵ Higher efficiencies have been reported by Raytheon for 10.6 μ m radiation. Raytheon Company firstly fabricated the OPA device in 1988. However, the resets lead to severe wavelength dependence and difficulty to obtain high efficiency (> 95%).²³

1.5 Liquid crystal decentered micro-lens arrays

Another type of liquid crystal beam steering device is called liquid crystal decentered micro-lens array proposed by E. Watson.²⁴

The basic concepts of beam steering using all positive or mixed three-layer decentered micro-lens arrays are shown in Fig. [1.5\(a, b\)](#). By shifting the position of the second and third layers, the input beam will be redirected to the steered angle. Some preliminary researches at the AFRL (air force research laboratory) have already described this type of system. With the micro-lens arrays encoded into liquid crystal devices, we can substitute the mechanical motion of lenslet with electrical control of the voltage profile. That could be preferable to the LC-OPA device since no resets are existed in the LC lenslet cascades. With appropriate phase compensations on each layer of the cascades, it is possible to obtain very high diffraction efficiency above 95%.

1.6 Tunable liquid crystal polarization gratings

Another approach to obtaining high efficiency beam steering is to apply the concept of Pancharatnam QHQ phase plate in Fig. [1.6](#).²⁷

Several research groups have reported work based on this idea. For example, Honma et al. have shown a lens fabricated through a micro-rubbing technique.³² Crawford and co-workers have demonstrated a LC diffraction grating through a polarization holography exposure on a linear photo-polymerizable polymer alignment layer.³³ Escuti et al. report their LC polarization grating to modulate unpolarized or

polarized light with a grating period as small as $6.3\mu\text{m}$.³⁴ These results have demonstrated the validity of this basic idea of what is called a polarization grating.

In this type of device, circular polarized light is normally incident on a half wave optical retarder with its optic axis spiraling in the plane of the retarder as shown in Fig. [1.7](#). The half-wave retarder is here considered to be a liquid crystal whose director axis corresponds to the slow retarder axis that has an in-plane spiral configuration where the azimuthal angle β linearly rotate from 0 to π , 2π , 3π , etc. As a result of Jones calculus, when the optical path delay (OPD) across the LC cell normal (along z axis) is half wave, the spatial phase profile (along x axis) of the transmitted circularly polarized light will have a common factor $\exp(i \cdot 2\beta(x))$, which means the output phase will linearly transform from 0 to 2π , 4π , and 6π , etc. If the gradient of the azimuthal angle of liquid crystal director is a constant with the rotation angle increasing along a particular direction (x or $-x$ axis in Fig. [1.7](#)), we will obtain a device with increasing phase without any “reset” or discontinuity.

In consideration of a tunable device, we developed a vertically surface aligned, continuous optical phase array (V-COPA) that uses a negative dielectric anisotropy LC material.³⁵ The period of the spiral grating was shown to be varied by adjusting an applied voltage profile, which allows for continuous angular control of the steering angle. In addition, only thickness with half-wave retardation is required for the LC polarization gratings, Throughput of the transmittance light without considerable absorption, scattering etc can be reach to 100% steering efficiency.

1.7 Overview of the report

The report is organized as follows. In the first chapter, we will review the background and previous work of liquid crystal beam steering technology. In chapter two, we will investigate the causes of low efficiency for optical beam steering devices based on liquid crystal Decentered micro-Lens Arrays (DLAs). We show that the efficiency is effected by: the relative phase of light exiting the individual lenses; the imperfect focusing of small lenses due to diffraction; the aberrations related to off-axis light going through a lens; and the diffraction spreading of light beams going through the DLA structure. High steering efficiency of over 94.4% is demonstrated by modeling the transmitted light through the DLA with scalar diffraction theory. We also propose modified phase profiles for the lenses that are a function of angle that substantially improve the performance of these types of devices over the unmodified profiles.

In the following chapter three, we will focused on basic design and concepts of tunable liquid crystal polarization gratings with a nematic liquid crystal (LC) optical phase plate, with a large continuous in-plane gradient that is variable, and its application to a beam steering device with high efficiency. The device is a vertically aligned, continuous phase, optical phased array (V-COPA), that uses a negative dielectric anisotropy liquid crystal material. High steering efficiency of over 95% is demonstrated by modeling of the liquid crystal director field, and its effect on transmitted light. The period of the V-COPA grating can be varied by adjusting an applied voltage profile, which allows for continuous angular control of the diffraction

angle. This continuous steering combined with such high efficiency is unprecedented.

To improve the important issue of tuning speed, in chapter four, we consider the dynamics of the LC polarization gratings. In this chapter we study the dynamics of discrete changes in the phase profile, and also continuous changes in the phase profile through acquired data and numerical modeling. We show that a design based on liquid crystals whose dielectric anisotropy can change sign (as a function of frequency) allows continuous tuning with reasonable response times.

In addition, the liquid crystal based electronically controlled lens will be briefly described in Chapter five. With this technique, we are able to replace the conventional eye glass with non-mechanical electrically controlled LC lens, also with the capability of different focal length.

Finally, we will present our conclusions and outline the potential future research subjects of the tunable liquid crystal polarization gratings for LC beam steering device.

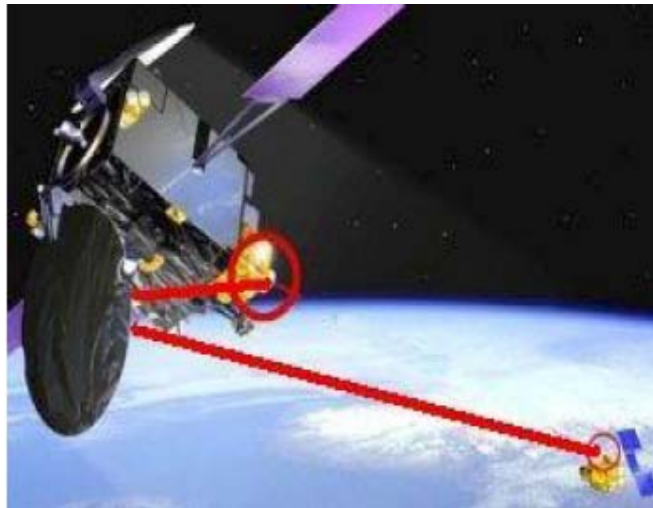


Fig. 1.1 Beam steering component used in free space communication

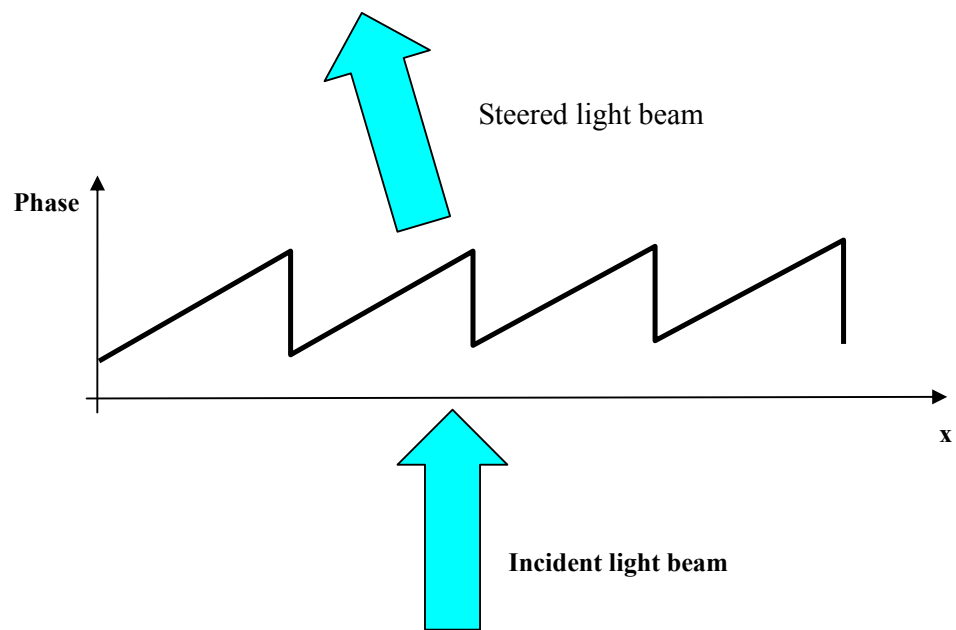


Fig. 1.2 A blazed grating used to deflect the beam

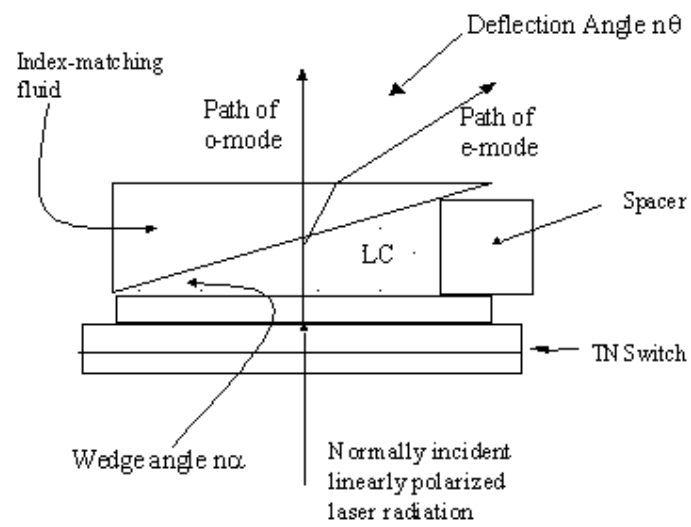


Fig. 1.3 Liquid crystal digital beam deflector with LC prisms

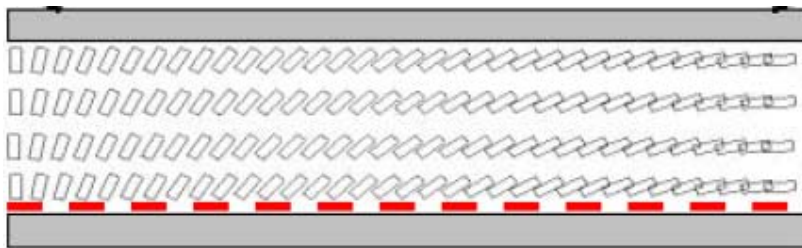


Fig. 1.4 Director configuration of one period of liquid crystal optical phased array device

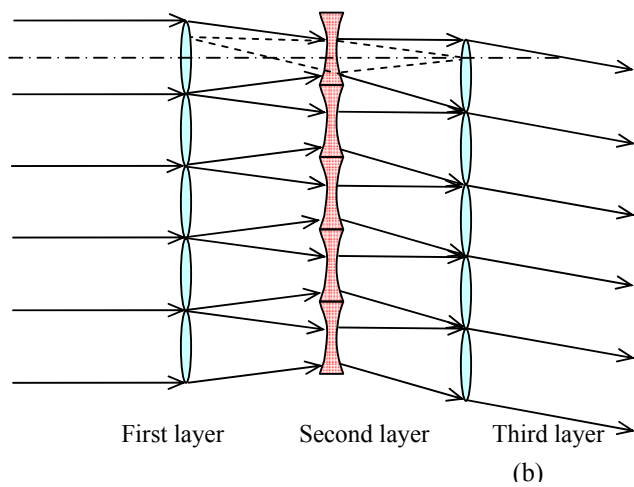
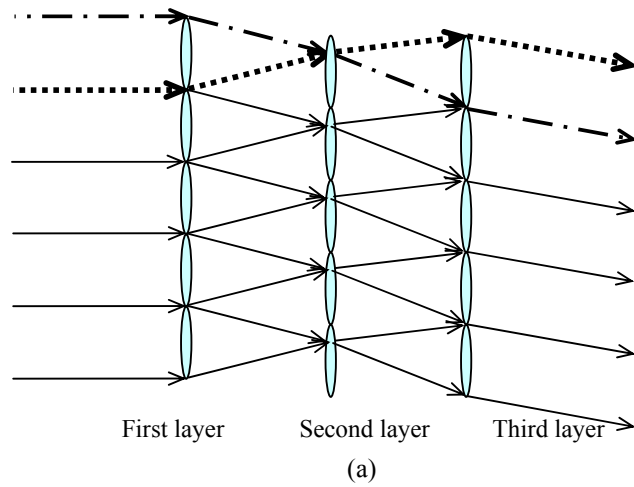


Fig. 1.5 Liquid crystal decentered micro-lens array

(a) all positive three-layer LC decentered micro-lens array

(b) mixed three-layer LC decentered micro-lens array

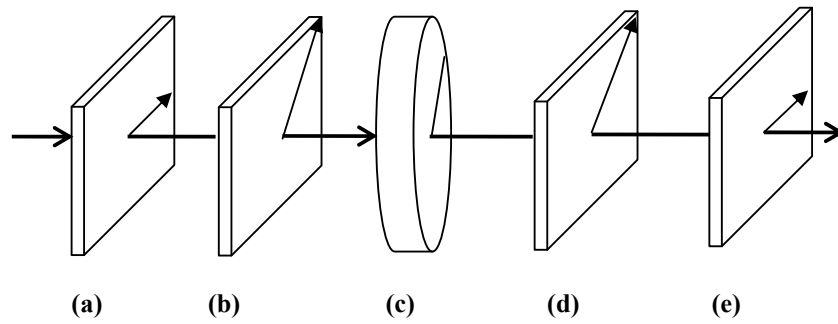


Fig. 1.6 A basic setup of Pancharatnam QHQ stack

(a) & (e): Polarizer; (b) & (d): Quarter-wave Plate; (c): Half-wave plate

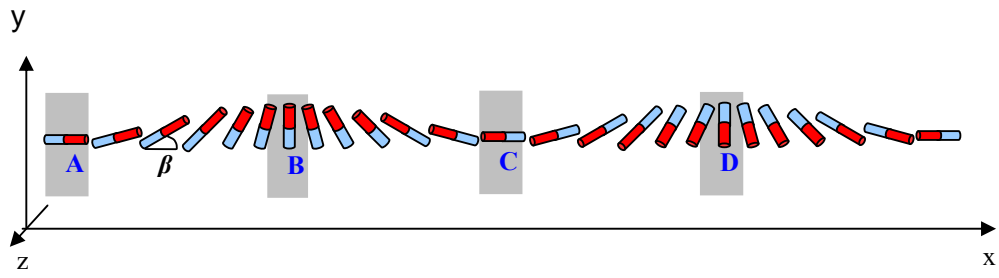


Fig. 1.7 In-plane spiral director configuration (x-y plane) of the polarization grating (named as V-COPA in our design)

Chapter 2

Liquid crystal decentered micro-lens array

2.1 Introduction to liquid crystal decentered micro-lens array

As we have introduced in Chapter 1, the liquid crystal based lenslet (liquid crystal decentered micro-lens array, LC-DLAs) offers an option to realize high efficiency non-mechanical beam steering. The researchers from Wright Patterson Air Force Research Lab, such as Dr. Edward A. Watson, proposed some different configurations of decentered micro-lens array system, for instance, all positive decentered lens array where all the lens are designed with equal positive focal length, and mixed decentered lens array system where a center lens with negative focal length is sandwiched between two layers of positive lens cascades.²⁴ They concluded that the wavefront exiting from a micro-lens array can be treated as a blazed grating, with the angle dependent on the amount of the decenter. Moreover, the periodic nature of the wavefront limits the final diffraction efficiency to the desired direction.

The advanced liquid crystal technology also provided the opportunity to replace the mechanic glass micro-lens with non-mechanical LC materials. When encoding the micro-lens array system into the LC cell, in principal the encoded process is similar to the traditional liquid crystal optical phase array (LC-OPA) system which has been studied for more than ten years. In the typical LC-OPA system, the issue of resetting problem (usually referred as fringe field effect) seriously downgraded the steering efficiency as shown in Fig [2.1](#). However no such effect will exist in the liquid crystal decentered micro-lens array system that the LC material is used to reproduce the

phase profile of lens arrays that have no abruptly phase resets internally. Another advantage of DLAs with liquid crystal material is that the LC micro-lens cascade can be electronically controlled solely and can be packed more densely in practice. It can offer the capability of phase correction by tuning the liquid crystal phase profile to the objective compensated lens profile which will minimize the loss from the edge diffraction and obtain high diffraction efficiency.

Dr. Jianru Shi from Liquid crystal Institute of Kent State University has developed the theoretical modeling program of DLAs in analyzing the limits and considerations of Liquid crystal decentered micro-lens array.³⁶ In his work, Dr. Shi implemented the detailed calculation and optimized simulation results of the expected efficiency of this LC-DLAs cascade system by scalar integration approach and the FDTD (Finite Difference Time Domain) modeling method. Some unexpected issues in the all positive lens system are raised in his work, such as the “flipping” effect and ill-focusing problem of positive lens with incident light of Gaussian beam. To avoid these issues, as an alternative design, we will introduce the mixed LC-DLAs cascade system where the center liquid crystal lens has a negative focal length. Both of these LC-DLAs systems will suffer from the edge diffraction loss and low efficiency caused by several factors without any phase correction and compensation. In this chapter, we will investigate several important factors related to the final loss of the diffraction efficiency and thereafter show the optimized phase compensation procedures which can lead to a very high steering efficiency of over 94%.

The general algorithms of beam steering with all positive or mixed three-layer decentered micro-lens array system have already been shown in Fig. [1.5\(a, b\)](#) of Chapter 1. In this chapter, we will denote the lens with positive focal length as positive lens, and the lens with negative focal length as negative lens. To illustrate the steering algorithm, the configurations of three-layer

macroscopic lenses are shown in Fig. 2.2(a, b). Note that the subscript numbers (1, 2, and 3) are defined as the layer number. In the all positive micro-lens system (Fig. 2.2(a)), the focal lengths of all the lenses are identical, $f_1 = f_2 = f_3$. The inter-layer spacing is equal to the focal length. The beam after exiting the third lens is steered by shifting the second and the third lens towards the same direction. The decentered amount Δ_2 of the second lens is also same as the one of the third lens. In the mixed lens system (Fig. 2.2(b)), the second negative lens and the third positive lens are translated with respect to the first positive lens in the opposite direction, with the amount Δ_2 and Δ_3 respectively, where Δ_3 is two times of Δ_2 . The focal length of negative lens f_2 is one fourth of the positive lens f_1 , where f_1 is equal to f_3 . The inter-layer spacing is half of the focal length f_1 .

To characterize the optical performance of the LC cascades, firstly we develop the simulation programs and tools to simulate the light propagation through the three-layer LC lens cascade. By the means of our LC3D routine, we are able to simulate and optimize the phase profile of the liquid crystal micro-lens required in the system.

2.2 Numerical modeling methods

2.2.1 Kirchhoff's scalar integral method

To describe the propagation of the incident beam through the LC-DLAs cascade system and calculate the final diffraction efficiency in the far field, we develop a scalar integral method according to the Huygens-Fresnel diffraction theory.³⁷ In Fig. 2.3, three micro-lens layers are assumed to be thin layers with the optical path delay (OPD) profile of $OPD_1(x_1)$, $OPD_2(x_2)$, and $OPD_3(x_3)$. Denote the radius of lens as r , and the off axis distance as x , the OPD function of an ideal positive ideal lens is given by:

$$OPD_1(x_1) = \sqrt{r^2 + f_1^2} - \sqrt{x_1^2 + f_1^2} \quad (2.1)$$

Similarly, the OPD function of an ideal negative lens is defined as follows:

$$OPD_2(x_2) = \sqrt{x_2^2 + f_2^2} - f_2 \quad (2.2)$$

In addition, three different phase compensations (phase-up correction, aberration correction and mirror symmetry correction) will be applied to the phase profile of LC micro-lens to obtain high efficiency respectively (details in section 2.4). Therefore the final objective OPD profile for each layer can be written as:

$$\begin{aligned} OPD_1'(x_1) &= OPD_1(x_1) \\ OPD'(x_2) &= OPD_2(x_2) + OPD_{\Delta 2}(x_2) + OPD_{\Delta mirror 2}(x_1) \\ OPD_3'(x_3) &= OPD_3(x_3) + OPD_{\Delta 3}(x_3) + OPD_{\Delta phase_up 3}(x_3) \end{aligned} \quad (2.3)$$

A Gaussian beam E_0 is normal incident through the first positive lens layer:

$$E_1(x_1) = E_0(x_1) \cdot e^{ik \cdot (OPD_1'(x_1))} \quad (2.4)$$

By the *Kirchhoff's scalar integral*, we may calculate the field from the first layer to the second layer by Eq. (2.5):

$$E_{2a}(x_2) = \int E_1(x_1) \left(\frac{1 + \cos \theta_1(x_1)}{2} \right) \cdot \frac{e^{ik \cdot r_1}}{\sqrt{r_1}} dx_1 \quad (2.5)$$

The wave traversed through the second negative lens layer is:

$$E_{2b}(x_2) = E_{2a}(x_2) \cdot e^{ik \cdot (OPD_2'(x_2))} \quad (2.6)$$

From the second layer to the third layer, the transmitted wave can be given by:

$$E_{3a}(x_3) = \int E_{2b}(x_2) \left(\frac{1 + \cos \theta_2(x_2)}{2} \right) \cdot \frac{e^{ik \cdot r_2}}{\sqrt{r_2}} dx_2 \quad (2.7)$$

Note that the inclination factor $\frac{1 + \cos \theta}{2}$ is only good for small angles. It will cause inaccuracy at large angles.

At the third positive lens layer:

$$E_{3b}(x_3) = E_{3a}(x_3) \cdot e^{ik \cdot (OPD_3'(x_3))} \quad (2.8)$$

The wave E_{3b} is equivalent to the near field E_{near} , which can be transformed to the far field E_{far} . The diffraction pattern of exiting beam in the far field can be obtained by Kirchhoff's scalar integral too. To be consistent with the general mechanism of light detection, we can define the diffraction efficiency as the ratio of the peak intensity of the main lobe over the peak intensity of the reference beam.

2.2.2 Liquid crystal director modeling method

The DLAs cascade system can be programmed into liquid crystal based devices. Liquid crystal director modeling is employed to find the correct voltage that needs to be applied on each pixel region of the lens to obtain the desired phase profile. Fig. 2.4 shows the structure of a typical LC cell configuration of a positive liquid crystal micro-lens unit. It has a liquid crystal layer sandwiched between two glass plates coated with a common indium tin oxide (ITO) transparent electrode on one substrate, and striped electrodes on the other. By applying different individual voltage on the electrodes, the orientation of LC director over all the pixels in the bulk can be controlled precisely. Variable optical path delay (OPD) along x axis can be obtained to form a phase profile of either the positive or negative micro-lens as described in Eq. (2.1–2.3).

To encode the micro-lens phase profile into the liquid crystal cell, the first step is to characterize the LC cell's OPD curve with respect to the ramped voltage by a simple one dimensional (1D) LC director simulation (along z axis) as shown in Fig. 2.5. Since for each point on the OPD profile of a LC micro-lens can be found a corresponding voltage value on the OPD vs.

Voltage curve, the first entry voltage profile of a positive or negative micro-lens can be thereby derived. In principle, the OPD depth of the target lens profile must less than the maximum OPD of LC cell as shown in Fig. 2.5. In order to avoid the two plateau regions *I* and *III*, where one is applied with 0V or small voltage (approximately keep with the initial director configuration along the surface alignment direction), and another is involved with high voltage (vertical director configuration, not stable and hard to convergent and reach equilibrium state), we usually select the linear region *II* as shown in the Fig. 2.5 to map the objective ideal positive or negative lens phase profile as shown in Fig. 2.6 into the individual voltage on each pixel of LC cell.

By applying the initial voltage on the system, the equilibrium state of the LC director configuration will be simulated by a two dimensional LC model with vector field method. The liquid crystal director orientation is considered to be a function of *x* and *z*. Note that we define *x* axis is along the cell surface and perpendicular to the stripe electrodes, *y* is along the electrodes direction, and *z* is along the cell normal. The generalized force on the director components (**n_x**, **n_y** and **n_z**) is given by:

$$[f_G]_{n_i} = -\frac{\delta f_G}{\delta n_i} = \frac{\partial f_G}{\partial n_i} - \sum_{j=x,y,z} \frac{d}{dj} \left[\frac{\partial f_G}{\partial \left(\frac{dn_i}{dj} \right)} \right] \quad i = x, y, z. \quad (2.9)$$

Where f_G is the Gibbs free energy density, formed from the elastic free energy density and the electric free energy density, and $-\delta f_G / \delta n_i$ is the functional Euler-Lagrange derivative of it.

The general update formula for each grid is the balance between the viscous torque and that from Eq. (2.9):

$$\gamma \frac{dn_i}{dt} = -\frac{\delta f_G}{\delta n_i} + \lambda n_i \quad i = x, y, z. \quad (2.10)$$

Here γ is the viscosity coefficient and λ is a Lagrange multiplier used to maintain the unit length of the director $|\mathbf{n}| = 1$. Since the \mathbf{n} will be renormalized in each iteration, the Lagrange multiplier λ can be dropped.

The derivatives can be replaced by finite difference to discretize the Eq. (2.10) in our 2D modeling:

$$\begin{aligned}\gamma \frac{\Delta n_i}{\Delta t} &= -[f_G]_{n_i} \\ \Delta n_i &= -\frac{\Delta t}{\gamma} [f_G]_{n_i} \\ n_i^{new} &= n_i^{old} - \frac{\Delta t}{\gamma} [f_G]_{n_i} .\end{aligned}\quad (2.11)$$

Here vector method is employed to obtain the liquid crystal director configuration with applied electric field. The derivative of elastic free energy density can be derived by the typical Frank-Oseen equation including splay, twist and bend free energy density as shown in Eq.(2.12):

$$f_{elastic} = \frac{1}{2} K_{11} (\nabla \cdot \vec{n})^2 + \frac{1}{2} K_{22} (\vec{n} \cdot \nabla \times \vec{n} + q_0)^2 + \frac{1}{2} K_{33} (\vec{n} \times \nabla \times \vec{n})^2 \quad (2.12)$$

Where K_{11} , K_{22} , and K_{33} are the elastic constants named as splay, twist and bend constants of deformation of the liquid crystal directors, q_0 is the chiral number to specify the twist of LC material.

The electric free energy with respect to n_x , n_y and n_z can be defined by the Eq.(2.13), that is, the product of the electric field and electric displacement, which is for constant voltage case:

$$\begin{aligned}
f_e &= \frac{1}{2} \vec{E} \cdot \vec{D} = \\
&\frac{1}{2} (\nabla V) \cdot (\epsilon_0 \epsilon_r \nabla V) = \\
&\frac{1}{2} \left(\frac{\partial}{\partial x} V(x, y, z) \right) \left(\epsilon_0 \left(\frac{\partial}{\partial x} V(x, y, z) \right) \cdot \epsilon_{\perp} + \epsilon_0 \left(\frac{\partial}{\partial x} V(x, y, z) \right) D_e \cdot n_x^2(x, y, z) \right. \\
&\quad + \epsilon_0 D_e n_x(x, y, z) \cdot n_y(x, y, z) \cdot \left(\frac{\partial}{\partial y} V(x, y, z) \right) + \\
&\quad \left. \epsilon_0 D_e n_x(x, y, z) \cdot n_z(x, y, z) \cdot \left(\frac{\partial}{\partial z} V(x, y, z) \right) \right) + \\
&\frac{1}{2} \left(\frac{\partial}{\partial y} V(x, y, z) \right) \left(\epsilon_0 D_e n_x(x, y, z) \cdot n_y(x, y, z) \left(\frac{\partial}{\partial x} V(x, y, z) \right) + \epsilon_0 \left(\frac{\partial}{\partial y} V(x, y, z) \right) \epsilon_{\perp} \right. \\
&\quad + \epsilon_0 \left(\frac{\partial}{\partial y} V(x, y, z) \right) D_e n_y^2(x, y, z) + \epsilon_0 D_e n_y(x, y, z) \cdot n_z(x, y, z) \cdot \left(\frac{\partial}{\partial z} V(x, y, z) \right) \left. \right) + \\
&\frac{1}{2} \left(\frac{\partial}{\partial z} V(x, y, z) \right) \left(\epsilon_0 D_e n_x(x, y, z) \cdot n_z(x, y, z) \left(\frac{\partial}{\partial x} V(x, y, z) \right) + \right. \\
&\quad \left. \epsilon_0 D_e n_y(x, y, z) \cdot n_z(x, y, z) \cdot \left(\frac{\partial}{\partial y} V(x, y, z) \right) + \epsilon_0 \left(\frac{\partial}{\partial z} V(x, y, z) \right) \epsilon_{\perp} \right. \\
&\quad \left. + \epsilon_0 \left(\frac{\partial}{\partial z} V(x, y, z) \right) D_e \cdot n_z^2(x, y, z) \right) \tag{2.13}
\end{aligned}$$

Then we can derive the functional derivative of the electric free energy with respect to n_x , n_y and n_z , which are the director components at discrete points on a two dimensional spatial grid. During each update of the director components on each grid point, the time derivatives are only taken in the forward direction and the spatial derivatives are centered around the grid locations by only considering the nearest neighbors. The electric field can be also discretized into grids represented by the $V(x, y, z)$. The grids of electric field will be updated in each loop once the

dielectric tensor is regenerated by the contemporary liquid crystal director configuration. The approaches for updating the LC director are known as “successive displacement” and “simultaneous displacement”. In each loop, the relaxation process will cover all of the grid points, and for each grid, a new value of each director component (n_x , n_y and n_z) will be calculated. In the successive displacement, each component at a particular grid point will be updated immediately, while the simultaneous displacement will calculate the new values of all the grid points and update them at the same time. To study the equilibrium relaxation process, the successive approach is employed since it tends to reach the equilibrium state quickly and efficiently. As for the simultaneous approach, it is typically used in the dynamics study (details in Chapter 4).

To ensure all the grids can be updated by calculating the new voltages and new director configuration from the adjacent grid points, we need consider the appropriate boundary condition for the LC grids system. There are two common boundary condition used in the liquid crystal modeling: periodical boundary condition and mirror symmetry boundary condition. In the current DLAs system, periodical boundary condition is used. Since we cut the first electrode into half and place them in the first and last pixel (along x) of the system to be consistent with the periodical boundary condition, the LC director configurations in the last pixel are identical to these LC directors in the first pixel.

In this DLA model, the grid size used in our calculation was 2230×50 and the grid spacing was $1.0 \times 0.5 \mu\text{m}$ for x and z respectively. In our discretized numerical model, we enforced the unit length of the director by normalization, rather than using the Lagrange multiplier method. The equilibrium state was assumed to be reached when the tolerance (which is the absolute value of the difference between the current iteration’s average $|[f_G]^{new}|$ and previous iteration’s

average $|[f_G]^{old}|$) was less than 10^{-6} N/m².

When the equilibrium state of director configuration is reached, the OPD profile of the simulated LC configuration can be given by:

$$OPD(x) = \int_0^d (n_{eff}(x, z) - n_o) \cdot dz \quad (2.14)$$

where $n_{eff}(x, z) = \frac{n_o n_e}{\sqrt{n_o^2 \cos^2 \theta(x, z) + n_e^2 \sin^2 \theta(x, z)}}$, while θ is angle between the director and z axis in LC cell.

However, the first entry of the voltage profile may not result in the desired OPD profile of the ideal positive lens or negative lens or the profile combined with phase correction. This is because the fringe field effect which is yielding from the small electrode width (much smaller than the cell thickness) and because of the elastic coupling in the x direction. To minimize the errors between the desired OPD profile and the simulated one, the OPD difference can be calculated and thereby transformed into a voltage difference. Adding the voltage modification to the initial voltage profile (note as the optimization loop #1), we can calculate the LC director configuration again (note as the optimization loop #2). We will repeat the optimization loops until the simulated OPD profile is closed enough to the desired one. This optimization procedure can be illustrated by Fig. 2.7.

Typically, five or six optimization loops are good enough to meet the tolerance requirement and obtain the final optimized phase profile of the LC micro-lens, either the positive lens array or the negative one.

2.3 All positive decentered micro-lens array

2.3.1 Description of all positive micro-lens array

To illustrate the all positive decentered micro-lens array system in Fig. [2.2\(a\)](#), we trace the light propagation through the micro-lens cascades from the geometric point of view, in which diffraction effects are ignored. A collimated input beam is split into separate cones at the first layer. The wavefront is supposed to focus at the plane of the second layer and then recover to the parallel transmitted beam with the third lens array, and redirected to some certain angle by the decentered displacement of the second and third layer. In the all positive LC-DLAs, the layer spacing is equal to the focal length of the positive lens. The decentered amounts are also equal for the 2nd and 3rd lens array. Since the individual micro-lens is only in the dimension of hundreds of microns, the output beams are characterized with diffraction properties that the macroscopic lenses did not appear obviously. The final output wavefront is actually similar to the blazed grating.

2.3.2 “Flipping effect”

Obviously, in this all positive system, a “flipping effect” will be occurred as shown in Fig. [2.8](#). The reconstructed deflected beam will have certain loss inevitably because of the inversion of the individual wavefront of each lens.

2.3.3 Robust lens condition for a positive lens

To understand the throughout loss of the all positive DLAs, an analysis of the robust lens condition for a positive lens will be helpful. A lens does not meet this condition when the Gaussian beam divergence related to the lens aperture is significant compared to its focusing power as shown in Fig. [2.9](#). In this case it is not possible for the lens to provide a sharp focus point when illuminated with collimated light.

We describe the robust lens condition Γ as:³⁸

$$\Gamma = \left(\frac{\pi \cdot w^2}{\lambda \cdot R} \right) \gg 1 \quad (2.14)$$

where w is the beam waist of a Gaussian incident light, set it as $D/2$, where D is lens diameter, R is equal to the focal length f here, then we can rewrite Γ as:

$$\Gamma = \left(\frac{\pi \cdot w^2}{\lambda \cdot R} \right) = \left(\frac{\pi \cdot D^2}{4\lambda \cdot f} \right) \approx \frac{D^2}{\lambda \cdot f} \gg 1 \quad (2.15)$$

For a positive lens, the OPD profile can be written as $x^2/2f$ approximately. Note that the variable x is off axis distance, range from $-r$ to r , and r is the radius of the lens. The OPD depth (maximum available OPD of a lens) of a positive lens is about $D^2/8f$. The robust lens condition Γ can be given by:

$$\Gamma = \frac{D^2}{\lambda \cdot f} = \frac{8 \cdot OPD_{\max}}{\lambda} \gg 1 \quad (2.16)$$

From Eq. (2.16), to make a robust positive lens, the OPD depth should be much larger than the designed wavelength. Otherwise, the Gaussian beam waist will locate far away from the spherical center of lens. The micro-lens is not able to focus the incident beam and is actually an ill lens.

For the case of an all positive DLAs this condition is a limiting one, however in the case of a mixed lens system, we will shown in the next section that a modification to the lens phase profile of the center lens can correct for this problem.

2.4 Mixed decentered micro-lens array

2.4.1 Description of mixed micro-lens array

As for the mixed decentered micro-lens array system in Fig. 2.2(b), similarly, from the

geometric point of view, a collimated input beam is also split into separate cones at the first layer same as the all positive system. However, the wavefront is reconstructed at the second layer without focusing to the back focal point. Compared with the all positive system, the negative lens will avoid such issues as ill-focusing of a Gaussian beam and “flipping” effect. The beam is recollimated and deflected to a non-zero field angle exiting from the third layer. A paraxial ray trace shows that the tangent of the field angle φ_3 is equivalent to the amount of decentered Δ_3 divided by half of the focal length f_3 . By shifting the position of the second and third layers, the input beam will be redirected to the steered angle. When the micro-lens arrays are encoded into liquid crystal devices, we can substitute the mechanical motion of lenslet with electrical control of the voltage profile in all the electrode pixels.

2.4.2 Design considerations

The properties of the exiting wavefront of micro-lenses are different with the output from the macroscopic lenses that can be simply analyzed by the paraxial ray tracing. In fact, it is necessary to consider DLAs (all positive DLAs or mixed DLAs) as being diffractive devices.

When we consider DLAs as diffractive devices, the diffraction efficiency (DE) of a decentered lens arrays is affected by:

- Phase up of the outgoing wavefronts from the individual lenses
- The off-axis aberration of the lenses
- Robust lens condition limitation
- Diffractive scattering from the aperture of the first lens layer

The first two can be corrected by modifying the lens profile vs. steering angle. The robust

lens condition limitation can be corrected in the “mixed lens” system by modifying the lens profile of the center negative lens. Therefore, in a mixed DLAs system these three issues can be corrected by the phase compensation of the conventional lens profile. However the last factor cannot be corrected and sets the DE limit of a micro-lens array as determined by the lens diameter.

2.4.3 Three phase compensations of mixed micro-lens arrays

To understand the efficiency losses of the micro-lens cascades, we studied three different aspects of the phase compensations. We studied three sources of the efficiency loss occurred in mixed micro-lens arrays and their correction approaches. The off-axis aberration correction can be applied on either positive or negative micro-lens layers. The phase-up corrections are usually applied on the third positive micro-lens array. The mirror symmetry correction is designed specifically for the mixed micro-lens system to correct for the non-robust nature of the micro-lenses.

a. Off-axis aberration correction

The algorithm of off-axis aberration correction of the DLAs can be understood by first considering an ideal single positive lens, as shown in Fig. [2.10](#). A collimated input plane wave, denoted as ray AB and ray $A'B'$, is oblique incident on the positive lens with a tilted angle φ_3 from right to left. Note that BD is perpendicular to $A'B'$, point B and D are in the same wavefront before the beam passes through the lens. The exiting beam is focused to the back focal plane OO' at point O with ray BO and ray $B'O$, where the distance BO is denoted as R . Draw a circle of radius R centered at O . Note that point C in ray $A'B'$ is also on the circle with radius R . Then point B will have the same wavefront as point C after the beam transmits through the lens. Compare the

two wavefronts, the optical path difference of this positive lens can be written as:

$$OPD_{\Delta+} = -DC = OD - OC = OB' + B'D - OC = OB' + B'D - OB \quad (2.17)$$

Note that $O'B'$ is equal to f_3 , BB' is the distance x from point B to the center of lens B' . OO' is denoted as d .

From Eq. (2.17), the phase difference in Fig. 2.10 can be described by:

$$\begin{aligned} OPD_{\Delta+}(x) &= \sqrt{f_3^2 + d^2} + x \sin \varphi_3 - \sqrt{f_3^2 + (x+d)^2} \\ &= x \sin \varphi_3 - \left(\sqrt{f_3^2 + (x + f_3 \cdot \tan \varphi_3)^2} - \sqrt{f_3^2 + (f_3 \cdot \tan \varphi_3)^2} \right) \end{aligned} \quad (2.18)$$

Fig. 2.11 shows the case of a single negative lens. The collimated beam incidents at the negative lens with a tilted angle φ_2 from left to right, defined as ray AB and ray $A'B'$. Similarly, point B and D are in the same wavefront before pass through the lens, while point B and C have the same phase after pass through the lens. It yields the following optical path difference of the negative lens:

$$OPD_{\Delta-} = DC = A'C - A'D = A'B - A'B' - B'D \quad (2.19)$$

As illustrated in Fig. 2.11, it can be rewritten as:

$$\begin{aligned} OPD_{\Delta-}(x) &= \sqrt{f_2^2 + (x+d)^2} - \sqrt{f_2^2 + d^2} + x \sin \varphi_2 \\ &= \sqrt{f_2^2 + (x + f_2 \cdot \tan \varphi_2)^2} - \sqrt{f_2^2 + (f_2 \cdot \tan \varphi_2)^2} - x \sin \varphi_2 \end{aligned} \quad (2.20)$$

In Fig. 2.2(a, b), consider a non-steered system where the decentered amount Δ_2 and Δ_3 are both equal to 0, and φ_2 and φ_3 are thereafter equal to 0. The phase differences of non-steered system can be given by:

$$\begin{aligned} OPD_{0+}(x) &= f_3 - \sqrt{f_3^2 + x^2} \\ OPD_{0-}(x) &= \sqrt{f_2^2 + x^2} - f_2 \end{aligned} \quad (2.21)$$

(2.22)

The final aberration of the third positive lens for a non-zero steered angle can be described as

Eq. (2.18) minus Eq. (2.21):

$$OPD_{\Delta 3}(x_3) = \sqrt{f_3^2 + (f_3 \tan \varphi_3)^2} - f_3 + x_3 \sin \varphi_3 - \left(\sqrt{f_3^2 + (x_3 + f_3 \tan \varphi_3)^2} - \sqrt{f_3^2 + x_3^2} \right)$$

where the term $\sqrt{f_3^2 + (f_3 \tan \varphi_3)^2} - f_3$ is a constant, and can be neglected. The off-axis

aberration correction for the third positive lens is given by:

$$OPD_{\Delta 3}(x_3) = x_3 \sin \varphi_3 - \left(\sqrt{f_3^2 + (x_3 + f_3 \tan \varphi_3)^2} - \sqrt{f_3^2 + x_3^2} \right)$$

(2.23)

In the same way, the off-axis aberration correction for the second negative lens can be given

by:

$$OPD_{\Delta 2}(x_2) = \sqrt{f_2^2 + (x_2 + f_2 \tan \varphi_2)^2} - \sqrt{f_2^2 + x_2^2} - x_2 \sin \varphi_2 \quad (2.24)$$

b. Phase up correction

The discontinuous phase profile of the wavefront (E_{3b}) exiting from the third positive micro-lens layer is the same as that exiting a blazed grating. The OPD introduced by each lens of third layer is analogous to each prism in a micro-prism array of a blazed grating as shown in Fig. 2.12. The discontinuous phase profile shows some deviations from a straight line that represents the ideal phase without reset for designed wavelength. These discontinuities will cause dispersion and loss of efficiency if they are not a multiple of the transmitted light's wavelength. However an addition term, $OPD_{\Delta \text{Phase_up}3}$ can be added to each micro-lens in the third layer to cause this condition to be met.

c. Mirror symmetry correction

In Fig. 2.2(b), given the decentered amount of the second and third lenses equal to 0, the wavefront is symmetric on both sides of the second negative micro-lens from the geometric point of view. However, due to the diffractive effects of the first positive micro-lens array, this mirror symmetry about the second layer will be destroyed. The idea of this correction is to modify the phase profile of the second LC micro-lens by adjusting the voltage profile, so that the ideal mirror symmetry is restored.

In Fig. 2.13, as for a case of non-steering, the phase entering the second layer is shown as $P_{2a}(x)$. The phase of the second lens is given as $P_2(x)$. The exiting phase, $P_{2b}(x)$, from the second layer can be given by:

$$P_{2b}(x) = P_{2a}(x) + P_2(x) \quad (2.25)$$

As required by the mirror symmetry, the input wavefront is defined as:

$$\begin{aligned} P_{2a}(x) &= -P_{2b}(x) + 2 \cdot h \\ P_{2a}(x) &= -(P_{2a}(x) + P_2(x)) + 2 \cdot h \end{aligned} \quad (2.26)$$

where h is the peak height of P_{2a} . The modified phase $P_2(x)$ for non-steered case can be rewritten as:

$$P_2(x) = -2 \cdot P_{2a}(x) + 2 \cdot h \quad (2.27)$$

Then the mirror symmetry correction term required for the ideal negative lens with phase profile $OPD_2(x)$ of the non-steered case will be given by:

$$OPD_{\Delta mirror 2}(x) = P_2(x) - OPD_2(x) \quad (2.28)$$

Note that $P_2(x)$ is actually determined by the inputting wavefront of the first lenslet, that is always in the fixed location. Even the second micro-lens layer is translated by the decentered amount Δ_2 , the mirror symmetry correction term $OPD_{\Delta mirror 2}$ will keep with the same profile

and location of the initial non-steered one. The new phase profile of the negative LC micro-lens will be the fixed $OPD_{\Delta mirror 2}(x_1)$ superimposed on the shifted ideal negative lens profile $OPD_2(x_2)$.

2.5 Simulation Results of LC-DLAs

2.5.1 Limitations of all positive DLAs

The Fig. [2.14\(a-e\)](#) below show the near field phase profile from a non-steered positive lens array as a function of the OPD of the micro-lens and their diameter.

It can be seen that there is a strong correlation with the smoothness of the near field profile with the OPD of the lenses. This smoothness is reflected in the far field DE as is also shown. The figures also show the “flipping” effect of the input Gaussian beam profile by an all positive DLA (that can be understood by considering the dashed lines that represent light rays in Fig. [1.5\(a\)](#)) (in Chapter 1) further affects the far-field DE.

It is interesting to study the efficiency dependency with respect to the OPD depth of the all positive micro-lens array. In Fig. [2.15](#), it turns out that the all positive micro-lens system with single lens will be very hard to achieve high efficiency unless the OPD depth of the lens is larger than about $5\mu\text{m}$ at the wavelength of $1.5\mu\text{m}$. This result is actually expected from the “robust lens” condition in Eq. [\(2.16\)](#). Moreover, in a five-lens array, the maximum efficiency decreases to 95% because of the “flipping” effect of positive lenses. Considering a liquid crystal cell with the relatively high birefringence of 0.3, to satisfy the “robust lens” condition, the thickness of the cell should be around $15\mu\text{m}$ at least. Such a thick LC cell will make high speed switching difficult, and can lead to extra scattering and absorptive losses.

Looking at the far-field results, both on axis and as a function of the steering angle, we can consider an all positive micro-lens array in Fig. 1.5(a) with lens radius as 552 μm , focal length as 57.498 mm, OPD depth as 2.6496 μm , and totally 5 lenses in each layer, the final diffraction efficiency is only about 89.05% for no steering at the wavelength of 1.5 μm with a Gaussian incident beam, as shown in Fig. 2.16(a). Without any phase compensations, the efficiency for steering light in Fig. 2.16(b) will even lower to 55.4% at the steering angle of 0.50 $^\circ$.

For the small lenses with long focal length, the beam divergence can compete with the focusing power of the lens, and therefore prohibit the positive lens from focusing as it does for larger diameter or shorter focal length lenses (with an OPD > 5) . This major drawback is hard to resolve in the all positive lens system without going to thick liquid crystal cells. However in the mixed micro-lens system, since no focus at the position of the second layer is required as described in the proceedings, the issues with the “robust lens” condition can be solved by modifying the phase profile the middle lens so that the phase fronts on either side of it are mirror symmetric. And also the flipping effect is eliminated.

2.5.2 Out-of-lens leakage of mixed micro-lens array

In the next section, the results of phase compensation to the lens profiles of a mixed lens system will be shown to be capable of solving the issues with off-axis lens aberration, the phase up of the outgoing wavefronts from the individual lens, and the “robust lens” issue by applying the “mirror symmetry” condition to the middle lens. However there is another issue, related to the diffractive loss, that cannot be corrected, given a particular lens diameter, that we will discuss first.

To understand the diffraction loss of the mixed system, a very simple model is designed to illustrate the efficiency loss with respect to the micro-lens diameter size. Consider a square phase profile that traverses through the first positive layer of a mixed system with 5 micro-lenses in each layer. The square phase profile is located in the center of the array, and has a diameter exactly equal to the lens size, as shown in Fig. [2.17\(a\)](#). The beam profile after the first positive layer and right before the second negative layer can be derived from Eq. [\(20\)](#). By comparing the integral of light intensity within the diameter of the lens in the 2nd layer, with the overall intensity, the out-of-lens leakage for each single micro-lens unit can be calculated. As shown in Fig. [2.17\(b\)](#), the out-of-lens leakage for a micro-lens array with 1104 μm diameter is the regions outside of the two markers, which is about 0.358% in the case of non-decentered array. The leakage implies that the maximum efficiency available for the system is about 99.642% even with all potential compensations applied. In Fig. [2.18](#), the out-of-lens leakage will keep increasing to 4.38% when decreasing the lens size to about 86 μm because the diffraction effect will become more and more dominant, especially for smaller diameter of micro-lens. In the case of a decentered array, for example 0.20 decentered ratio in Fig. [2.18](#), this leakage will increase a little, to 0.419% for a 1104 μm diameter lens, and to 4.99% for a 86 μm diameter lens because more light will diffract and leak out of the shifted second lens. The out-of-lens leakage determines the maximum efficiency available for the mixed system. To construct a mixed micro-lens system with requirement of 98% efficiency, the diameter of each micro-lens should be at least larger than 250 μm .

2.5.3 Simulation results of mixed decentered micro-lens array

In the modeling, the liquid crystal used for a positive LC lens is MLC-10000-000, where $n_e =$

1.6528, $n_o = 1.4971$, $\Delta n = 0.1557$ (at $\lambda = 589$ nm, 20°C) and $\varepsilon_{||} = 37.2$, $\varepsilon_{\perp} = 8.0$ (at 1 kHz, 20°C).

The LC cell gap is 25 μm . Since the desired OPD depth of a negative LC lens is four times of the positive one, it means the cell gap of a negative lens will be also approximately four times of the positive lens if the same liquid crystal material is used. However, a thicker cell will lead to more extra light energy loss by scattering, and absorption, etc. Licrilite-18349 with a larger birefringence is used as the negative LC lens in our model, where $n_e = 1.8025$, $n_o = 1.5321$, $\Delta n = 0.2704$ (at $\lambda = 589$ nm, 20°C) and $\varepsilon_{||} = 21.9$, $\varepsilon_{\perp} = 6.1$ (at 1 kHz, 20°C). The cell gap of the negative LC lens is 50 μm . There are 5 LC micro-lens units in each layer.

The electrode width in Fig. 2.4 is 20 μm , which is a little thinner than the thickness of LC cell. The gap between each electrode is 3 μm . A single LC micro-lens radius covers 24 electrodes. The radius of each micro-lens is 552 μm . The focal length f_1 and f_3 of the positive layers are designed to be 57.498 mm, while the focal length f_2 of the negative layer is designed as 14.374 mm.

After six optimization loops described in section 2.2, an equilibrium director configuration of a positive LC lens can be obtained with small errors of OPD profile compared with the ideal one at the wavelength of 1.5 μm as shown in Fig. 2.19(a). The director configuration of LC cell is illustrated in Fig. 2.19(b). To implement the aberration correction for the third positive lens, we can add the OPD compensation to the ideal positive lens profile together. Since the amount of the aberration correction for a positive lens is relatively very small compared with the OPD depth, it can be easily encoded into the OPD optimization procedures.

The situation for modeling the negative LC lens will be more complicated, which is caused by the mirror symmetry correction. As we mentioned above, the amount and location of mirror symmetry will be in the fixed position according to the location of the first positive layer, while

the OPD profile of the second negative lens will be translated by a decenter amount Δ_2 . Hence for each steering angle, the final sum of the ideal OPD profile and the mirror symmetry correction will be different. So the director configuration will be different for each steering angle. In Fig. [2.20\(a\)](#), a negative LC lens OPD profile incorporated with mirror symmetry correction for a non-dcentered array is shown. For a steered angle of 0.64° , the simulated OPD profile is shown in Fig. [2.20\(b\)](#).

The phase-up correction to achieve a 0 or 2π discontinuity in the exiting OPD profile of the third positive lens, is implemented by placing a series of phase retarder plate at each micro-lens.

Without any phase correction described above for the mixed micro-lens array, the diffraction efficiency for no steering is only about 84.2% in Fig. [2.21](#). The lowest one is 44.4% at the steering angle of 0.275° . It also shows the different contribution of the efficiency improvement by the different phase corrections. Obviously, the aberration correction plays the least important role to improve the efficiency and may be neglected for the case of small deflection angles. The phase up correction is especially critical to some steering angles where the phase discontinuity is about π . The most important factor for micro-lens with small diameter is the mirror symmetry correction. It will enhance the overall performance of the final diffraction efficiency for all of the steering angles. With all these three phase corrections integrated in the mixed LC micro-lens array, the average diffraction of all available steering angles is 96.8%, while the minimum one is 94.4% at the steering angle of 1.008° .

2.6 Fabrication and characterization of LC-DLAs

In order to demonstrate the modeling results, we fabricated the individual layer of LC-DLAs

as shown in Fig. 2.22. Four micro-lens cells in each LC layer are designed to make one layer. Each individual lens is controlled by 48 electrodes. The electrodes on the ITO substrate were coated with accurate width by the photo-lithography technique. The general electrode pattern is shown in Fig. 2.23. There are totally 192 inter-digital electrodes etched in the active area of LC cell on one substrate, while another substrate is simply coated with a common electrode. With the fan-out regions of electrodes, the electrodes in microns can be bonded to the external cables. The mixed liquid crystal micro-lens arrays are filled with the LC materials introduced in section 2.5.3. The positive LC-DLAs is filled with MLC-10000-000. To reduce the large thickness of the negative LC micro-lens, we choose the liquid crystal Licrilite-18349 that has relatively large birefringence Δn as 0.2704.

To verify the algorithm of scalar integral method that is used to characterize the light propagation through the system, the beam profile of each layer is first measured by the schematic diagram of set up in Fig. 2.24. The LC micro-lens layer is illuminated by a collimated beam at 632.8nm with normal incident angle. The beam expander is used to collimate the incident beam, and also zoom in the diameter of the beam to cover the whole active area of LC micro-lens, which is about 5×10 mm. Before the collimated light meets the LC micro-lens layer, the polarization state of the beam will be changed into linear polarization along the rubbing direction by the first polarizer. The LC micro-lens layer is driven by 48×4 electrodes connected with cables to the voltage amplifier controlled by computer. Since the driven voltage profiles are identical for all the four LC lens units, only 48 electrodes input that controlled by the Labview program is necessary. When the driven voltage profile is applied, the collimated beam is then focused by the LC micro-lens at the focal point, which is 57.49 mm theoretically. The second polarizer is used to

attenuate the light intensity to avoid the saturation of light that collected by the PULNiX camera system. The camera system is moved back and forward to locate the focal plane of the positive micro-lens layer, where the focused light beam should have the sharpest profile and highest peak. The measured focal distance is about 51.3 mm. The image of beam profile is shown in Fig. [2.25\(a\)](#). To compare with the simulation results with exactly same parameters and set up, the image profile can be converted into intensity profile in Fig. [2.25\(b\)](#). Note that the measured beam profile needs to be calibrated with the peak-to-peak distance and the height of the maximum lobe to compare with the simulation intensity profile at the focal point. With these calibrations, the FWHM of main lobe and the side lobes are very consistent with the predicted results.

As for the negative micro-lens, the beam profile is not as good as the positive LC micro-lens because it is related to the 50 μ m cell thickness in Fig. [2.26\(a-b\)](#). The cell thickness of the second negative micro-lens can seriously result poor performance of the final assembled mixed micro-lens arrays. To revolve this, two 25 μ m negative LC layers that attached together but driven separately might help to reduce the error. In addition, in the final assembled system, the multi-reflection effect between each layer will affect the final light throughput seriously. The coating layers or some index match medium for the whole LC-DLAs system should be considered to reduce the reflection problem of inner layer.

2.7 Summary

We used a two dimensional liquid crystal director modeling method and three-layer scalar integral optical calculation method to study the liquid crystal mixed micro-lens array. The properties of three different phase correction methods were investigated detailed to optimize the

diffraction efficiency. In general, the mirror symmetry correction and the phase-up correction can resolve the low efficiency problem. By mapping all the phase corrections into the phase profile of LC cells, the minimum efficiency of the system can be improved from 84.2% to 94.4% at the steering angle of 1.008° and with the lens radius of $552\text{ }\mu\text{m}$. We also studied several other important factors that lead to the efficiency loss in the micro-lens system, such as robust lens condition for all positive system, and the out-of-lens leakage due to diffraction.

Another aspect of the LC-DLAs work is that it makes clear that a mechanically DLA may have low efficiency because it does not offer the possibility of providing the steering angle dependent corrections considered here. So this work points to the possibility of considering a larger angle beam steering device that uses mechanically decentered short focal length fixed lens, that are dynamically corrected by integrated LC layers. We also fabricate the positive/negative micro-lens layer of LC-DLAs. The measured beam profile at the focal plane of the positive LC micro-lens demonstrated the feasibility of the above modeling results. However, the very thick negative LC micro-lens resulted in some beam profile error. We may divide the single thicker negative LC cell into two separate units with the opposite rubbing direction (in general, the LC director in one cell will tilt along $+x$ axis, while the other one will tilt along $-x$ axis) to minimize the view angle problem. In addition, to assemble the three layers together, we need to take account into the inner reflection loss between different layers. Specific index match coating technique or medium selection may be considered in the future work.

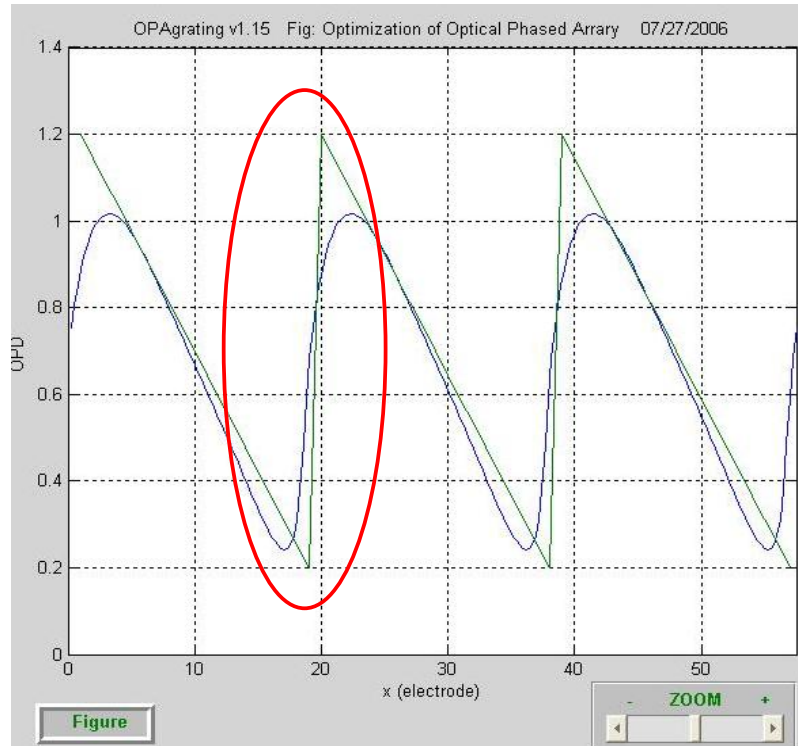


Fig. 2.1 Resetting issues (red circled regions, also refer as fringe field effect) in liquid crystal optical phase array

Green line: ideal grating profile with strictly reset of each period

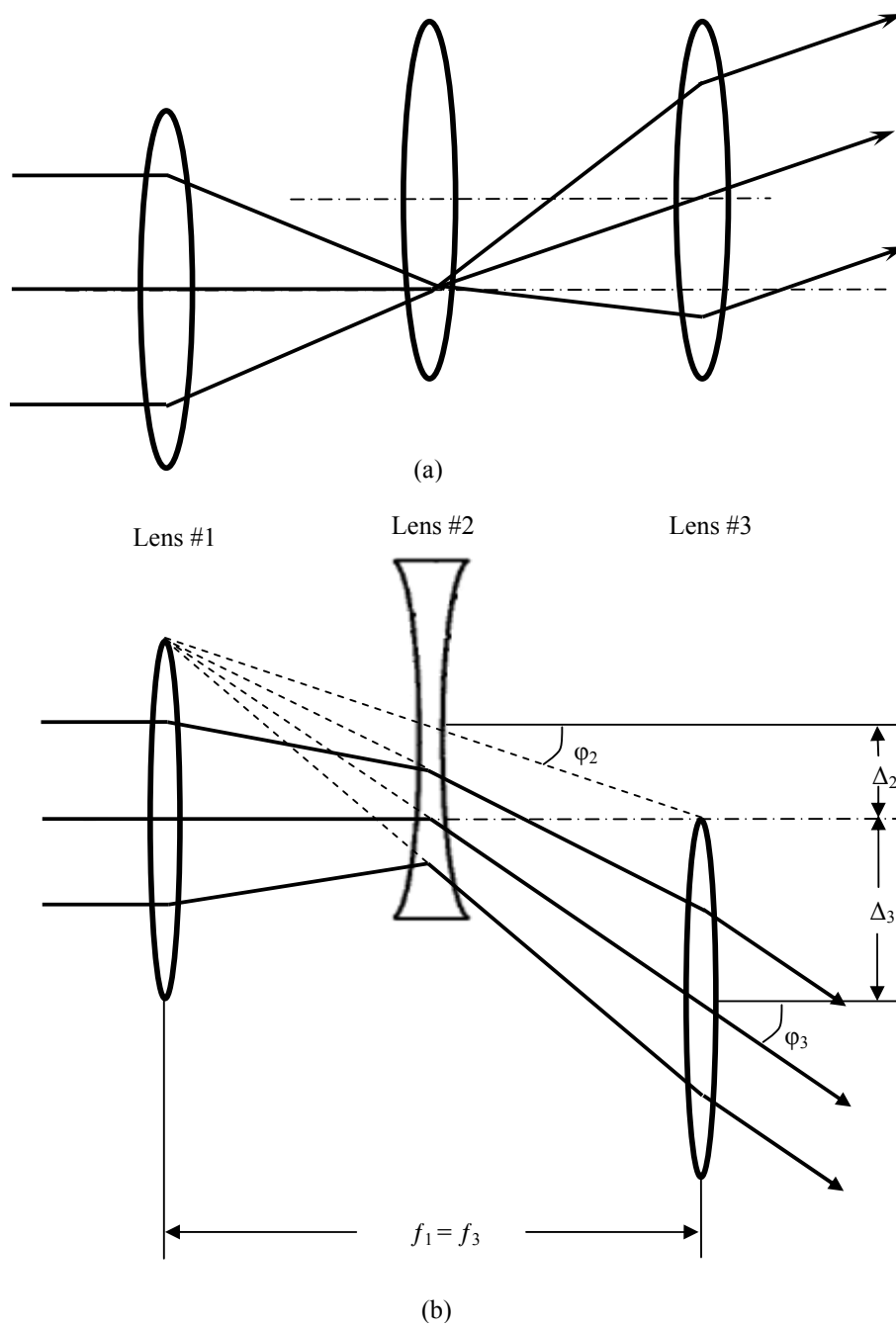


Fig. 2.2 Geometric illustration of beam steering with (a) all positive decentered

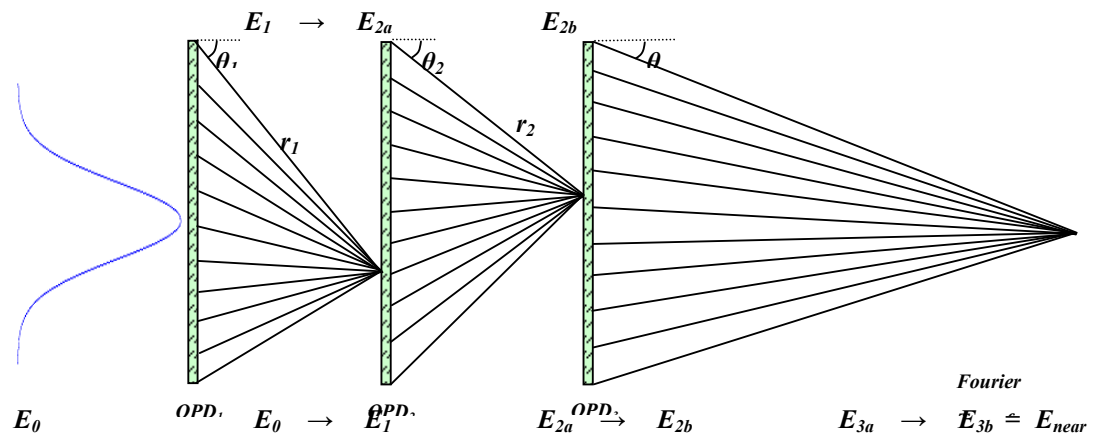


Fig. 2.3 Scalar integral approach of three-layer decentered micro-lens array

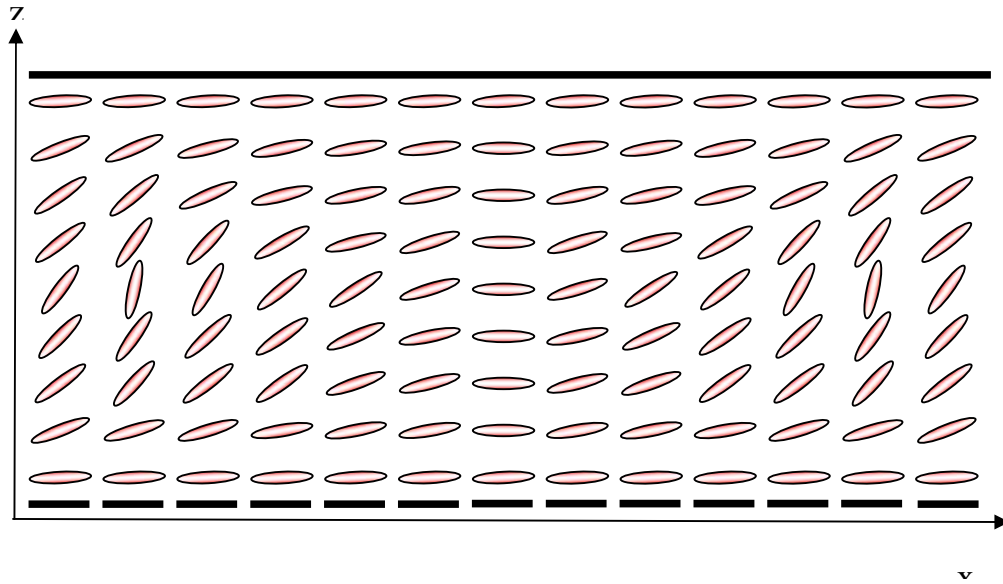


Fig. 2.4 Structure diagram of a single positive liquid crystal micro-lens

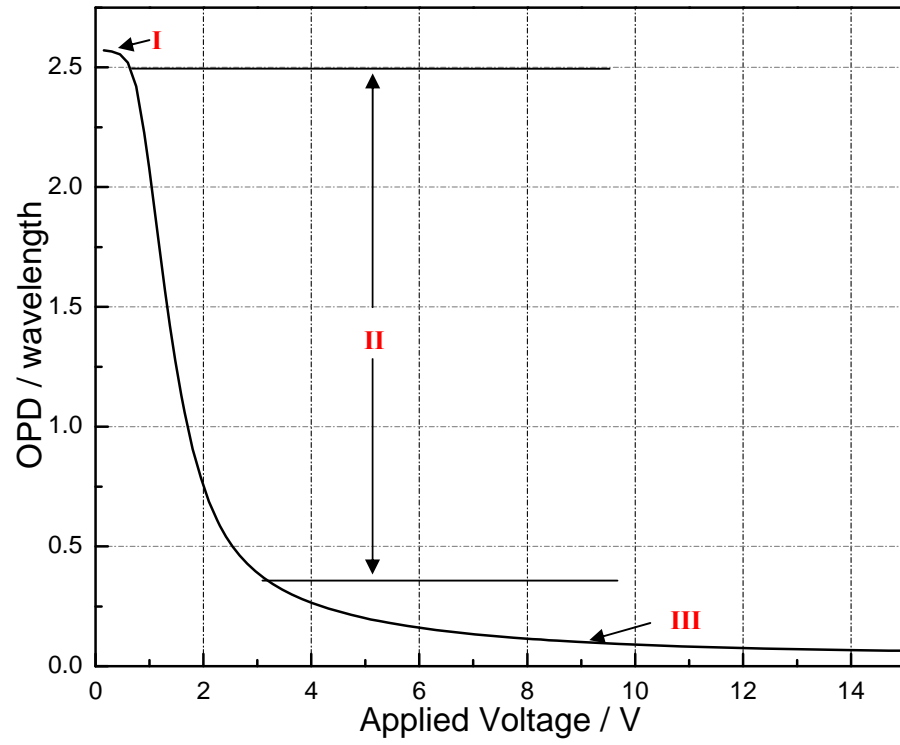


Fig. 2.5 Calculated OPD of a LC cell (designed for positive lens) with respect to the applied voltage (region I and III are two plateaus with low and high applied voltage, region

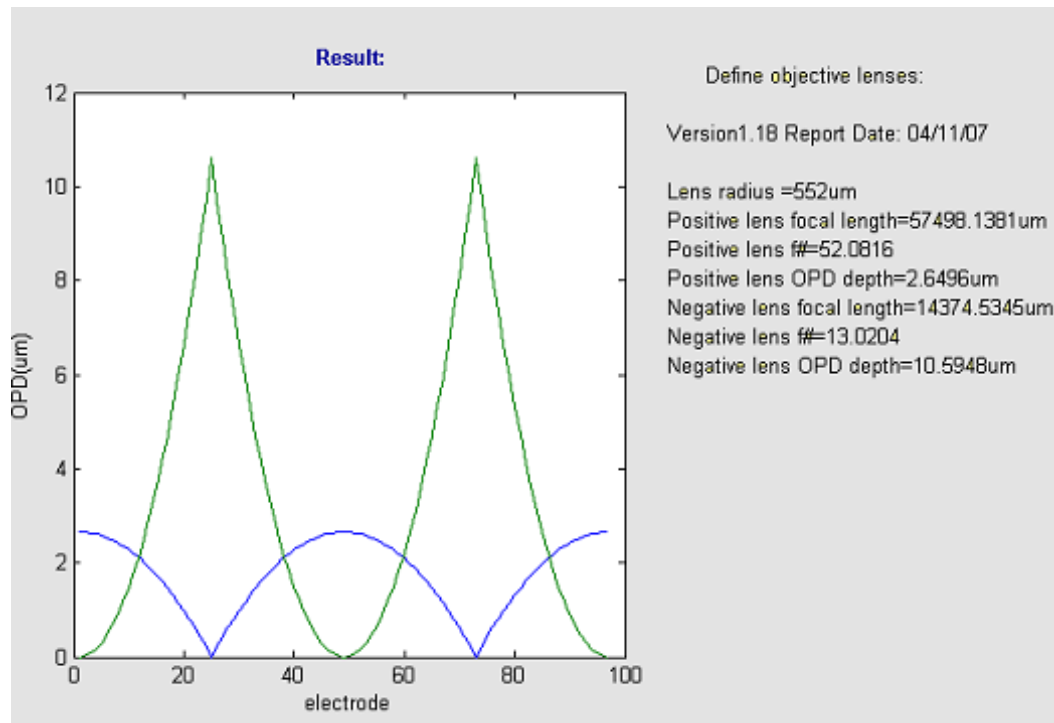


Fig. 2.6 Optical path delay (OPD) profile of ideal objective positive (blue curve) and negative (green curve) lens with 552 μm radius, no reset issue exists in the lens design

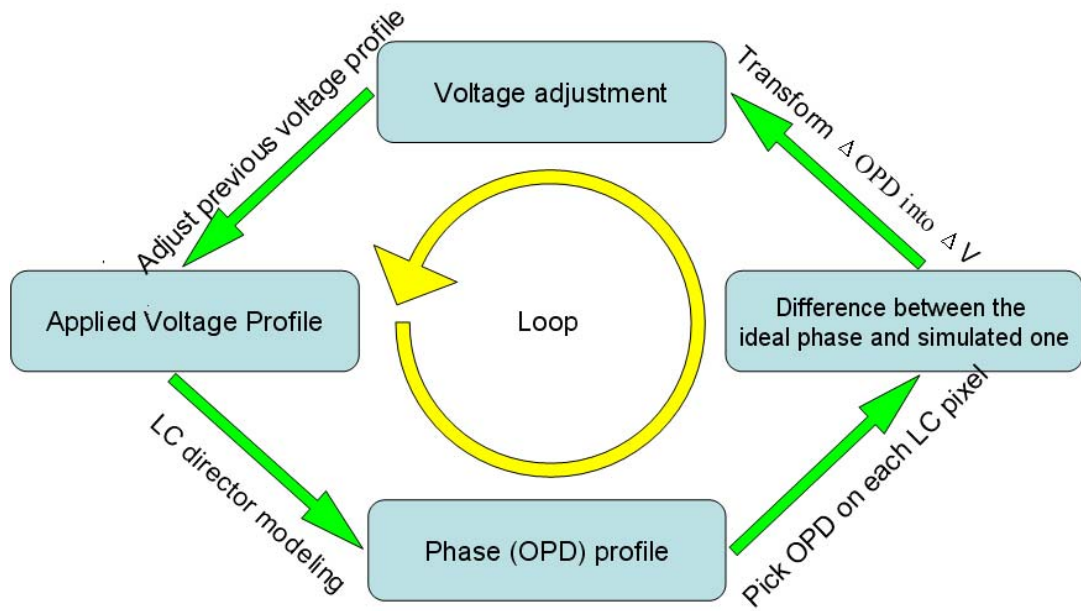


Fig. 2.7 Optimization loops to implement optimized LC micro-lens phase profile with applied voltage profile modification

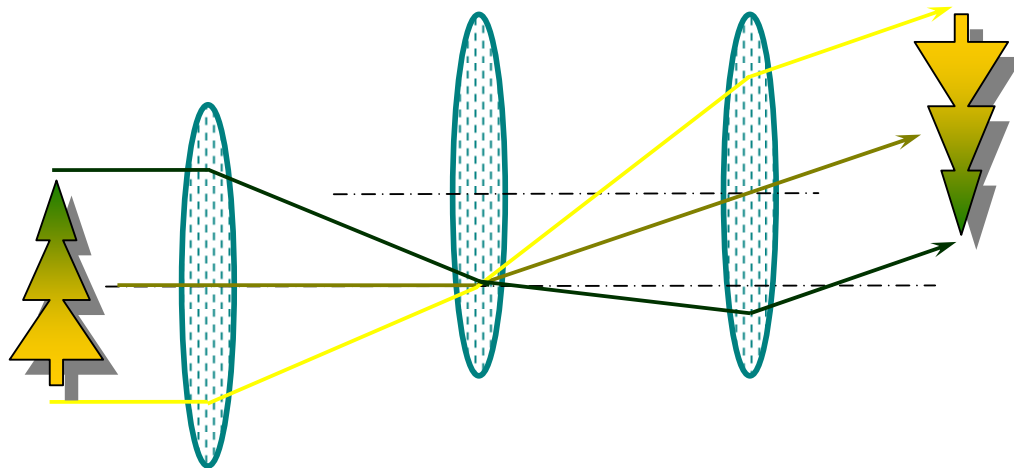


Fig. 2.8 “Flipping effect” in the all positive LC decenter lens cascade

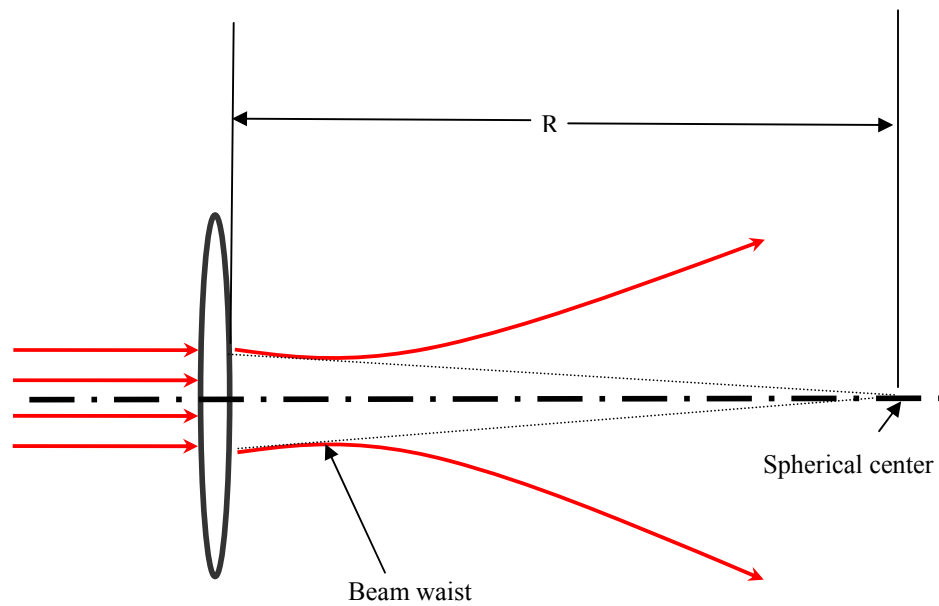


Fig. 2.9 “Ill lens” in the case of a positive lens incident with Gaussian of large R
 where the spherical center is far from the beam waist

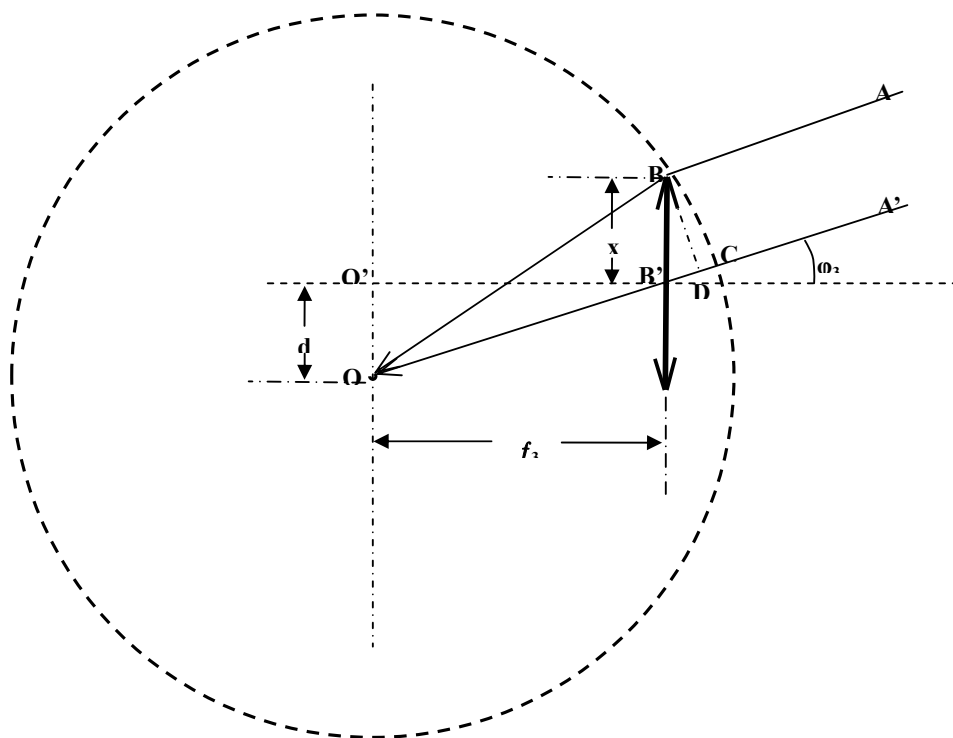


Fig. 2.10 Off-axis aberration of a single positive lens

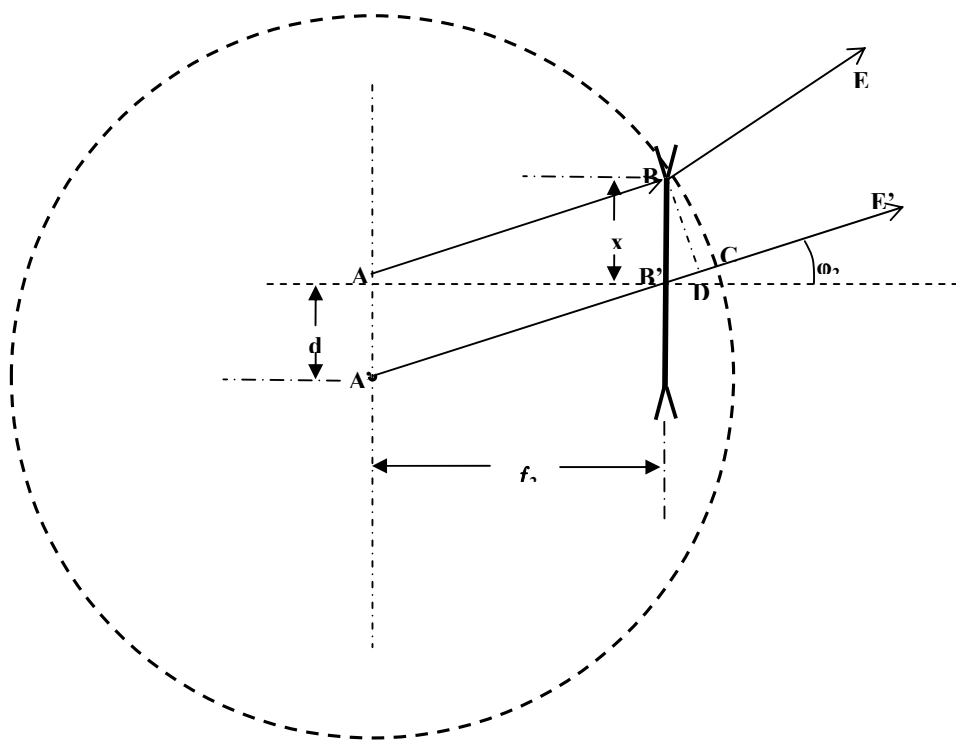


Fig. 2.11 Off-axis aberration of a single negative lens

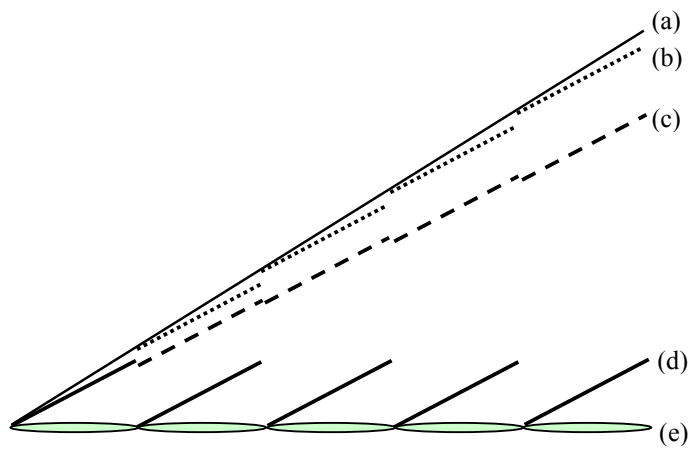


Fig. 2.12 Phase up correction for third positive micro-lens layer

(a) Ideal Phase for designed wavelength; (b) Phase of E_{3b} with 2π phase up; (c)

Unfolded phase of E_{3b} ; (d) Phase profile of E_{3b} ; (e) Third layer lens

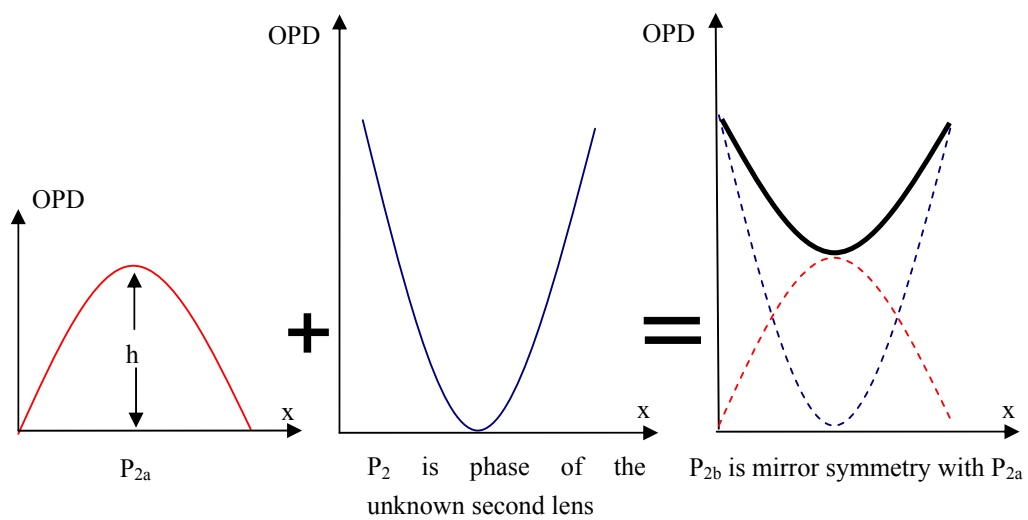


Fig. 2.13 Algorithm of mirror symmetry correction of the second lens phase profile

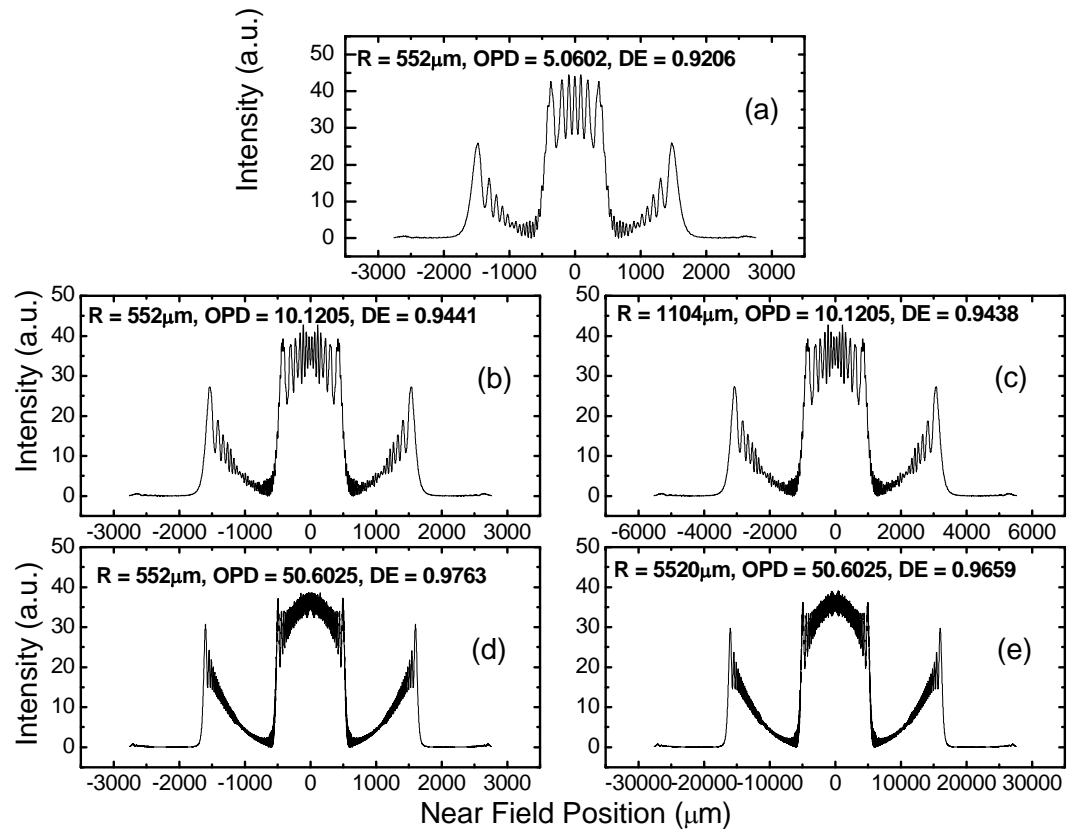


Fig. 2.14 Near field intensity profile for a non-steered positive DLA (5 lenses in each layer) as a function of OPD and diameter

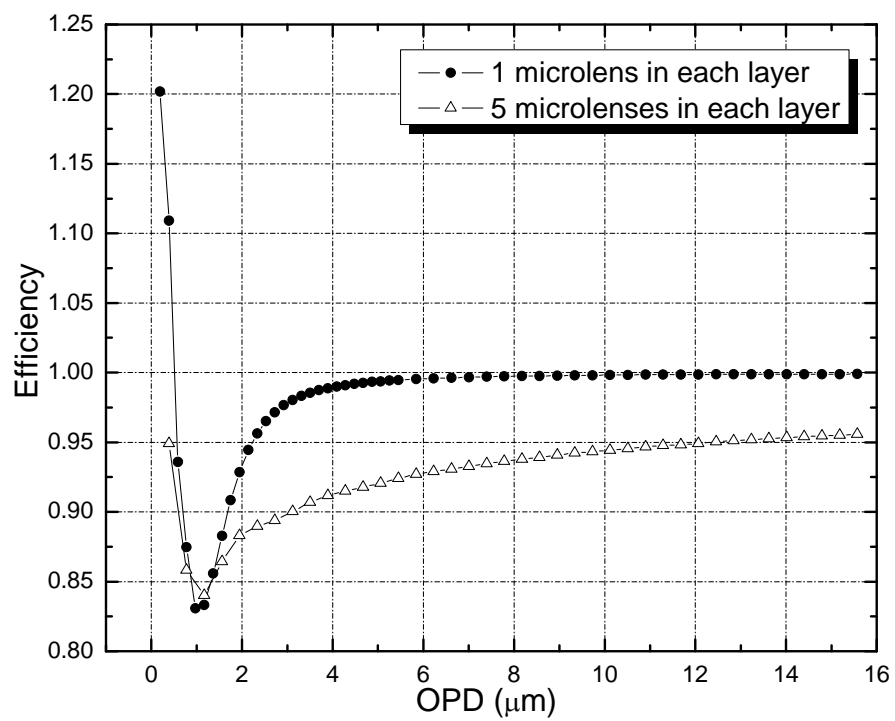


Fig. 2.15 OPD range of a robust all positive micro-lens array

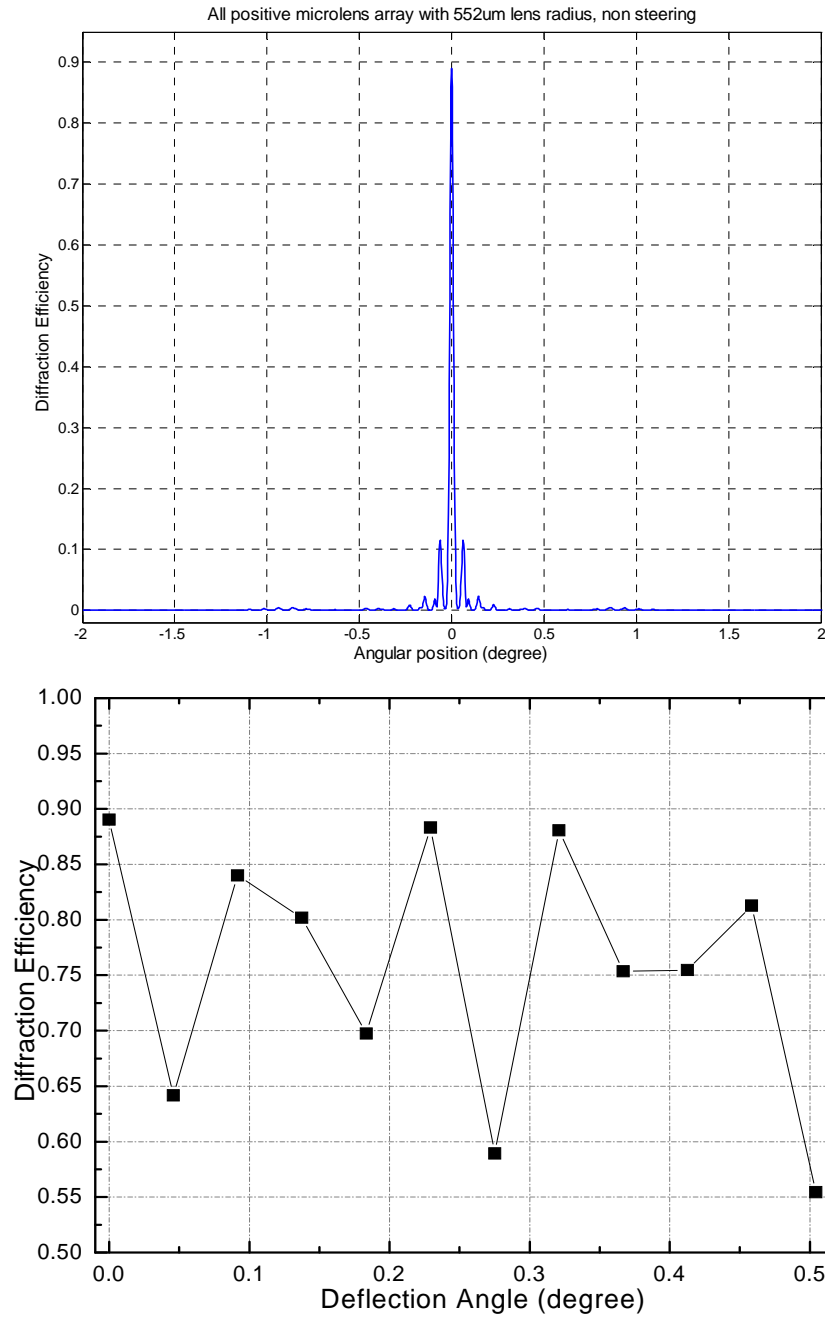


Fig. 2.16 All positive micro-lens array with 552 μm radius

(a) Far field Intensity for non steering

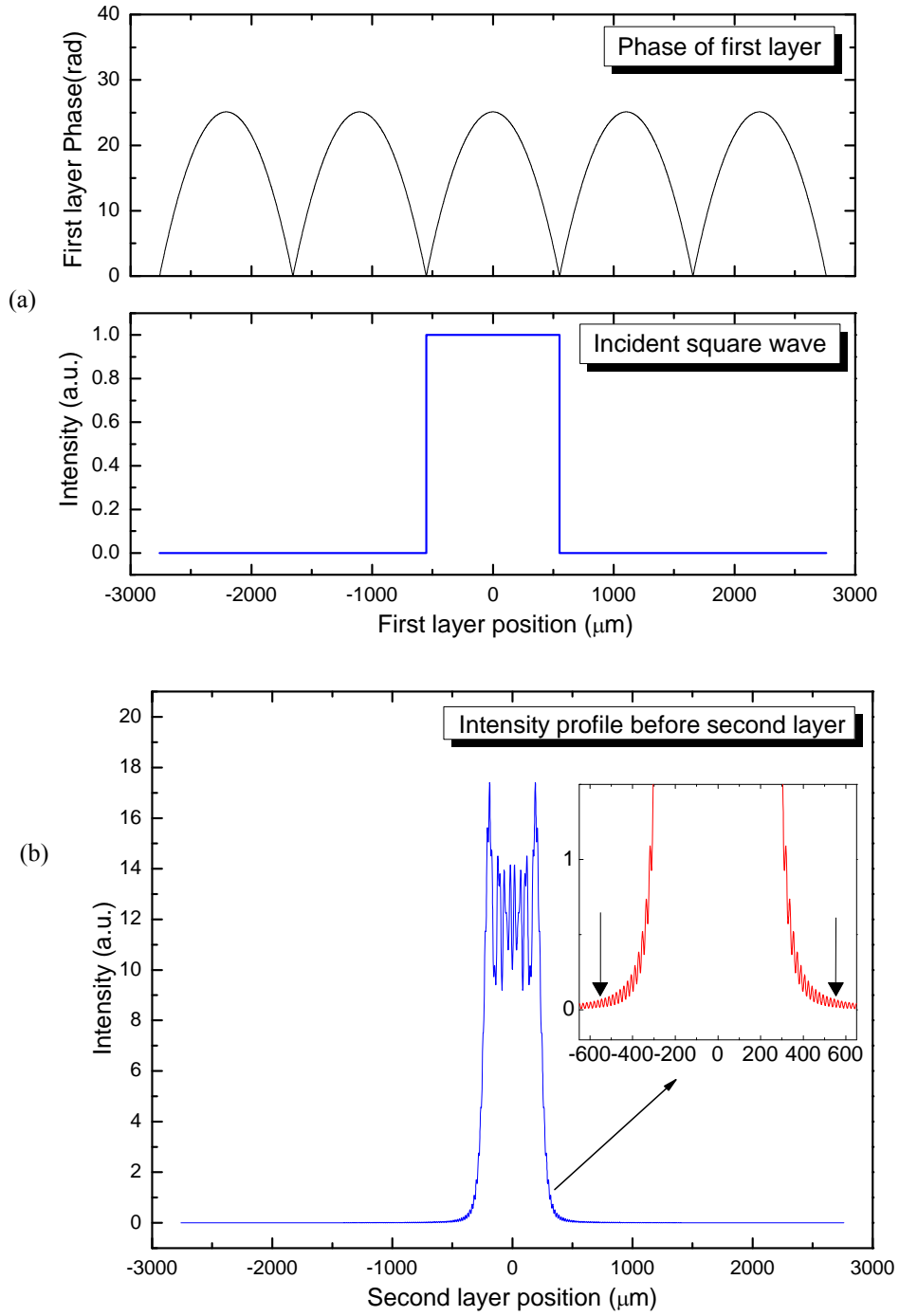


Fig. 2.17 (a) Incident square wave and first layer phase profile of mixed micro-lens

array; (b) out-of-lens leakage right before the second layer

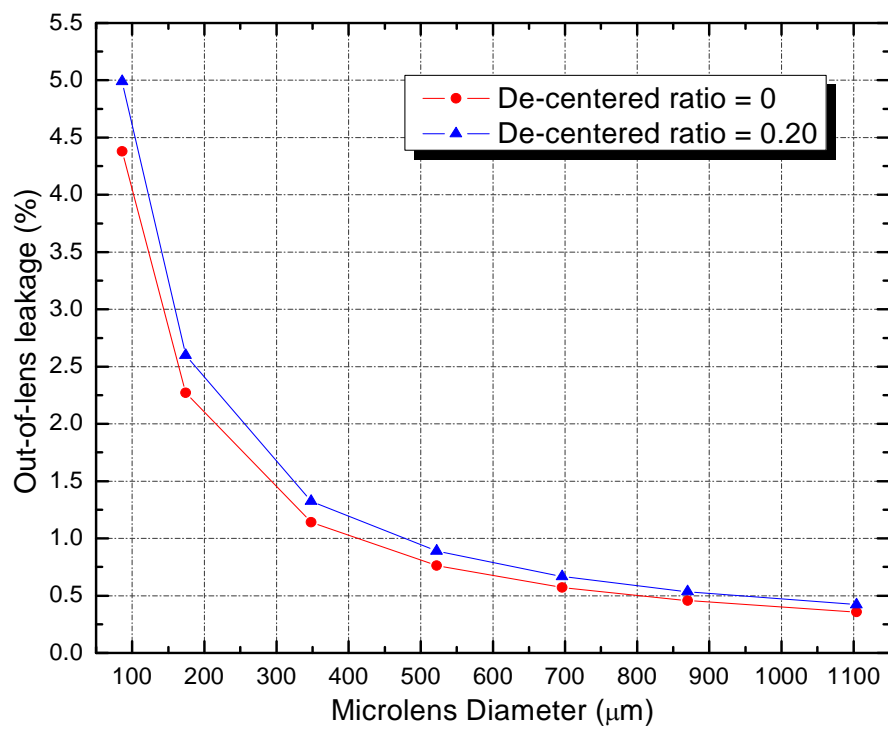


Fig. 2.18 Out-of-lens leakage with respect to the diameter of micro-lens

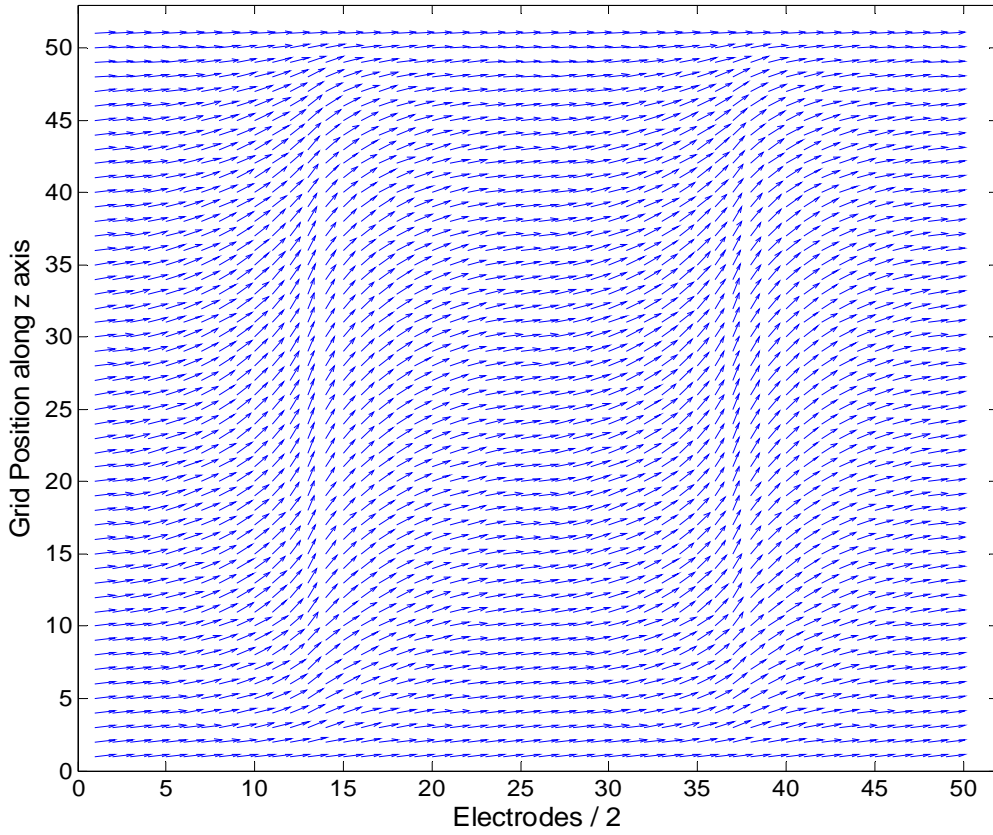
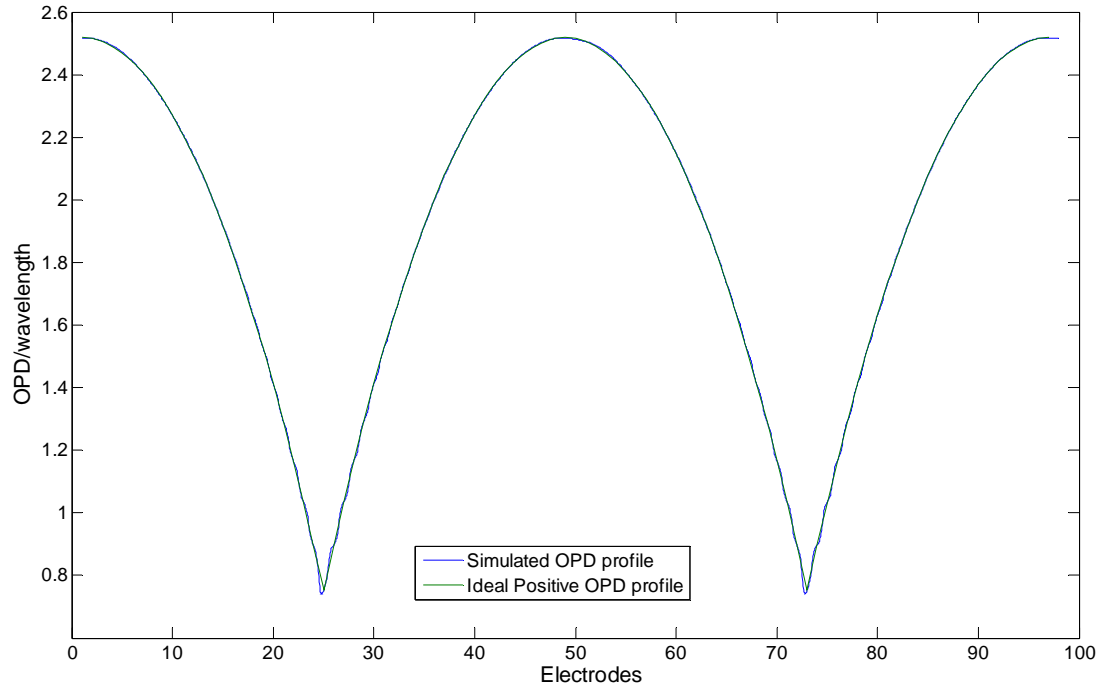


Fig. 2.19 (a) OPD profile of a positive LC layer; (b) director configuration of a

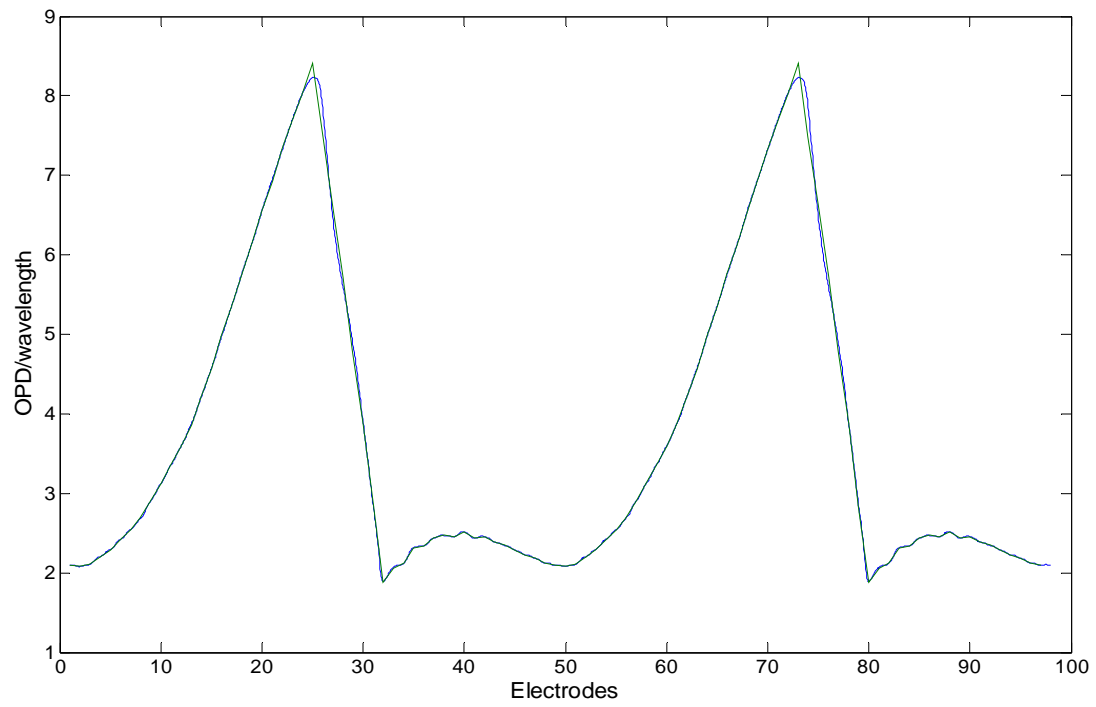
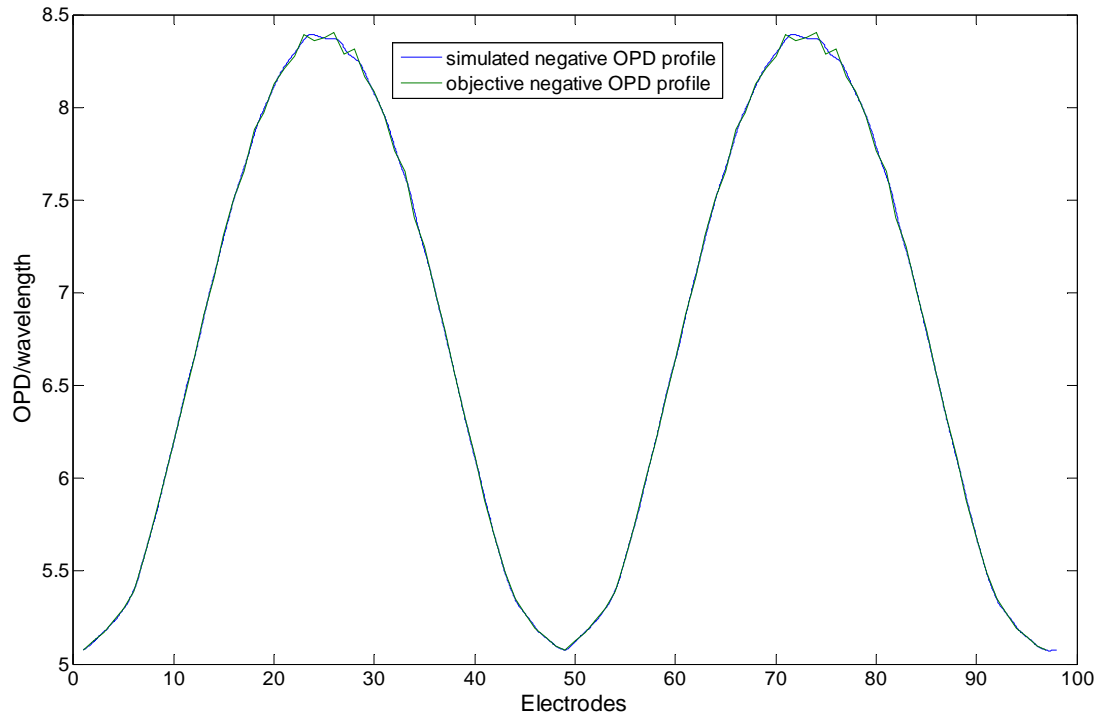


Fig. 2.20 (a) OPD profile for a negative LC lens with steering angle = 0°

(b) OPD profile for a negative LC lens with steering angle = 0.64°

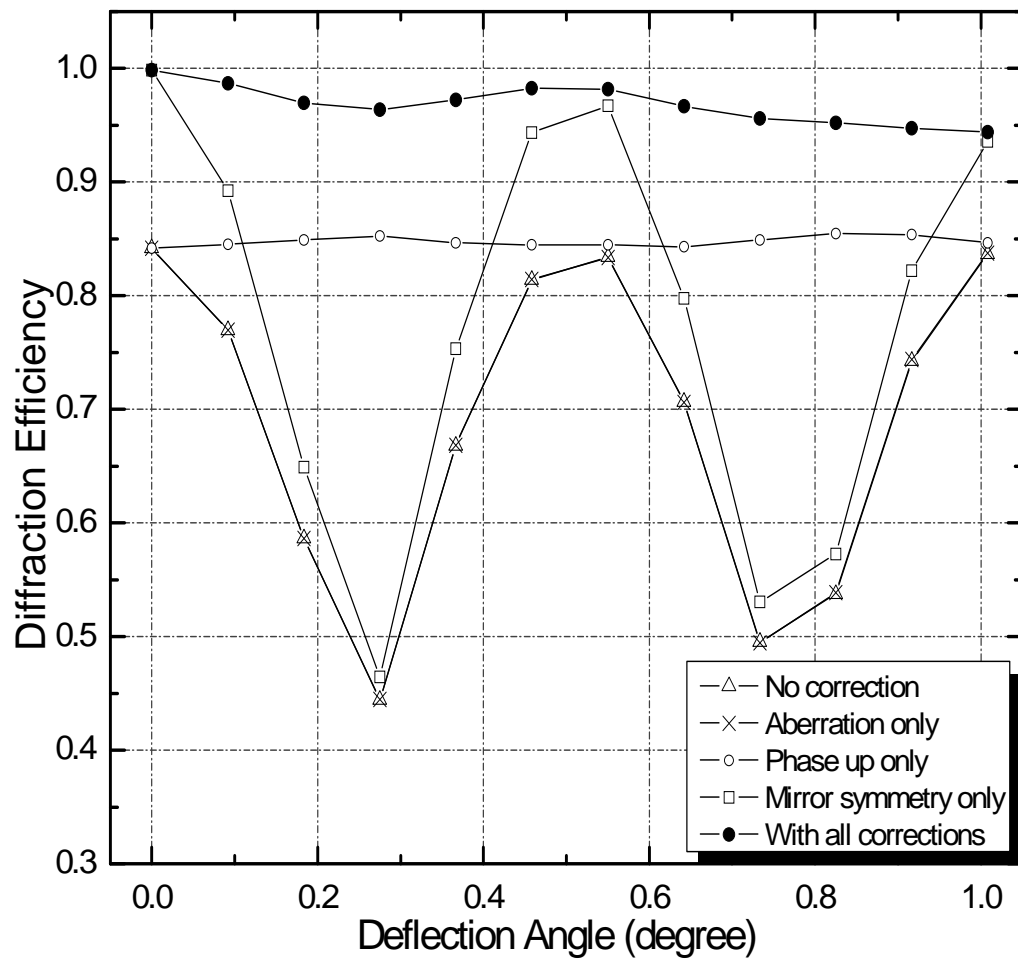


Fig. 2.21 Contributions to the final diffraction efficiency by the three different correction approaches

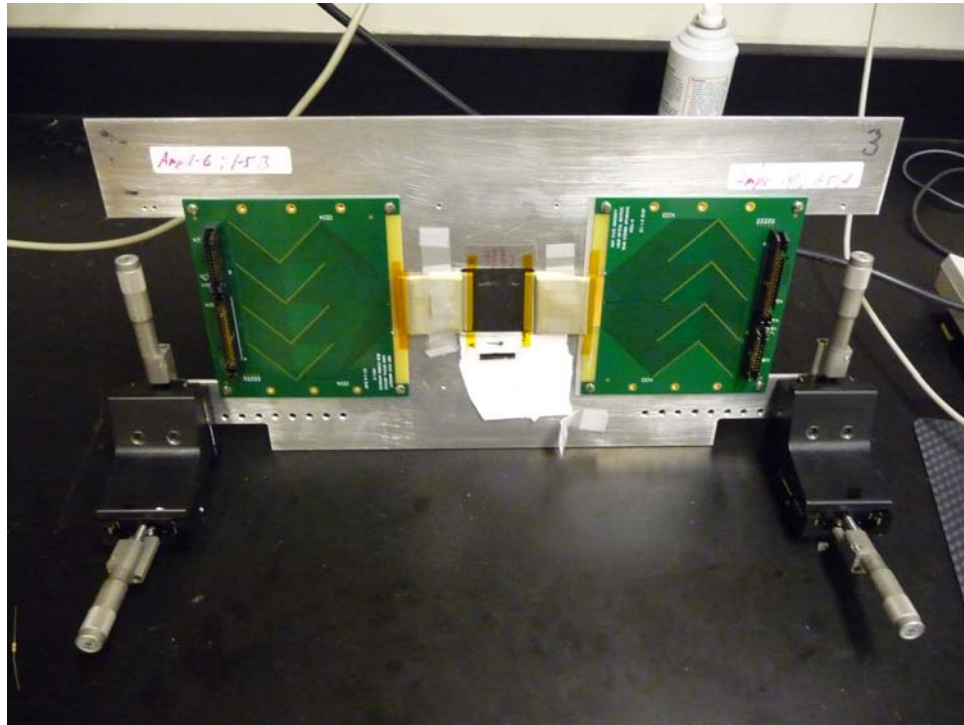


Fig. 2.22 A positive LC-DLA layer connected with interface board

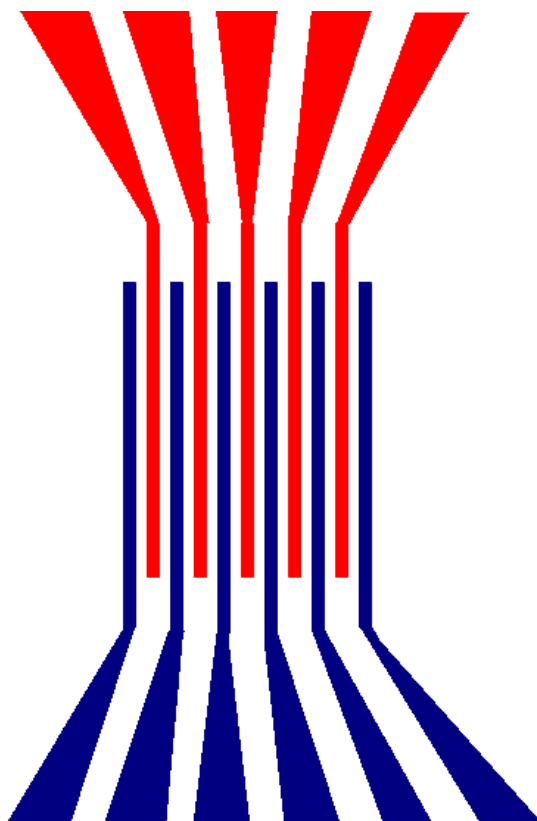


Fig. 2.23 Inter-digital electrode pattern with fan-out region (part) in one substrate of LC-DLAs

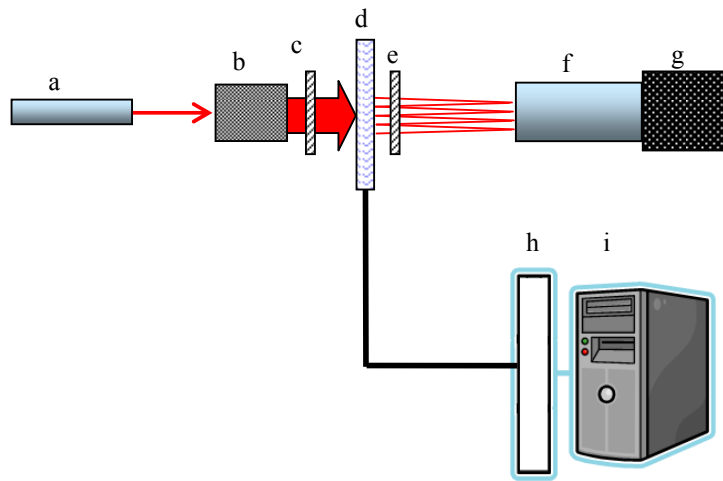


Fig. 2.24 Schematic diagram of beam profile measurement of LC micro-lens
 He-Ne laser 632.8nm; (b) beam expander; (c) polarizer; (d) LC micro-lens; (e)
 polarizer; (f) signal collect lens system; (g) PULNiX camera; (h) Amplifier; (i)
 Controlled computer with Labview program.

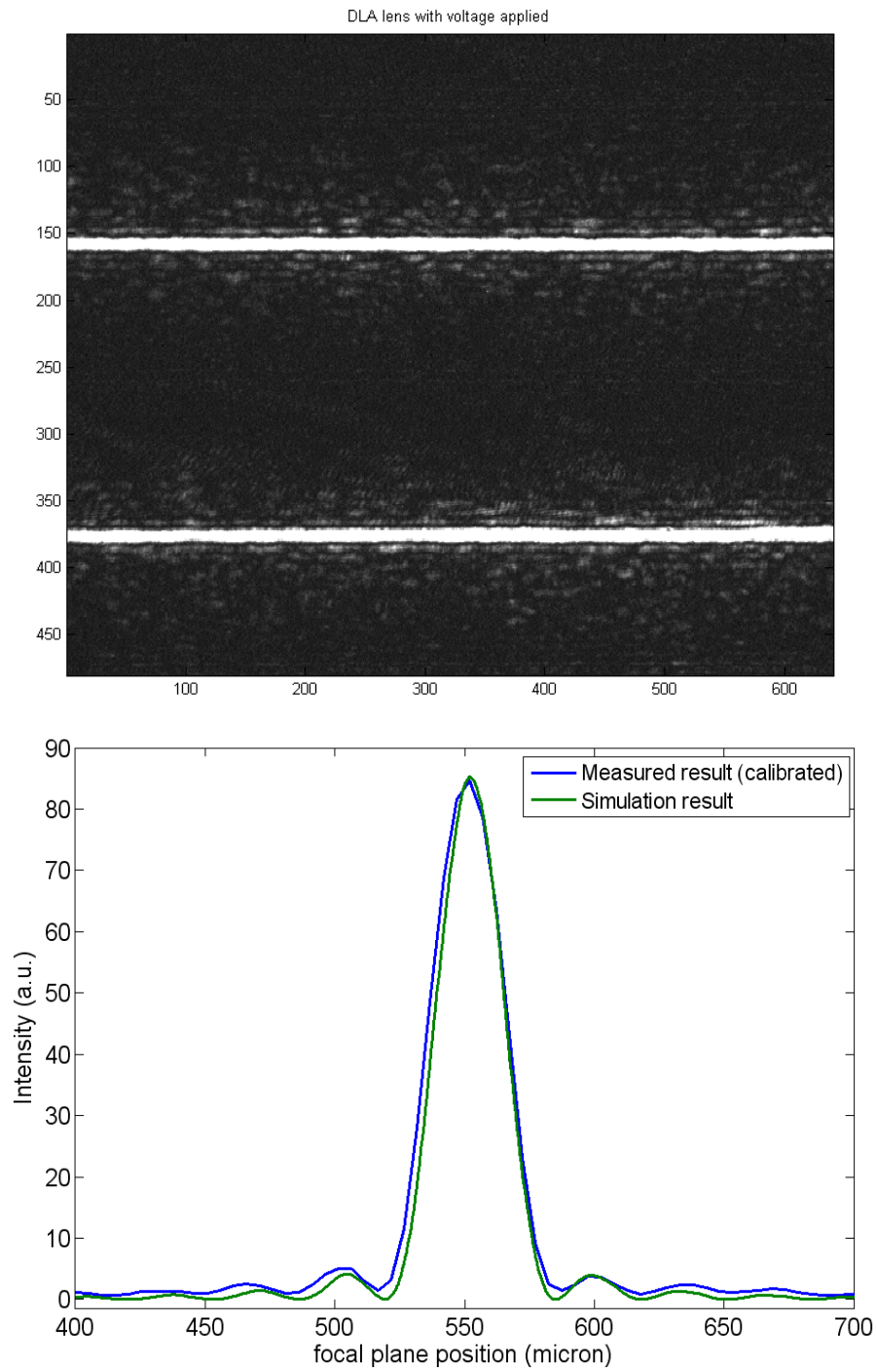


Fig. 2.25 Positive LC-DLA layer (a) beam profile image of the 25 μ m positive microlens LC layer at focal plane; (b) Intensity profile with comparison of

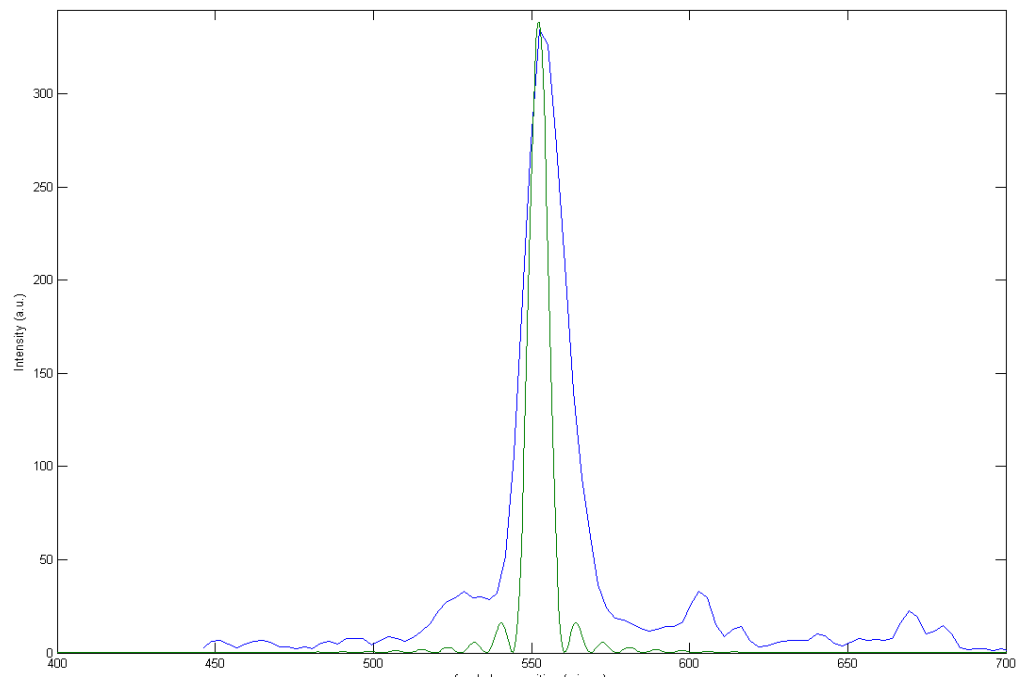
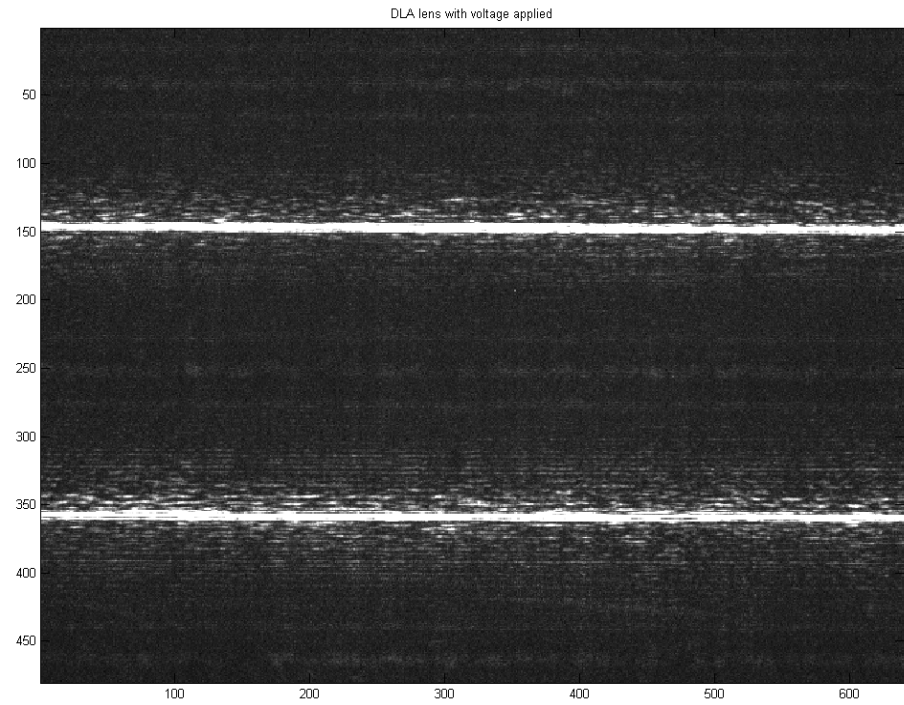


Fig. 2.26. (a) beam profile image of the 50 μ m negative microlens LC layer at focal plane

(b) Intensity profile with comparison of simulated results

Note: the voltage profile is for positive lens but with same focal length as the negative one

Chapter 3

Tunable liquid crystal polarization gratings

3.1 Introduction

Traditionally in the liquid crystal beam steering devices, for instance, the LC optical phased arrays (LC-OPAs), LC prisms, and LC decentered micro-lens arrays in Chapter2, their steering mechanisms are based on the spatially varying retardation $\Delta n \cdot d$ (Δn is the effective birefringence, and d is the LC cell thickness) of liquid crystal material. These liquid crystal based devices follow the basic idea of generating a linear change of optical path difference (OPD) across the aperture, which tilts the incident phase front and thereby steers the optical beam.²⁶ To achieve an optimized performance of continuous steering in this category, either a large thickness d of LC cell (such as LC prisms or the middle LC lenslet in mixed LC-DLA system) is employed to achieve a large gradient over a large aperture with a continuous phase profile; or the periodical resets is used to form the phase profile whose OPD step is an integer number of wavelengths of the light (such as LC-OPAs). The large value of d leads to slow response, absorption and scattering of light by the device. The resets in Fig.1.2, if mathematically ideal, would not be a large problem for a single frequency wavefront, however, in real devices they are well known that they degrade the achievable device efficiency since it is very hard to obtain an ideal programmed reset profile in the continuous Liquid crystal director configurations.

In this chapter, a tunable liquid crystal polarization grating is proposed and studied from a new viewpoint. This approach toward generating a phase gradient is based on Pancharatnam's

“QH” method.²⁷

Fig.1.6 shows the optical model of the QH device of Pancharatnam: A light beam passes through a polarizer, a Quarter-wave plate ($\lambda/4$ plate), a Half-wave plate ($\lambda/2$ plate), another Quarter-wave plate, and another polarizer.

The incident light becomes a circular polarized light after the first $\lambda/4$ plate, so that the light incident on the half-wave plate can be defined as E_{in} according to Jones Calculus notation:

$$E_{in} = \begin{bmatrix} Ex_{in} \\ Ey_{in} \end{bmatrix} = \begin{bmatrix} Ex_{in} \\ i \bullet Ex_{in} \end{bmatrix}. \quad (3.1)$$

For convenience, we assume it is a right hand circular polarized light.

The transmitted light leaving the half-wave plate, E_{out} , is defined as a linear mapping of the incident light E_{in} by a Jones Matrix which represents the $\lambda/2$ plate:

$$\begin{aligned} E_{out} &= R \bullet P \bullet R^{-1} \bullet \begin{bmatrix} Ex_{in} \\ Ey_{in} \end{bmatrix} \\ &= \begin{bmatrix} \cos \beta & -\sin \beta \\ \sin \beta & \cos \beta \end{bmatrix} \bullet \begin{bmatrix} 1 & 0 \\ 0 & e^{i\varphi} \end{bmatrix} \bullet \begin{bmatrix} \cos \beta & \sin \beta \\ -\sin \beta & \cos \beta \end{bmatrix} \bullet \begin{bmatrix} Ex_{in} \\ i \bullet Ex_{in} \end{bmatrix}. \end{aligned} \quad (3.2)$$

Where R and P are defined as rotation and phase matrices of the $\lambda/2$ plate respectively, β represents the angle between the slow axis of the $\lambda/2$ plate and the x axis, and φ is denoted as the phase retardation of the $\lambda/2$ plate, which is equal to π here. The final relationship can be simplified

$$\begin{aligned} \text{as: } E_{out} &= \begin{bmatrix} \cos^2 \beta + e^{i\varphi} \sin^2 \beta & \cos \beta \sin \beta (1 - e^{i\varphi}) \\ \cos \beta \sin \beta (1 - e^{i\varphi}) & \sin^2 \beta + e^{i\varphi} \cos^2 \beta \end{bmatrix} \bullet \begin{bmatrix} Ex_{in} \\ Ey_{in} \end{bmatrix} \\ &= \begin{bmatrix} Ex_{in} e^{i \bullet 2\beta} \\ -i \bullet Ex_{in} e^{i \bullet 2\beta} \end{bmatrix}. \end{aligned} \quad (3.3)$$

In the Eq.(3.3) for the light leaving the half-wave plate, the transmitted light is a left hand circular polarized light with a common phase factor $\exp(i \cdot 2\beta)$, which is the most important result

from the simple model. The phase of the transmitted circular light can be accurately controlled by the azimuthal angle β . Considering Fig.1.6, where the half-wave plate is followed by polarizer and quarter wave plate that convert the circularly polarized light back to a linearly polarized state, the main point is that we have linear polarization in and linear polarization out with a phase shift due to the rotation of the half-wave plate.

The above result can be applied to a device where the slow axis of the half-wave plate rotates about the device normal. If we have a LC cell of half-wave optical retardation, with an in-plane director configuration where the azimuthal angle linearly rotates from 0 to π , the final spatial phase profile of circularly polarized transmitted light will linearly change from 0 to 2π . If the gradient in this azimuthal angle is constant with the rotation angle increasing along a particular direction (the x axis in Fig.3.1), a device with linearly increasing phase without any “reset” or discontinuity is obtained. Theoretically, given such an ideal in-plane spiral director configuration in Fig.3.2(a,b), with an incident circular polarized Gaussian beam with appropriate wavelength to meet the half-wave retardation condition, the exiting light will characterize with a phase profile in the near field as shown in Fig.3.3, combined to be a circular polarized light with the x and y component. The final diffraction efficiency in the far field pattern of Fig.3.4 can reach to 99.6% that is unprecedented. Diffraction gratings that are operated by periodically modulating the state of the polarization of transmitted light through them are generally named as “polarization gratings”.³⁹⁻⁴⁰ As far as the very thin thickness (only half-wave retardation) is concerned, the light loss from absorption and scattering can be minimized.

Several research groups have reported work based on the LC polarization gratings. Crawford and co-workers have demonstrated a LC diffraction grating through a polarization holography

exposure on a linear photo-polymerizable polymer alignment layer.³³ They disclosed several switchable LC polarization gratings based on the planar-periodic patterned surface alignment layers. Honma et al. have shown a lens fabricated through a micro-rubbing technique and demonstrated the liquid crystal gratings consisting of multidomain alignment regions fabricated through a microrubbing technique.³² Escuti et al. report their experimental results of a liquid crystal polarization grating (LCPG) modulating unpolarized light with high contrast for the first time. They also report LC polarization grating to modulate unpolarized or polarized light with a grating period as small as $6.3\mu\text{m}$ and observe nearly ideal diffraction into the first order at $> 99\%$ for monochromatic light.³⁴ These striking results have demonstrated the validity of this basic idea of what is called a polarization grating.

Unfortunately, all the above QHQ methods have utilized different alignment techniques to generate a fixed azimuthally distributed LC director. The devices are switchable, in that their steering effect can be turned on or off through the application of an electric field along the device normal, but are not continuously variable.

In summary, on one hand previously demonstrated continuously variable optical beam steering devices based on an increasing OPD need “resets” that limit the efficiency of the device. While on the other hand, high efficiency beam steering devices based on the Pancharatnam QHQ concept have been demonstrated, but they are not continuously variable.

It is the objective of our work to demonstrate a high efficiency, continuously variable, optical beam steering device that is based on the Pancharatnam QHQ concept which compromise the advantages of the above two different categories of devices: tunable and high diffraction efficiency.³⁵ In addition to the convention name of liquid crystal polarization gratings (LCPG), we

also call our device a V-COPA device because it is based on the OPA idea, but has a Continuous phase profile, and uses Vertical alignment.

3.2 Tunable liquid crystal polarization grating concept

At the beginning of this work, we tried a lot of efforts to develop the tunable LCPG based on some novel electrode patterns with a uniform planar surface alignment to trigger and formalize the in-plane spiral director configuration. However, it turned out no matter what the electrode pattern is, from the topology point of view, the uniform planar alignment at surface always contradicts forming the in-plane spiral configuration in the bulk. That is the cause the LCPG researches choosing all kinds of techniques to first formalize a strong anchoring surface alignment with in-plane spiral configuration. Given the specific spiral surface alignment of liquid crystal cell, the period and rotation sense of the LCPG is thereby determined and the period length is equal to the period of surface alignment and can not be tuned anymore.

To obtain a tunable LCPG, an ideal surface alignment might be characterized with the following three features: first, it should assist the initialization of the in-plane polarization gratings; second, it should not prohibit the tuning capability of the period of the polarization grating; third, the surface alignment should be consisted with few domains that are as simple as possible to reduce the difficulties of alignment fabrication. In our design, a quasi vertical alignment with slightly modulation of the polar/azimuthal angle in three specific regions of the surface will satisfy all the above requirements.

The tunable LCPG device in this chapter uses a vertical alignment and a LC material that has a negative dielectric anisotropy. In the next chapter of dynamics of LCPG, we will employ the dual

frequency LC material to enhance the performance of the tuning speed. The basic idea is that when a voltage profile is applied, the LC director will lie in the plane of the cell, but without a strong planar surface anchoring imposed in-plane direction. This allows for the pitch of the spiral (and the beam steering angle) to be changed. Two aspects of the design that need to be considered are: how is the initial spiral pattern formed, and how is it changed.

One way we have considered to form an initial, defect free, spiraling director configuration in the plane of the cell, is to slightly modify the vertical alignment as will be explained here with reference to Fig. [3.5](#).

In Fig. [3.5](#), the alignments at the bottom substrate are shown in the red arrows. They are approximately vertical, and the alignments at the top substrate (not shown) are identical as the one at bottom substrate. We call this a quasi-vertical alignment because the alignment is not exactly vertical in some domains, which are slightly tilted to the $+y$ and $-y$ directions (the director rotates about the x axis with alternating signs to tip in and out of the plane of the drawing). The red arrows near the bottom substrate in the cone represent the orientation of the surface alignment over the electrodes region. The alignment in region B and the two electrodes near B slightly tilts to the $+y$ with 88° polar angle (measured relative to the surface), while alignment in region D and the two electrodes near D tilts to $-y$ with 88° polar angle. All the other regions (such as the gap between the electrodes) are exactly vertical with 90° polar angles. A liquid crystal material with the negative dielectric anisotropy $\Delta\epsilon$, is used so that when an electric field is applied, the LC director will tilt to lie in the x - y plane. The directors in the LC bulk over region B will lie in the x - y plane and towards the $+y$ axis, while directors over region D will also lie in the x - y plane but towards $-y$ direction. To orient the directors of region A or C along $+x$ or $-x$ axis direction, we

employ a specific voltage profile with voltage offsets and the vertical surface alignment. For example, the voltage profile on the electrodes of bottom substrate is: 10, 12, 12, 12, 10, 10, 10, 12V; and 0, 2, 2, 2, 0, 0, 0, 2V on the top. The above voltage profile will lead to the fringe field between the electrode #1 and #2, electrode #4 and #5, etc. The director in the region *A* (between electrode #1 and #2) will try to reorient perpendicular to the fringe field from the voltage offset. Given an initial vertical director in the region *A* near the surface, to be consistent with the vertical surface alignment, the director will reorient along the equi-potential line in the x-z plane to minimize the free energy of the system when the fringe field of the voltage offset is applied. With these specific regions' orientations determined, one full period of spiral of grating in the bulk of LC cell can be formed in the x-y plane.

In a word, we consider that the RMS average voltage applied to the entire cell is approximately the same, but a DC offset, that is a function distance along the x axis in Fig. 3.5 is employed to effect the spiral configuration. It is anticipated that at a location where the DC offset is changed to a higher value, the director will tend to orient in the x-z plane with the director rotated slightly from the horizontal with a particular rotational sense about the y axis. On the other hand, at another location where the DC offset is changed to a lower value, the director will tend to orient in the x-z plane with opposite rotational sense about the y axis from the horizontal. The intended effect of this will be to “trap” a pi-rotation of the director between these two locations. The DC offset is changed through the use of patterned electrodes. To illustrate this procedure, we can decompose the whole formation of grating into several snapshots as shown in Fig. 3.6.

It is interesting to know what the result is if we apply a “flip” offset of voltage profile from the initial vertical state, such as 12, 10, 10, 10, 12, 12, 12, 10V; and 2, 0, 0, 0, 2, 2, 2, 0V on the

bottom and top substrates respectively. This “flip” offset voltage profile will also result in an in-plan spiral director configuration but with an opposite sense of rotation compared with the previous results, as shown in Fig. 3.7. We may define the clockwise rotation of sense as “+” state, while the counterclockwise rotation of sense as “-” state, and the initial vertical state as “0” state. Either “+” or “-” state can be formed from “0” state with identical initial configuration and surface alignment. This simple algorithm implies a fast three states switching device when we switch the offset of voltage profile from the initial vertical state, for example, from “+” state to “0” state, next from “0” state to “-” state, then from “-” state to “0” state, et al.

To vary the pitch of the spiral, the location the DC offset changes can be moved by changing the voltage offset profile applied to the electrodes. Note that the director configuration in region A or C (Fig. 3.5) will be bonded with the offset region. Once the location of voltage offset region is shifted, the corresponding region A or C will also be translated. The quasi vertical surface alignment will not prohibit the formation of any direction in x-y plane with applied voltage. A vertical director configuration in a region can be lie toward any of direction in x-y plane theoretically. Therefore the bond regions can be easily moved from on location to another. Because of the trapped pi-rotation between their locations, if they are moved closer together, the pitch will be shortened. Similarly, we can expand the period of LCPG by move these two “bonds” away. Now we will simply introduce this approach and the equilibrium state modeling result. In chapter 4, we will focus on the dynamics study of the period tuning and propose a faster solution to tune the LCPG device.

Combining the modified vertical alignment, with the “adjustable” voltage profile, the V-COPA device can have a defined, tunable, defect free, initial spiral director structure.

3.3 Numerical Jones Calculus of Tunable LCPGs

Based on the above description of our tunable LCPG, we simulate the establishment of the initial polarization grating and also demonstrate the tuning capability of the device. We develop a specific modeling tool (V-COPA v3.0, as introduced in appendix I) to study the formation of liquid crystal polarization grating and their optical characteristic. The LC modeling is based on the LC3D subroutine with the applied voltage profile given by several separated stripe electrodes on both of top and bottom substrates with the same numerical modeling algorithm in Chapter 2. The optics simulation from near field to far field is implemented by Kirchhoff's scalar integral method introduced in the Chapter 2. The light passing through the LCPG cell is calculated by Jones Calculus that will be introduced in the following.

Fig.3.8 shows the 2D rectangular grid points representing the director configuration in the LCPG. Each grids can be represented by $n_x(i,j,k)$, $n_y(i,j,k)$, and $n_z(i,j,k)$. (i, j, k) is the index of each grid along x, y and z axis. There are total Numx grids along x axis, and Numz grids along z axis. In 2D modeling, j is equal to 1. We can treat each row of the lattice as one layer, and in each layer we will perform the Jones Calculus for the wavefront of all the grids from 1 to Numx that exits that layer, and the transmitted wavefront will be regarded as the incident beam for the next layer until the light exit the last layer represented by Numz. For every grid on each layer, the phase retardation of ordinary and extraordinary light can be defined by the birefringence:

$$\begin{aligned}\varphi_o(i, j, k) &= \frac{2\pi \cdot \Delta d \cdot n_o(i, j, k)}{\lambda} \\ \varphi_e(i, j, k) &= \frac{2\pi \cdot \Delta d \cdot n_{eff}(i, j, k)}{\lambda}\end{aligned}\tag{3.4}$$

Where Δd is the layer thickness, ordinary refractive index n_o is identical for all grids, the effective extraordinary refractive index n_e is given by the director configuration:

$$n_{eff}(i, j, k) = \frac{n_o(i, j, k) \cdot n_e(i, j, k)}{\sqrt{(n_o^2(i, j, k) \cdot \sin^2(\beta) + n_e^2(i, j, k) \cdot \cos^2(\beta))}} \quad (3.5)$$

Where β is $\pi/2 - \theta$, here θ is the polar angle given by $\text{asin}(n_z(i, j, k))$.

Know the polar and azimuthal angle on each grids, the Jones matrix on the grid can be calculated by:

$$J(i, j, k) = \begin{pmatrix} A & B \\ B & D \end{pmatrix} \quad (3.6)$$

$$A = \cos^2(\alpha(i, j, k)) \exp(i \cdot \varphi_e(i, j, k)) + \sin^2(\alpha(i, j, k)) \exp(i \cdot \varphi_o(i, j, k))$$

$$B = \cos(\alpha(i, j, k)) \cdot \sin(\alpha(i, j, k)) \cdot (\exp(i \cdot \varphi_e(i, j, k)) - \exp(i \cdot \varphi_o(i, j, k)))$$

$$D = \sin^2(\alpha(i, j, k)) \exp(i \cdot \varphi_e(i, j, k)) + \cos^2(\alpha(i, j, k)) \exp(i \cdot \varphi_o(i, j, k))$$

Apply the Jones matrix on each grid times with the incident beam $E_{in}(i, j, k)$, we will the $E_x(i, j, k)$ and $E_y(i, j, k)$ and final field with x and y component. Transforming the near field to the far field is implemented by the Kirchhoff's scalar integral.

3.4 Modeling results of tunable LCPGs

3.4.1 Establishment of a spiral director configuration

As an example of a device built with the V-COPA concept, we consider a $5\mu\text{m}$ (gap thickness d along z axis) cell filled with negative dielectric anisotropy ($\Delta\epsilon$) LC (MLC-6608): $\Delta\epsilon = -4.2$, $n_o=1.4748$, $n_e=1.5578$, the elastic constant $K_{11}=16.7$ pN, $K_{22}=7.0$ pN, $K_{33}=18.1$ pN. The LC cell,

as shown in Fig.3.5 consists of top and bottom substrates with patterned electrodes. The electrode stripe's width w_e (along x axis) is $4\mu\text{m}$, the length l_e is $1\mu\text{m}$ (along y axis), and the gap width w_g between each electrode is $1\mu\text{m}$.

To control the DC offset along the x direction while maintaining a constant RMS voltage, for example, voltages in the bottom electrodes can be 10, 12, 12, 12, 10, 10, 10, 12V, while 0, 2, 2, 2, 0, 0, 0, 2V are applied on the top.

Using the above LC parameters and modeling tool (V-COPA v3.0) we demonstrate the formation of a defect free spiral structure based on our concept. Initially the director field is determined by the surface alignment condition with no electric fields applied (nearly homeotropic). Then voltages are applied to the 8 electrodes (bottom electrodes: 10, 12, 12, 12, 10, 10, 10, 12V; top electrodes: 0, 2, 2, 2, 0, 0, 0, 2V). After LC directors relax to the equilibrium state by the vector field method, we can get the final director configurations as shown in Fig.3.9 where a nearly perfect spiral director configuration is formed. The arrows represent the director orientation, while the curves are the equipotential field line. We can define the period of the spiral configuration as the distance between the regions where the director is substantially along the y axis in the figure. We will refer to those regions as the Y-regions. Note that the Y locations are between the locations x_1 and x_2 in Fig.3.9 (as the x values where the potential steps up and down respectively). Please note the twist sense of the helix (as observed in the top view of Fig.3.9) would be opposite if the voltages on the bottom electrodes were exchanged (10V exchanged with 12V), and if the voltages on the top electrodes were also exchanged. A three-state switching digital beam deflector can be realized by this procedure.

3.4.2 Tuning the period of the spiral gratings

After the initial spiral director configuration is achieved, by translating the regions where the director is trapped in the x-z plane, we can expand or shrink the period of the grating. This is accomplished by moving the locations of the steps in the potential (x_1 and x_2). For this demonstration, instead of using periodical boundary condition, a “stress-free” boundary condition is used at the x locations of the left and right sides of the computed area shown in Fig.3.10 and 3.11. The director orientation at these boundaries is determined by a linear extrapolation from the three grid points closest to the boundary along the x direction.

To show the ability to modify the spiral pattern we start with the director configuration in Fig.3.9, and apply a new voltage profile to the LC cell, that is, 10, 12, 12, 12, 12, 10, 12, 12V on bottom electrodes; 0, 2, 2, 2, 2, 0, 2, 2V on top ones. Loading the previous director structure in Fig.3.9 as the initial starting configuration, the director will reach a new equilibrium state. In Fig.3.10, is shown the new director configuration with equipotential lines. It can be seen that due to the change in the applied potential, the x_2 and x_1 region on the right side of the figure are moved toward each other, while the x_1 region on the left side is held in position. By then changing the voltage profile on bottom to 10,10,12,12,12,10,12,12V, then 10, 10, 10, 12, 12, 10, 12, 12V, and then to 10, 10, 10, 10, 12, 10, 12, 12V, (with similar schemes on top electrodes), we can move the x_1 region on the left side of Fig.3.10 toward the right, while holding the position of the x_2 regions in Fig.3.10. The final resulting potential and director configuration is shown in Fig.3.11.

While Fig.3.10 and 3.11 demonstrate the concept of controlling the director configuration of in this device, in many applications we are interested in changing the period of a spiraling director configuration. To demonstrate this, we can start with the director and potentials shown in Fig.3.9,

move the periodic boundary conditions to the new pitch length, and then adjust of voltages on the electrodes to provide the new director profile. Fig.3.12 shows the result of this procedure, where the left and right sides of this figure correspond to the new locations of the periodic boundary conditions. The location of the new boundaries were placed in the director profile of Fig.3.9 at the x values of 9.75 and 29.75, and the voltages on the electrodes in the included region was changed to 10, 12, 12, 10, 10V, on the bottom and 0, 2, 2, 0, 0V on the top. The new spiral period is 10.25 microns.

3.4.3 Optical efficiency of tunable LCPGs

Using the Jones Calculus and scalar integral modeling methods and cell parameters previously described, we calculate the far field intensity pattern for the case of calculated periodic spiral director fields with the periods shown in the previous section. In these calculations a linear polarized beam (632.8nm) passes through the QHQ system in Fig.1.6, except the $\lambda/2$ plate is replaced by the V-COPA LC cell. A Gaussian profile beam is used as shown in Fig.3.13(a).

Fig. 3.13(b) is calculated for the spiral period of 15.75 μm shown in Fig.3.9 and shows a deflection angle of 2.302 degrees and a steering efficiency of 98.27%. In Fig. 3.13(c), the transmitted light across a smaller spiral period (10.25 μm) from Fig.3.12 is also calculated, showing a steering angle of 3.54 degrees with and efficiency of 96.77%. Once the desired director configuration is established it will likely be possible to apply a uniform voltage to the top and bottom electrodes (for example 10 volts on all of the top electrodes and 0 on the bottom). When doing this, we find the efficiency climbs to very close to 100%.

It is interesting to investigate the dispersion effect of the LCPG device. Known by Eq.(3.4), as

far as the different wavelength of incident light is concerned, given a fixed applied voltage profile, the requirement of half-wave retardation can not be satisfied for some other wavelengths, even we assume the birefringence is constant and wavelength independent. Our LCPG design with vertical alignment can resolve this issue easily, within a certain range of wavelength, we can modify the overall value of RMS voltage (for example, 10V used in previous example), squeeze or expand the n_z component across the LC bulk, to meet the half-wave retardation condition. However, even this half wave retardation requirement is met, in the LCPG device, not like the LC-OPA device that the steering angle is only related to the Δn and the length of period, the steering angle of LCPG is given by Eq. (3.7) and is obviously wavelength dependent.

$$\theta = \sin^{-1}\left(\frac{\lambda}{\Gamma}\right) \quad (3.7)$$

Where Γ is length of period, θ is the steering angle.

Therefore, for different wavelength of incident light, the deflection angle will be different. Additional angular calibration component should be used to compensate this dispersion error when the broad band application is concerned.

3.4.4 Discussion of modeling results

A key aspect of the V-COPA device is the trapping of a pi-twist region of the in-plane director configuration through the use of voltage offsets.

As may be clear from inspecting Fig. [3.9- 3.11](#), this is accomplished, in part, by the fixing of the director in the x-z plane in the regions x_1 and x_2 . A director fixed in this way “traps” a pi-twist of the director in the space between them. The sense of this twist is fixed by the initial spiral sense (set by the spatially patterned quasi-vertical surface alignment and the DC offsets).

The reason why the director at the regions x_1 and x_2 near the surfaces is oriented as shown is primarily due to the torques imposed on it by the electric field and the vertical surface alignment layer. Because the liquid crystal material used has a negative dielectric anisotropy, the director (especially in the high field region near the surface) will tend to align perpendicular to the electric field direction. This effect coupled with the effect of the alignment layer to tilt the director perpendicular to the surface, causes the director to tend to align perpendicular to the axis of the electrodes and along the equipotential lines.

The above results show that a device built as described can provide exceptional performance. However modifications of this example device can be considered. For examples, two-frequency LC materials could be used (details in Chapter 4). Also, flexo-electric or smectic C materials can be considered for the used liquid crystal. Other types of optical devices, such as lenses, can be made by causing the spiral to have a spatially dependent period.

3.5 Fabrication and characterization of tunable LCPGs

3.5.1 Fabrication of tunable LCPGs

3.5.1.1 Three-domain quasi vertical surface alignment

To realize the above design and modeling results, the first task is to obtain the three-domain quasi vertical alignment that has been implemented by Dr. Ke Zhang in liquid crystal institute of Kent State University. Polyamic acids SE-1211 is used as the quasi-vertical surface alignment medium, since SE-1211 has a long alkyl sidechain that promotes the vertical alignment of liquid crystals. By varying the baking temperature and the rubbing times and strength, we will obtain different controlled pretilt angle closed to 90° .

Fig.3.14 shows the detailed procedures to fabricate the three-domain patterned quasi-vertical alignment. First we spin coat SE-1211 on the ITO substrate with electrode pattern for 5 seconds of 500 rpm, and thereafter 20 seconds of 2000 rpm, and soft baking at 95°C for 2 minutes, and hard baking at 200°C for 1 hour. Soft-baking is the step during which almost all of the solvents are removed from the SE-1211 mixture. Hard-baking is necessary in order to harden the side-chain and improve adhesion of SE-1211 to the wafer surface. The un-rubbed vertical alignment layer is thereby formed on the substrate. Second we will coat the photoresist material (S-1818 with ratio of 1:3) on the SE-1211 coated ITO substrate for 5 seconds of 500 rpm, and thereafter 30 seconds of 1500 rpm, and soft baking at 95°C for 2 minutes. In the next step, attaching the designed photo-mask on the coated substrate, shining the UV light for 6 to 10 seconds, we are able to register the first alignment domain, for example, polar angle of 88° and azimuthal angle of 90°, in the regions as shown in Fig.3.14. After rinsed by deionized water and dried by air, we perform the first round of rubbing (5 to 10 times with rubbing block depends on the pretilt angle requested). Washing off the photoresist by a series of steps including P-thinner for 60 seconds, deionized water rinsing, methanol rinsing, deionized water rinsing, isopropanol rinsing, and dried in oven at 80°C for 10 minutes. Repeat the step 2 to step 5 to register the second alignment domain. By this procedure, a patterned ITO substrate with three-domain quasi vertical alignment is ready to be assembled and be filled with liquid crystal materials (MLC-6608).

To remove the defects in the bulk, further thermal treatment is also conducted on LC cell with three-domain surface alignment. First we apply high voltage (5V) to the cell. Heating the cell to the isotropic phase with voltage applied. Then cool down the system slowly with 5 dpm to the room temperature with voltage applied to obtain a uniform vertical director configuration in the

bulk of LCPG.

3.5.1.2 Patterned ITO substrate

In this work, both of the bottom and the top substrate will be accurately controlled with inter-digital electrodes coated on the substrates by photolithography technique. We design the electrode pattern and assemble the LC cell with four arms of electrode bonds as shown in Fig. [3.15](#). All the electrodes are applied voltage that controlled by the Labview program.

3.5.2 Polarized Optical Microscopy of tunable LCPGs.

As we predicted the director configurations of the initialization procedure of the V-COPA device for the single frequency material with a negative dielectric anisotropy, we have fabricated a V-COPA LC cell with the initial period of $23\text{ }\mu\text{m}$ filled with MLC-6609, a liquid crystal material with negative dielectric anisotropy of -3.7 at the temperature of $+20^{\circ}\text{C}$ and the applied voltage of 1 kHz . The surface alignment is approximately similar to the configuration in Fig. [3.5](#), except the different alignment domains are interchanged with 1 pixel, not three pixels in Fig. [3.5](#). The photo of the device with four interface board is shown in Fig. [3.16](#). For the initialization process, we apply the following voltage profile: 10, 12, 10, 12, 10, 12, 10...V on the electrodes of bottom substrate and 0, 2, 0, 2, 0, 2, 0...V on the top. The polarized microscopy verifies the periodical in-plane spiral director configuration in Fig. [3.17\(a\)](#) as alternate dark-bright bands from the view of polarized microscope. In the case of crossed polarizers that are parallel and perpendicular to the electrodes, Region *A* or *B* (in Fig. [1.7](#)) where the director is parallel or perpendicular to the electrodes will appear to be dark, while the transition region between *A* and *B* will be bright in the

polarized microscopy. The initial spacing between the dark bands is equal to the pixel spacing of electrodes as $23\ \mu\text{m}$. As long as the azimuthal angles of directors increase linearly along x or $-x$ axis, the dark-light bands will shift towards one uniform direction as shown in Fig. 3.17(b-c) when rotating the crossed polarizers. It demonstrates that the correct rotation sense and in-plane spirals are formed in the LCPG cell.

3.5.3 Characterization of tunable LCPGs

We use the jumping method (details will be introduced in Chapter 4: the dynamics of tunable LCPG) to tune the period of the single frequency V-COPA device. Based on the initial formed period, if continue to switch the voltage profile, the period of the grating can “jump” from the initial $23\ \mu\text{m}$ to $46\ \mu\text{m}$, $69\ \mu\text{m}$, and $92\ \mu\text{m}$, as shown in Fig. 3.18(a-d). For example, Fig. 3.18(a) is step 1 with the initial period with 10, 12, 10, 12...V on the electrodes of bottom substrate and 0, 2, 0, 2...V on the top. In Fig. 3.18(b) of step 2, we simply switch voltage profile to 10, 10, 12, 12, 10, 10...V on the bottom substrate and 0, 0, 2, 2, 0, 0...V on the top. Similarly, to obtain the period in Fig. 3.18(c) of step 3, we switch the voltage profile to 10, 10, 10, 12, 12, 12...V on the bottom and 0, 0, 0, 2, 2, 2...V on the top from step 2, and so on. The jumping steps must be performed in a correct sequence. One can not jump from step 1 to step 3 directly, otherwise the desired spiral configuration will not be obtained. It should be noted that during the transition process, disclination lines are formed due to the topological difference between the two states.

Given a circular polarized light at the wavelength of $1.5\ \mu\text{m}$ normally incident on the V-COPA device with the effective thickness of half-wave optical retardation, the transmitted light will deflect to the different steering angle as a result of period tuning. Initially, when the period

width is 23 μm , the deflected angle is 3.4° in Fig. 3.19(a). And different steering angles will be available, such as 1.7° steering angle for the period of 46 μm , etc, as shown in Fig. 3.19(b-d). When the requirements of half-wave retardation and constant gradient are met, the theoretical throughput of the deflected light will reach to 100% diffraction efficiency. The measured diffraction efficiency by peak ratio method is over 97.49% in Fig. 3.20 when the periods are in the range of 23 to 69 μm . However, when the width of period reaches to about 92 μm , the applied voltage profile will not be able to hold the gradient of the azimuthal angle of the directors as a constant, and the final efficiency will consequently drop to 70.46%.

One limitation of the above single frequency V-COPA is the tuning speed. It turns out that the response speed of the deflected light from 3.4° to 1.7° is about 650 ms. The response time will increase up to several seconds especially for the periods greater than 92 μm . To provide an adaptive beam steering technology with short response time, the need for the fast switching between different steering angles is critical. To resolve this issue and improve the tuning speed, in Chapter 4 we will concentrate on the dynamics mechanism of tunable LCPG device, and propose a dual-frequency LCPG with fast tuning capability.

In addition, as we described in section 2, we can easily implement a three-state switching device by flip the voltage offset profile, as shown in Fig. 3.21 and Fig. 3.22 with 1.5 μm of incident light switching between $+3.4^\circ$, 0° and -3.4° . The efficiency of each state is above 98%.

3.6 Summary

A tunable LCPGs device, that is characterized with an in-plane spiraling optic axis, has been studied in this Chapter. Employing a liquid crystal material with a negative dielectric anisotropy,

quasi-vertical surface alignment and an electric field with an offset voltage profile, excellent spiral configurations have been demonstrated. The resulting structure shows very high diffraction efficiency (95-98%). Compared with conventional LC prisms and OPA devices, the LCPGs device inherently has a continuous phase profile with no resets, while its thin (half wave retardation) cell thickness yields low absorption and low scattering. Moreover, the angle tune-ability of this device based on Pancharatnam's idea is achieved. Other optical devices such as electrically controlled lenses can also be envisioned based on this approach.

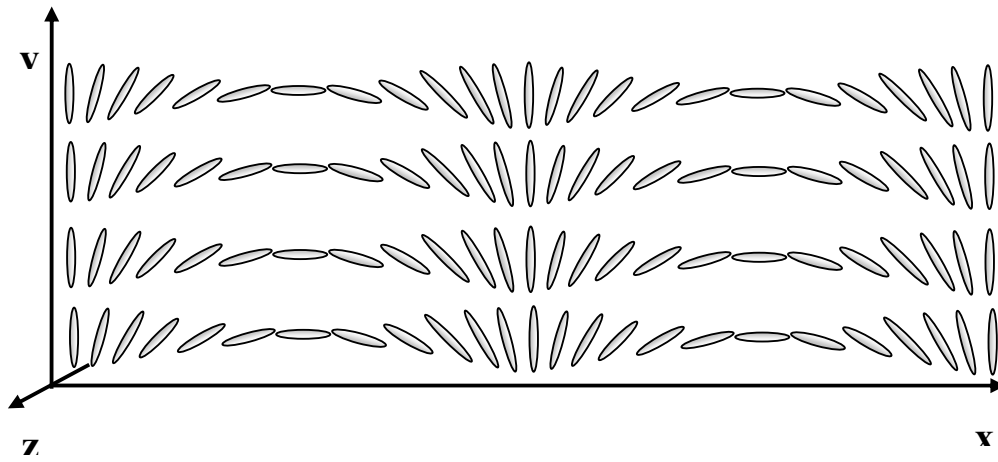


Fig. 3.1 The spatially varying orientation of the slow axis of the half-wave plate in the x-y plane of the LCPGs

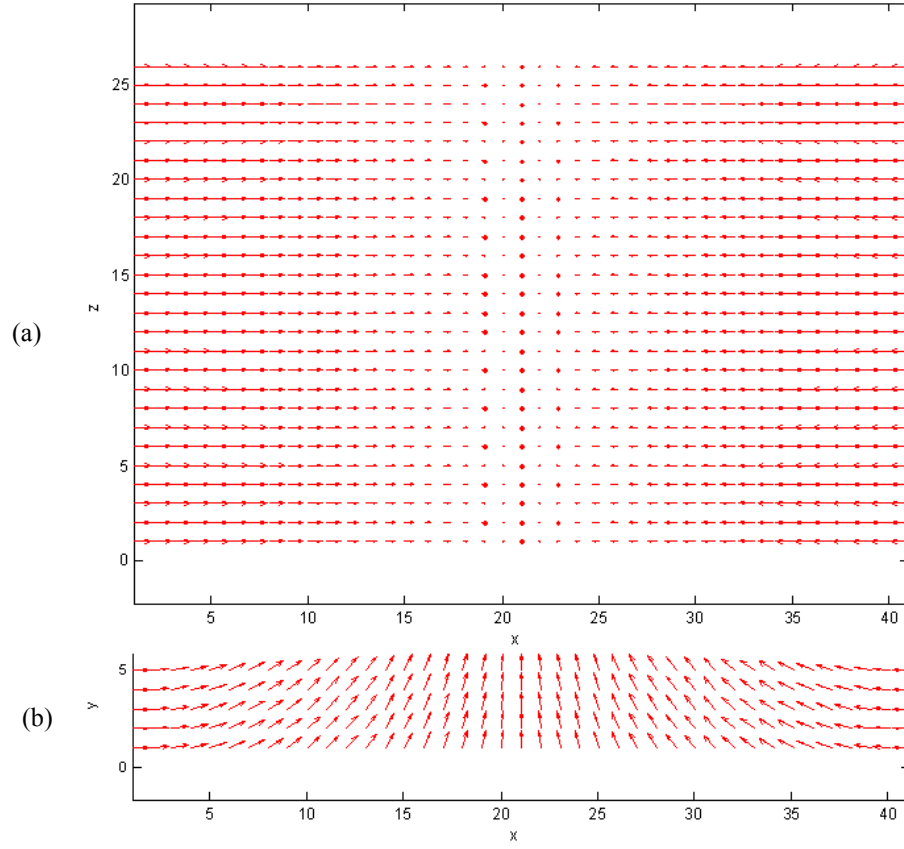


Fig. 3.2 Ideal director configuration of a LCPG device (one period)

(a) Side view of the LCPG director configuration

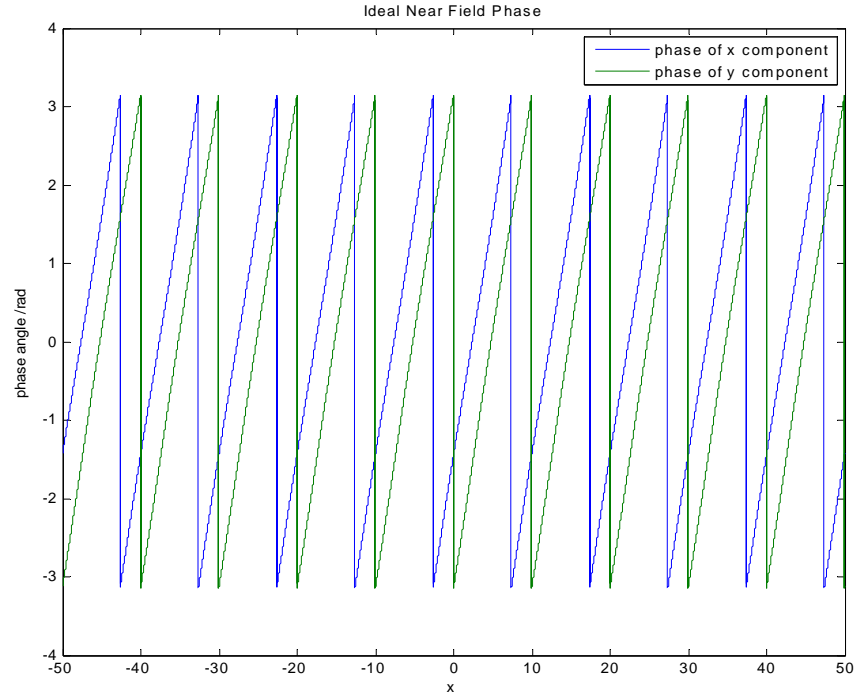


Fig. 3.3 Ideal phase profile of x and y component in the near field of a
LCPG device (with 10 periods)

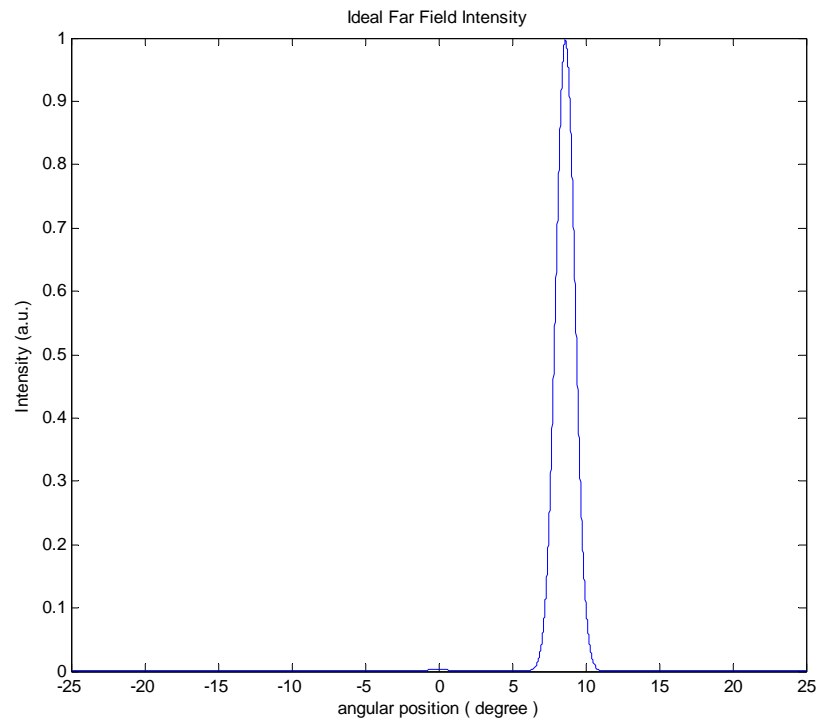


Fig. 3.4 Ideal diffraction pattern of intensity in the far field of a LCPGs device (with 10 periods)

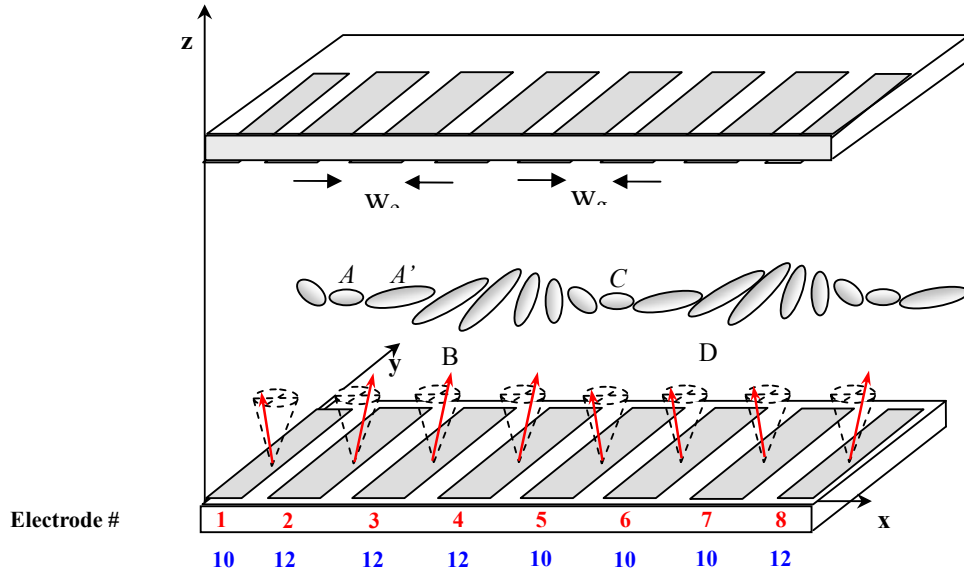


Fig. 3.5 A typical electrode pattern and in-plane spiral director configuration of a LCPGs device with 2 periods

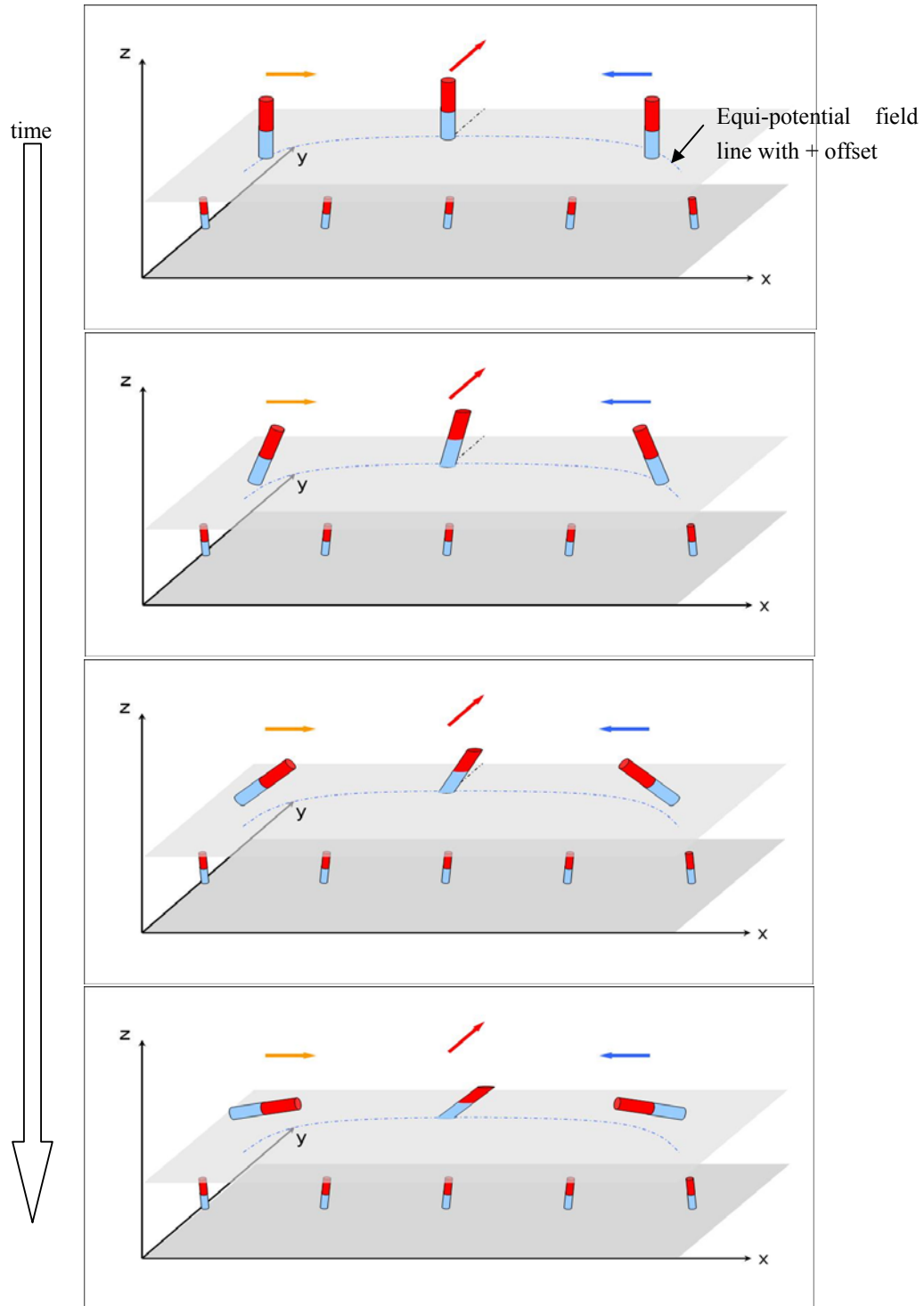


Fig. 3.6 Snapshots of the initialization of LCPGs (boundaries and center)

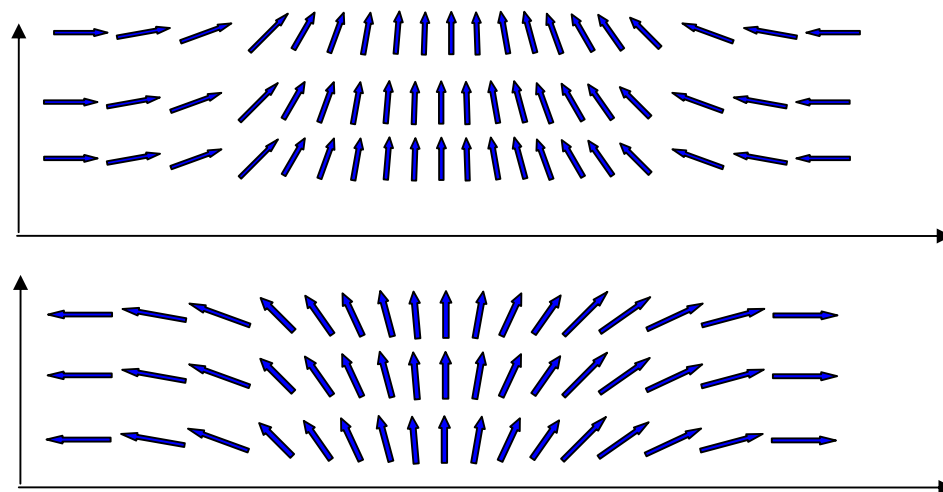


Fig. 3.7 Top view of director configuration of LCPGs in x-y plane:

Counterclockwise rotation of sense (– state, top one)

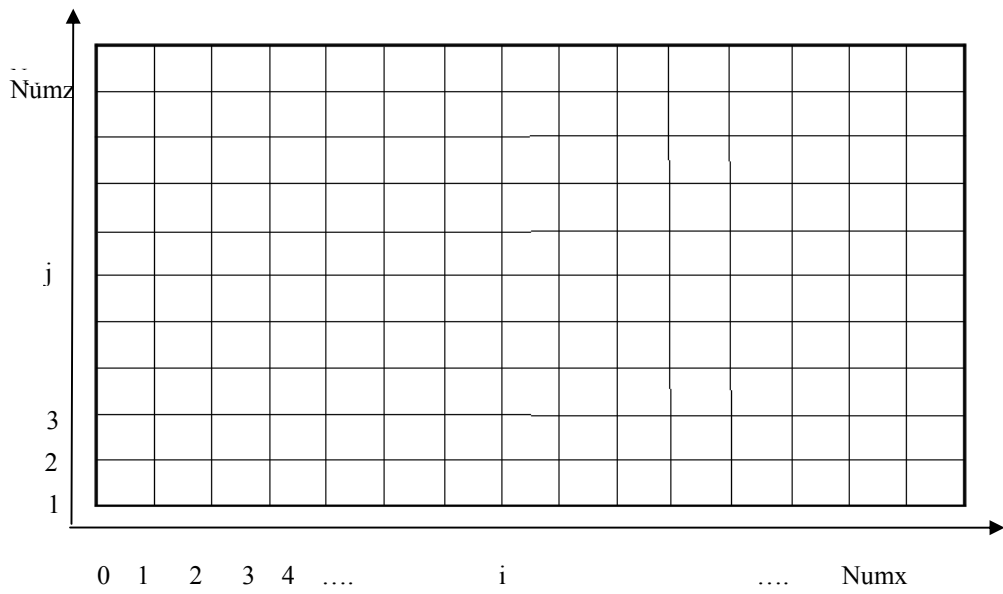


Fig. 3.8 2D rectangular grid of lattice for LC modeling and Jones calculus

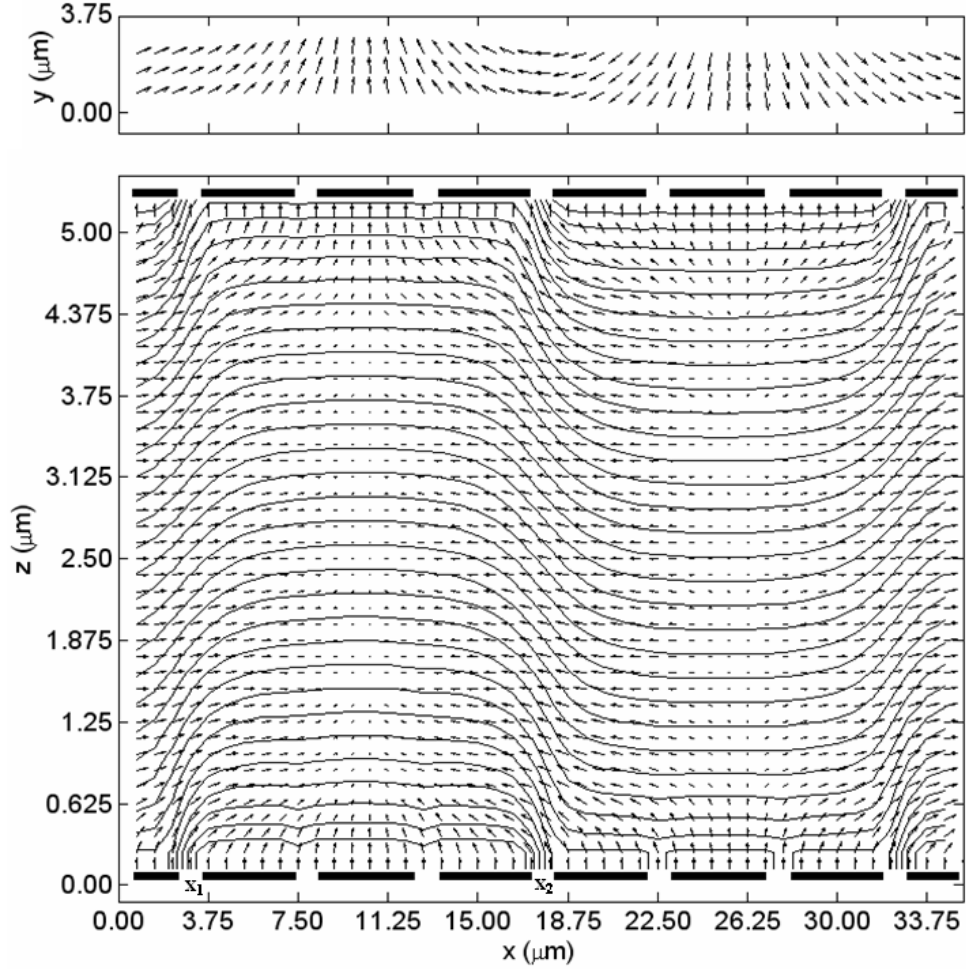


Fig. 3.9 Tunable LCPGs spiral grating starting with $15.75\mu\text{m}$ period

The top one is the view from normal of the cell and in the middle x-y plane along z. The bottom one is the side view of director configuration. The curves show the equipotential field with 0.33V between each level.

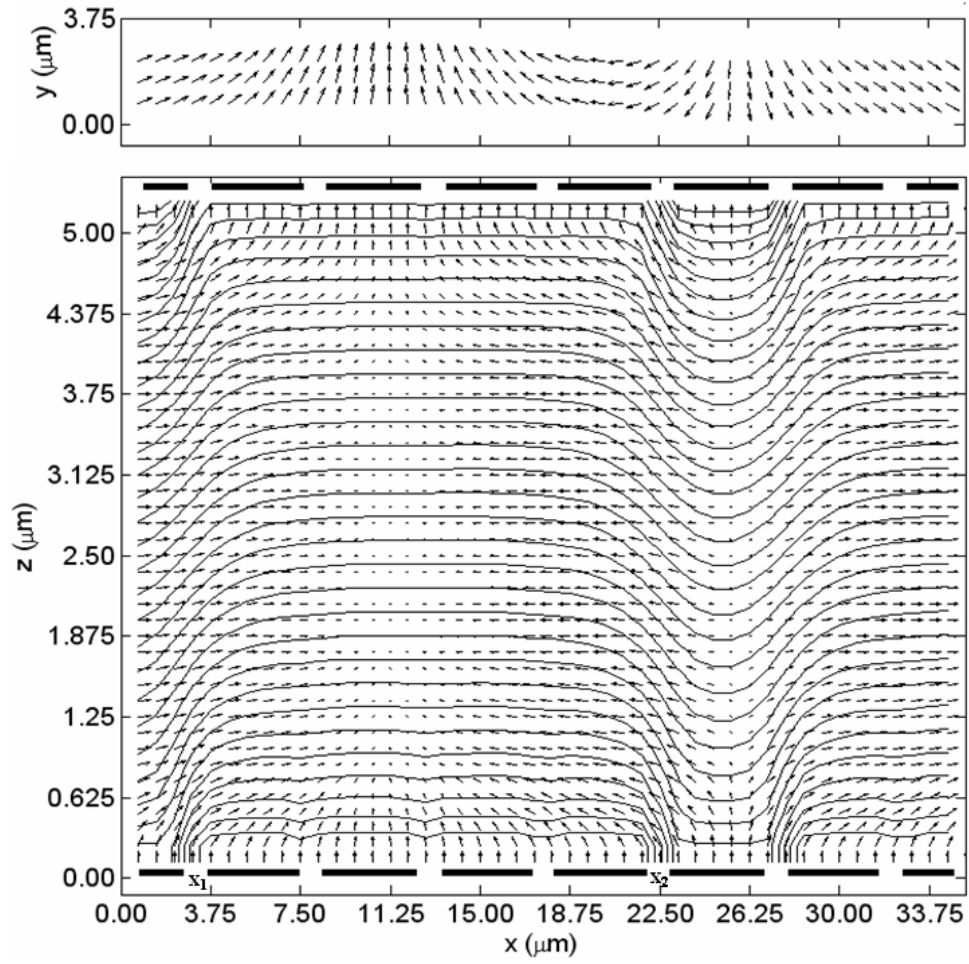


Fig. 3.10 Tuning of LCPGs with 13.5 μm period

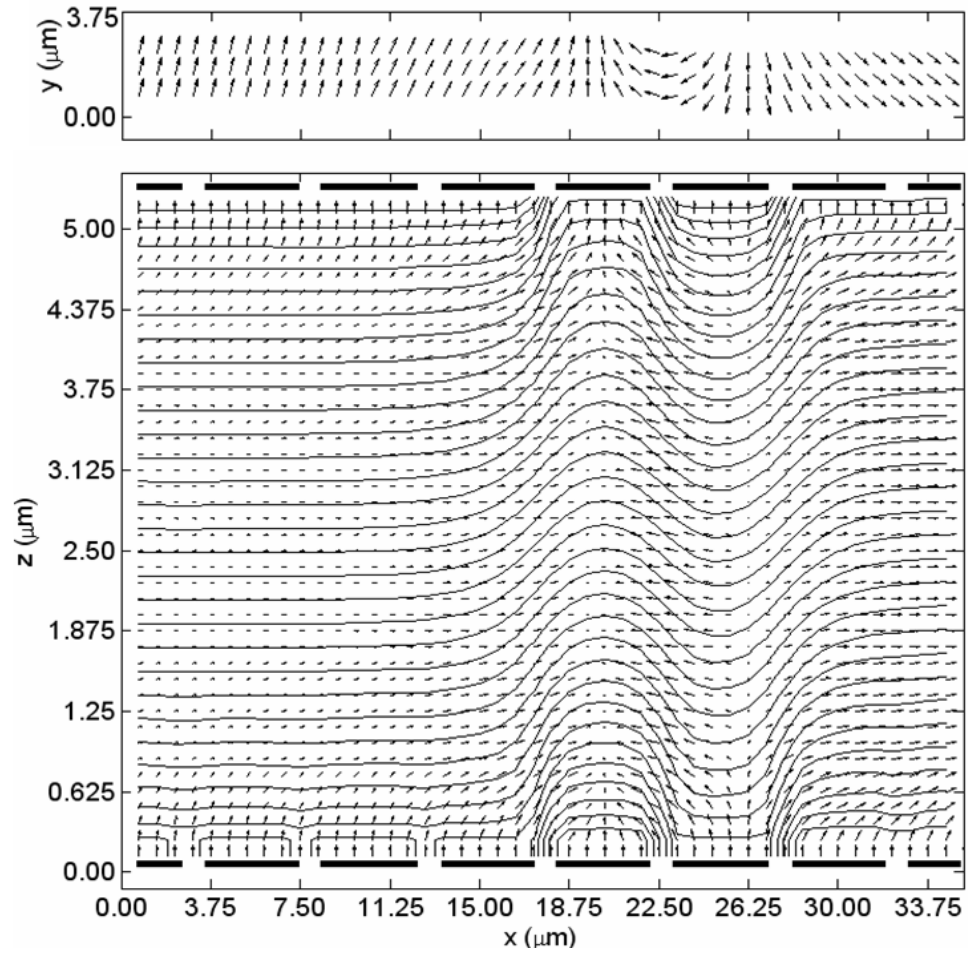


Fig. 3.11 Tuning of LCPGs with 7 μm period

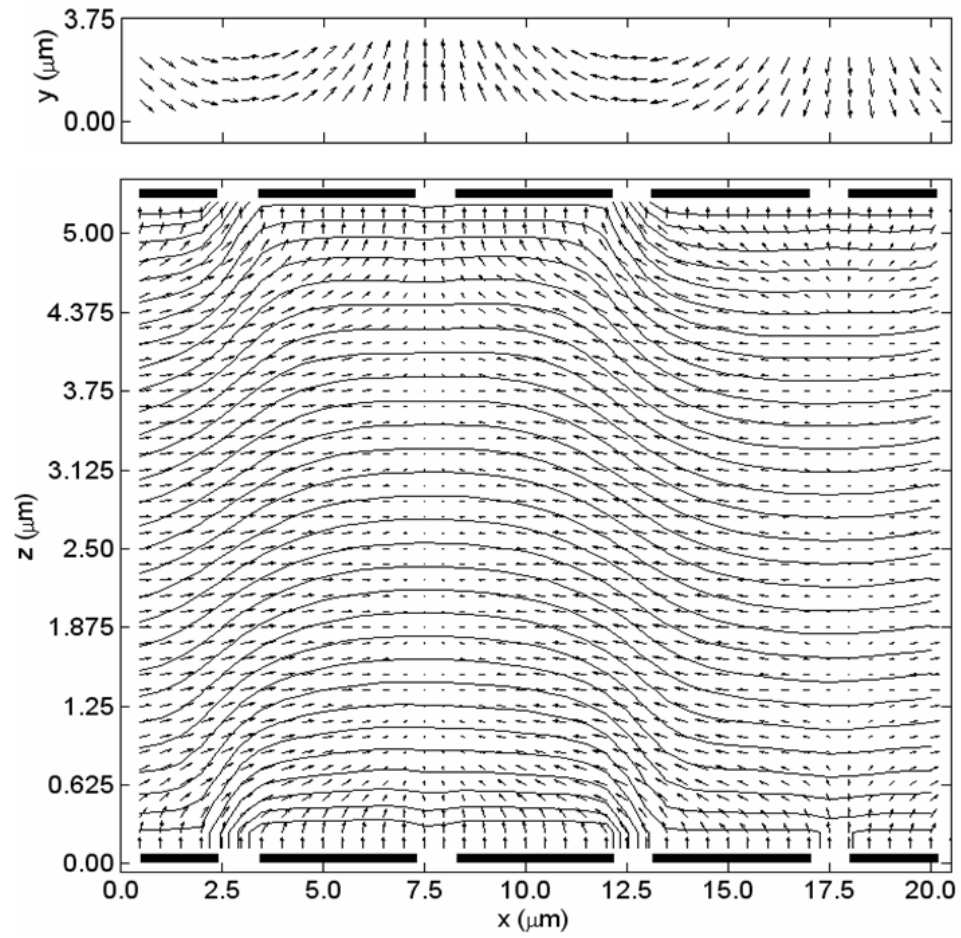


Fig. 3.12 A repeated LCPGs spiral of grating with $10.25\mu\text{m}$ period

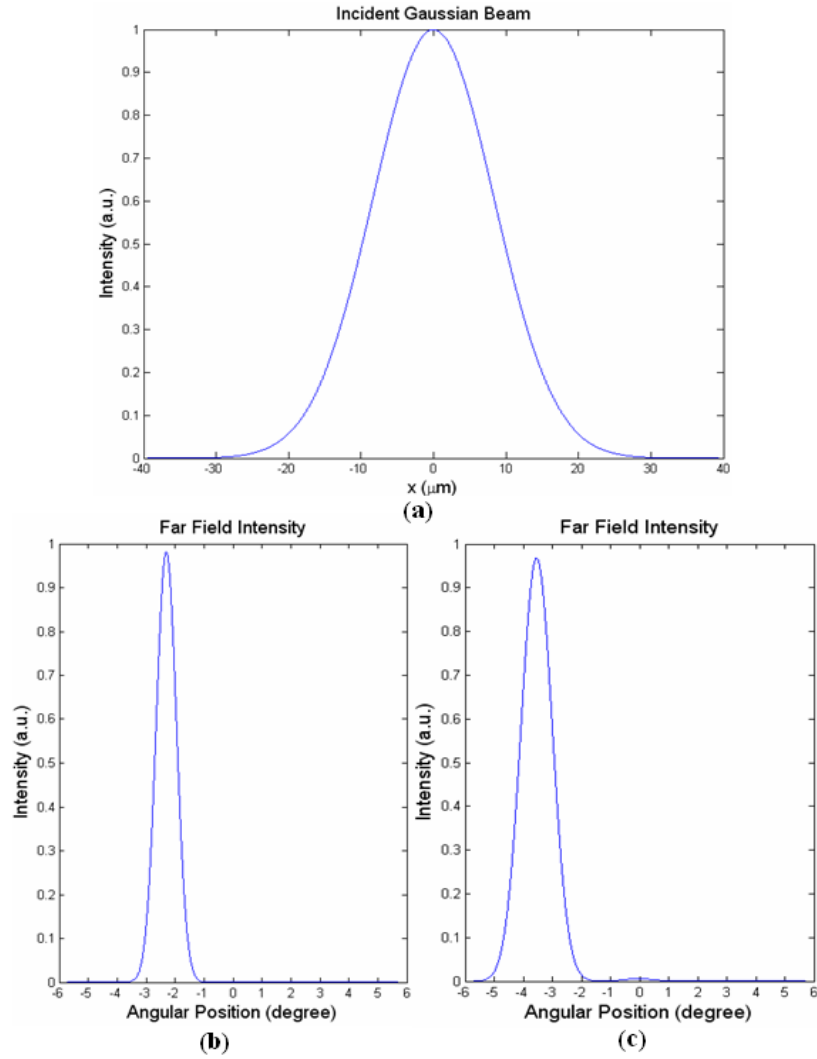


Fig. 3.13 Scalar Theory Calculation Results of tunable LCPGs

(a): Incident Gaussian Beam; (b): Far Field Intensity vs. Angular Position

for case in Fig.5, which is $15.75\mu\text{m}$ period; (c): Far Field Intensity vs.

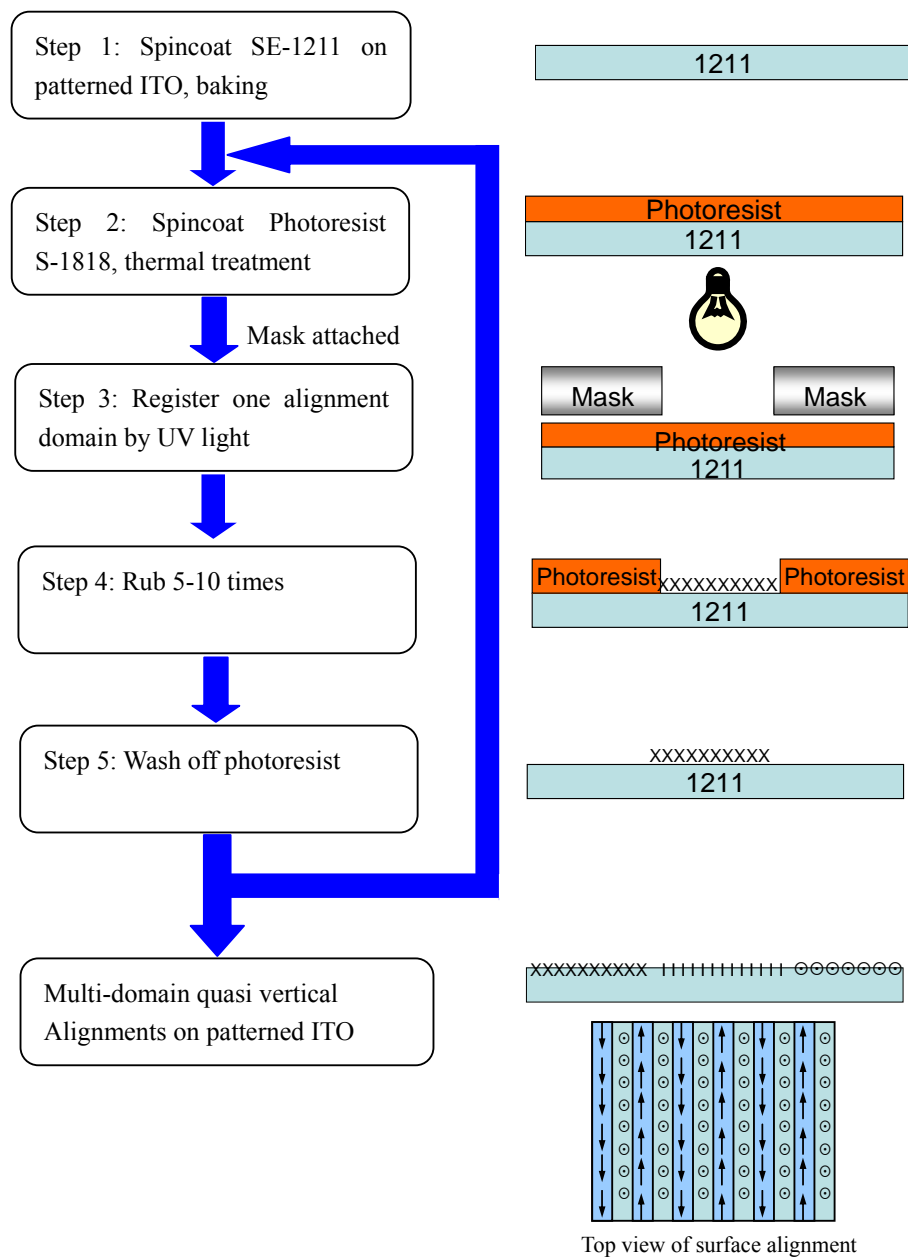


Fig. 3.14 Procedure of three domain quasi-vertical surface alignment

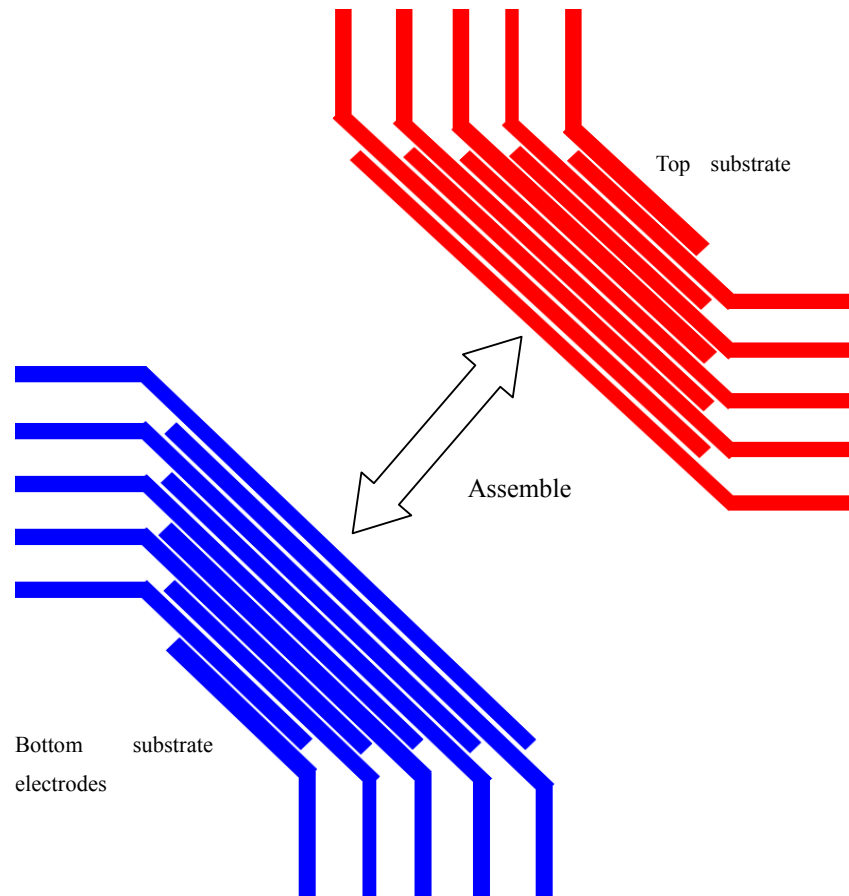


Fig. 3.15 Patterned electrodes in bottom and top substrate of LCPGs

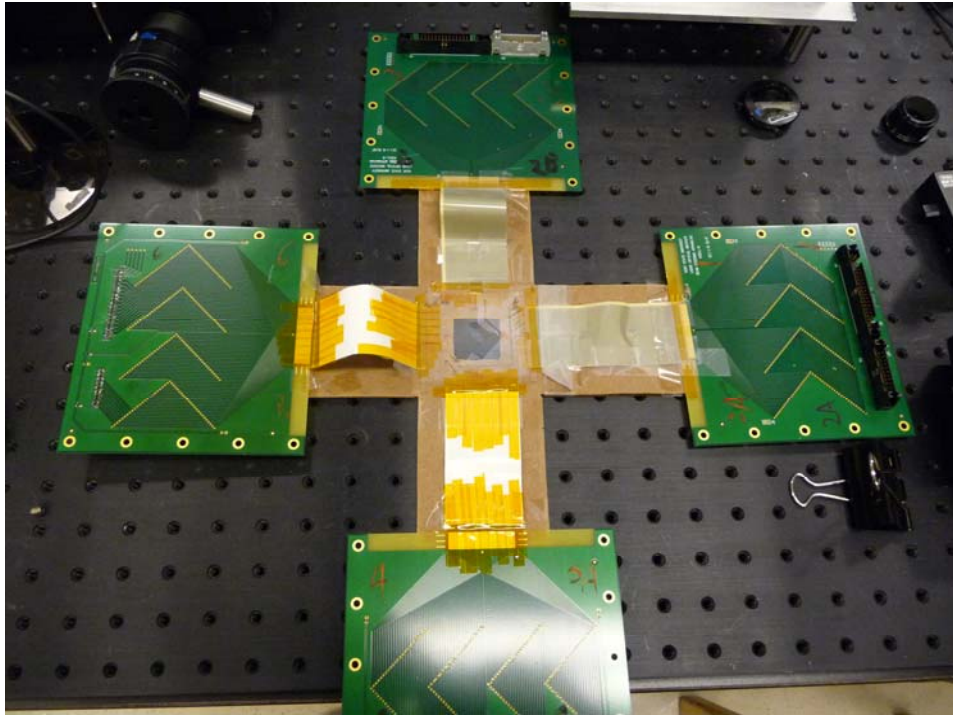


Fig. 3.16 Photo of LCPGs device with four interface board

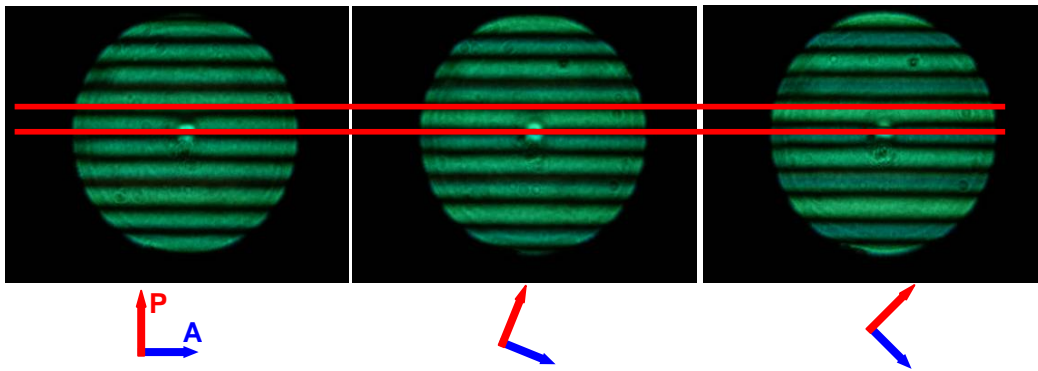


Fig. 3.17 Polarization Microscopy of LCPGs device

- (a) rotate polarizers with 0 degree; (b) rotate polarizers with 22.5 degree; (c)
rotate polarizers with 45 degree

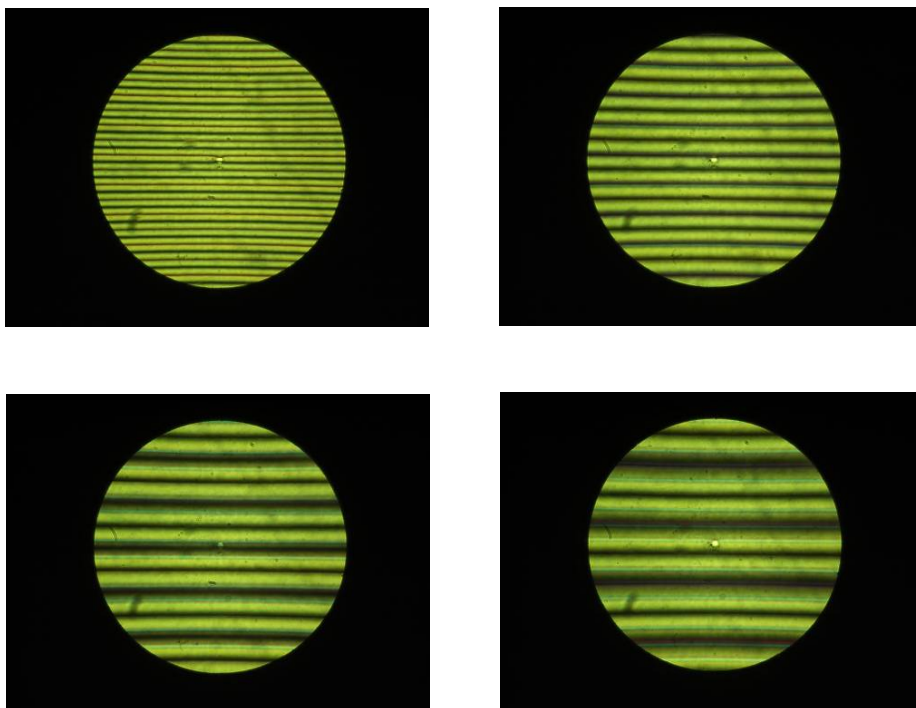


Fig. 3.18 Period tuning of LCPGs device in Polarized microscopy

(a) Initial period of $23\mu\text{m}$; (b) tuned period of $46\mu\text{m}$; (c) tuned period of $69\mu\text{m}$; (d) tuned period of $92\mu\text{m}$

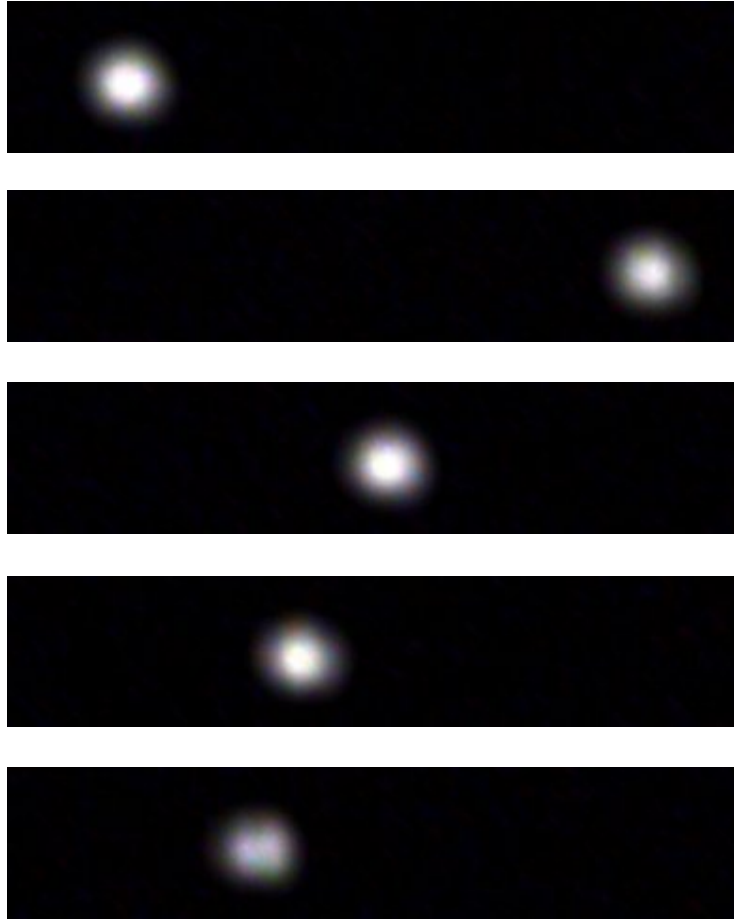


Fig. 3.19 Deflection beam in different period of Tunable LCPGs device

- (a) 0 degree without voltage applied; (b) 3.4 degree deflection with 23 μm period
(c) 1.7 degree deflection with 46 μm period; (d) 1.1 degree deflection with 69 μm period;
(e) 0.85 degree deflection with 92 μm period

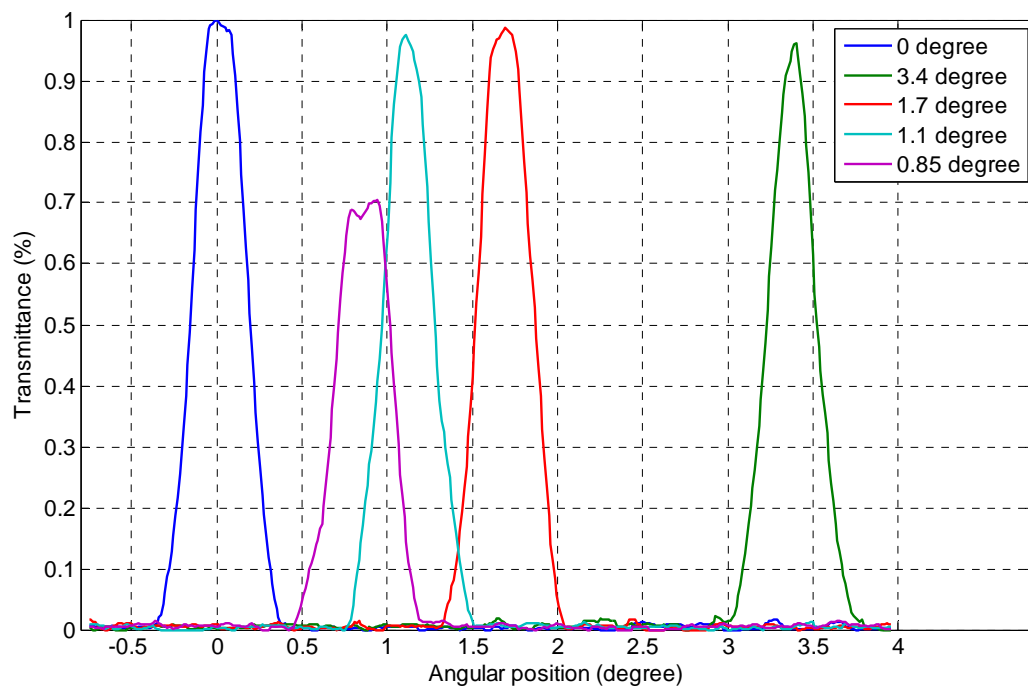


Fig. 3.20 Intensity profile of deflection beam for different period

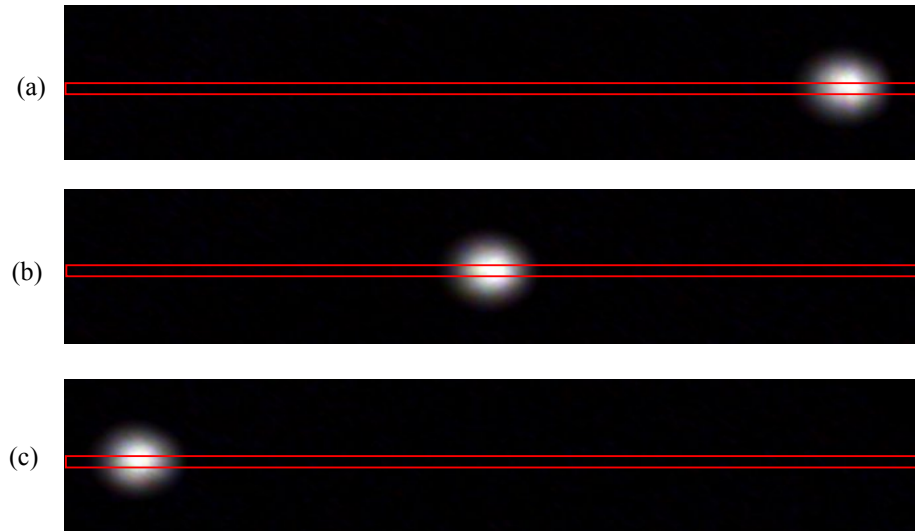


Fig. 3.21 Polarized microscopy of three-state switching of LCPGs

(a) “-” state; (b) “0” state; (c) “+” state

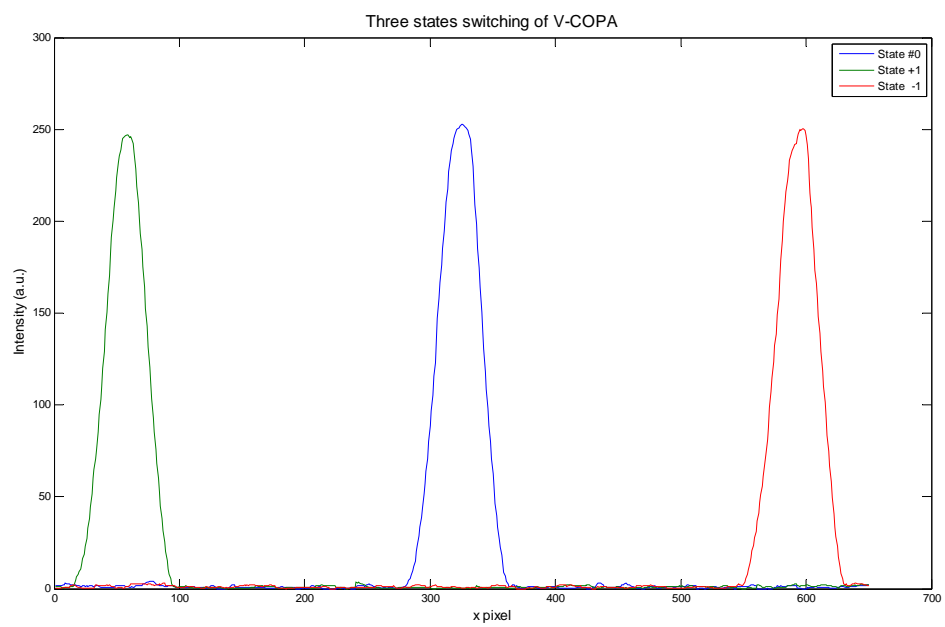


Fig. 3.22 Intensity profile along x of three-state switching of LCPGs

Chapter 4

Dynamics modeling of dual frequency LCPGs

4.1 Introduction

In Chapter 3, we have demonstrated the basic concepts and mechanisms of tunable liquid crystal polarization gratings (LCPGs) by the modeling and experimental results. The excellent steering efficiency and continuous tunable steering angles have been implemented by the fabricated LCPGs device filled with a negative dielectric anisotropy liquid crystal material.

However, one critical limitation of the LCPGs is the slow tuning speed. From a series of snapshots of the polarized optical microscopy of the tunable LCPGs (Fig. [4.1](#)), we explicitly show the detailed transforming procedures with three steps. The greenish snapshots at the beginning and the end of each step are the equilibrium director configurations applied with 10V on bottom and 0V on top, and no offset is applied, while the red snapshots are inter-medium state, for example in step 1 with 8, 5, 8, 5, 8, 5V...on bottom, and 3, 0, 3, 0, 3, 0V...on top. Appropriate high voltage offset will benefit the response time. Step 1 is the tuning procedure from the initial period (23 μm) to the expanded period (46 μm). The period varies from 46 μm to 69 μm in step 2, and from 69 μm to 92 μm in step 3. The arrow along x axis represents the response time scale of the snapshots. “Jumping” method is employed here to realize the tuning process in three steps. The response time is approximately about 640 ms in step 1, around 1.6 seconds in step2, and it will increase up to 3-5 seconds in the case of step 3. The relatively slow tuning speed will seriously limit the practicality of the tunable LCPGs device, since the fast and agile angular switching or tuning is preferred or

required in many beam steering applications.

To improve the response time, we first study the general concept of the tuning process of our LCPGs device. Then we will introduce three major tuning approaches, which are “walking” method, “jumping” method and “resetting” method. Based on the dynamics modeling of these approaches, we will propose a dual frequency tunable LCPG (V-COPA) device that is characterized with the fast tuning capability.

4.2 General concepts of driving scheme

To illustrate the tuning algorithm, as a starting point, we can first consider the method of single frequency LCPGs device discussed in Chapter 3. The voltage offsets are translated to the new location A' in Fig. 3.5. Before the voltage adjustment, the orientation of LC director in region A' was towards the x axis with very small azimuthal angle β . The effect of the fringe field from the voltage offset will reorient the LC director in region A' along the x axis with the new β' equal to 0° . As we know, the issue with this approach is that the response time is longer than the desired for some applications.

To improve the response speed of the period tuning, it is helpful to consider what the driving force of the period tuning is. The general strategy of period tuning is to translate several specific orientation regions, such as the regions A , region B and region C in Fig. 4.2, (along +x or -x axis) by translating the locations of the external torque that hold the director along the x or y axis in the figure. We denote the region A , where the directors orient towards +x axis with azimuthal angle β equal to 0° , as the left boundary of one full period. Similarly, the right boundary of the period is region C where the directors orient towards -x axis with β equal to 180° . Region B , where the

director is along +y axis with β equal to 90° , is denoted as the center of the period. We decompose the overall procedure which the period changes from a longer distance to a shorter one step by step as shown in Fig. 4.2. That is the typical “walking” method that we will introduce the details in section 4.4.1.

Three assumptions are set to explain the general concept of driving scheme. First, assuming the initial period of spiral director configuration has already been formed in step 1 of Fig. 4.2, we are able to vary the period based on the initial spiral configuration. Second, the surface alignment will not prohibit the translation of the spiral configuration along x axis, especially the center and boundaries regions. In our case, the quasi-vertical alignment is simply a trigger to initialize the in-plane spiral structure, and the homeotropical director configuration (along z axis) near the surface can gradually reorient towards any direction in the x-y plane of the bulk in principal. Third, we have a means that can reorient the directors in region A' (a region near the left boundary A) towards the x axis, and also have a means to reorient the directors in region B' (a region near center B) towards the y axis. By this approach, the orientation of the left boundary ($\beta = 0^\circ$) in the left shadow area and the orientation of the center in the center shadow ($\beta = 90^\circ$) will transit to a new location towards +x direction, while the orientation of the right boundary ($\beta = 180^\circ$) will keep as the initial location. As a consequence, the total length of the period will become shorter. Or we may translate the left boundary and center towards -x direction. In this case, the total length of period will be extended. Note that the external forces only focus on three specific domains (left or right boundary, and center), since the directors in all the other regions can be correctly oriented by the liquid crystal elasticity itself if the period is not too large. The concept can be analogous with holding one end of a spring, while pushing or pulling another end. All the other segments of the

spring will be adaptive to the external force automatically unless the stiffness condition is destroyed.

Considering the single frequency LCPG device described in Chapter 3, we can only have a torque to cause the director to align in one direction. However, by using a liquid crystal material whose dielectric anisotropy can change sign, we can consider to have torques to cause the director to align along the x or y axes. Liquid crystal material called “two frequency” materials have this property.

A two frequency liquid crystal is a material whose dielectric anisotropy is negative at high frequencies and positive at low frequencies.⁴¹ These materials will align along an electric field direction with a low frequency applied voltage (denoted as the positive mode). However when a high frequency voltage is applied, the LC will orient perpendicular to the field direction (denoted as the negative mode). The two modes can coexist if both high frequency and low frequency field are applied to the same region at the same time.

To numerical model the director configuration of dual frequency liquid crystal material, and study the dynamics characteristic of such device, we will first briefly introduce the basic concepts of the numerical modeling of dual frequency LCPGs.

4.3 Numerical dynamics modeling of dual frequency LC

4.3.1 Numerical modeling of dual frequency LC

The approach to simulate dual frequency LC device is to create two set of numerical arrays of voltage in the simulation. With low frequency voltage, a positive dielectric anisotropy is used to calculate the contribution to the electric free energy of the system, while a high frequency applied

voltage, a negative dielectric anisotropy will be employed in the contribution to the electric free energy. Both of the voltage profiles will contribute to the total free energy which led to the equilibrium state of the LC director configuration.

When we calculate the derivative of the electric free energy, an additional term should be included as Eq. 4.1:

$$\frac{df_E}{dn_i} = \frac{1}{2} \varepsilon_0 \cdot \left[\frac{dV_+}{di} \cdot \sum_j \left(\frac{1}{2} \cdot \frac{dV_+}{dj} \cdot n_j \right) \cdot \Delta \varepsilon_+ + \frac{dV_-}{di} \cdot \sum_j \left(\frac{1}{2} \cdot \frac{dV_-}{dj} \cdot n_j \right) \cdot \Delta \varepsilon_- \right] \quad (4.1)$$

$i, j = x, y, z$

Where V_+ , and V_- are the voltage for the positive and the negative mode separately.

The two sets of voltage profile are relaxed and calculated separately. Each voltage profile is then used to obtain the separate contributions to Eq. 4.1. The director configuration will be relaxed until the system reaches the equilibrium state.

4.3.2 Dynamic modeling

To study the dynamics of liquid crystal director relaxation, a simultaneous displacement approach is generally used. With simultaneous displacement, the modeling will calculate the director orientation on the entire lattice, and then update the entire director configuration at the same time.

We discretize the time of the LC director relaxation into n steps with defined time period τ (such as 25 ms) for each step. The voltage applied on the system will be updated immediately once a new step starts. For every step, the stopping condition is either the system reaching to the equilibrium state, or the accumulated modeling time for that step greater than τ . With the

dynamics LC3D tools that we develop, we are able to simulate, investigate and improve the performance of tuning speed of the LCPGs device.

To validate the response time calculated from the dynamics modeling, we compare the dynamics modeling results of the tuning by jumping method with the experiment tuning results. It turns out that the modeling results are reliable since it takes approximately 1/5 times of the experimental process with exactly the same configurations, setup and procedures.

4.4 Tuning methods of LCPGs

From the perspective of driving scheme of the applied voltage, there are three approaches to tune the LCPGs device, which are “walking” method, “jumping” method, and “resetting” method. Walking method is a continuous tuning approach to vary the period by a series of gradual changed voltage steps. This method is reliable and robust to have defect free tuning process. The disadvantages are the relatively slow speed compared with the other two methods, and complicated driving scheme with a series of tuning steps. “Jumping” method and “resetting” method are two discrete tuning approaches with voltage profile changed abruptly. Compared with the walking method, they are possibly faster to accomplish the tuning steps, and very simple algorithm to realize. Nevertheless, they also come with the high risk of generating unexpected defects or disclinations in the system that will lower the final steering efficiency.

4.4.1 “Walking” method

As we described in Fig. [4.2](#), “walking” method is a process that the pitches of the period of LCPG are continuously changed by modifying the voltage profile gradually. With this approach,

we are able to expand or shrink the pitch of the LCPGs with low risk of forming defects or disclinations. Table [4.1](#) shows the typical scheme of driving voltage of “walking” method. As a consequence, the director configuration in Fig.[4.3](#) will reorient and modulate the period from the initial large pitch to a small one.

To illustrate the details of continuous tuning method, we can first investigate the initialization of voltage pattern of single frequency LCPGs in Chapter 3 that provides a voltage “offset” between two areas of the device. At the location of the offset, the director tends to tilt to be perpendicular to the electrodes as discussed in Chapter 3. This concept works well for initializing the desired spiral pattern, but once the pattern is formed the effect of the offset is not ideal for holding or changing the spiral pitch, in other words, it can not modulate the period within a short response time. With the director being held in the plane of the cell (the $x - y$ plane) it is more likely that the lowest energy director configuration will be with for it to lie parallel to the electrodes at the offset region. We find that applying an “offset”, to a single electrode width can effectively trap the director to be parallel to the electrode direction as shown in Fig. [4.4](#).

It seems to be conflict with the initialization process that the offset will trap the boundary region A or C, instead of the center region B in Fig. [4.2](#). Actually both configurations (boundaries or centers) are possible to trap for the applied fringe field with the offset, since they are both perpendicular to the fringe field for a negative dielectric anisotropy LC material. When the initial director configuration is vertical, and the offset is applied to the boundary region A or C, the director in A or C near the surface will prefer to align along the equi-potential field line (Fig. [3.9](#), Chapter 3), which is in $x-z$ plane and towards x axis. To be consistent with the director near the surface and lower the free energy, the LC directors in the bulk of the fringe field region will

thereafter reorient towards the x axis and form the boundary regions. It is a different story when we apply an offset voltage on the existing LC director that have been approximately aligned towards y axis (region B' near the center). The director will prefer to reorient towards y axis and form a new center region to minimize the free energy of the system. It turns out that this process is much more effective and faster than the other one.

An added advantage of this method of using the negative dielectric anisotropy of the LC material to fix region B in Fig. 4.2 is that when “two frequency” liquid crystal material is used, we can also apply a voltage that couples with the positive mode of the material to trap the director perpendicular to the electrode direction (regions A and C in Fig. 4.2) as shown in Fig. 4.5.

An issue with continuous tuning is the ability to absorb or nucleate spirals. This can be accomplished by having regions in the aperture that have a vertically aligned director field (without any voltage applied) that will absorb spirals, and that can be used to nucleate spirals that are shifted into the active area. Details of this approach will be shown in the calculation section 4.4.

4.4.2 “Jumping” method

We consider two discrete tuning approaches: “jumping method” and “resetting method”. A single frequency LCPGs or a two frequency LCPGs device in the negative mode can be tuned with discrete periods. As for jumping method, we switch the voltage profile abruptly from one period to another period without any intermediate steps. The typical voltage scheme is shown in Table 4.2. The relevant director configurations of each step are illustrated in Fig. 4.6. From the program point of view, it is very simple and easy to setup the driving scheme to control the

“jumping”. In the section 3.5, all the tuning results are implemented by the “Jumping” method. Nevertheless, as we have shown in Fig. 4.1, especially in step 3, since the applied voltage is abruptly changed without any buffering procedures, it is very easy to form any topology difference that come with wrong rotation sense or disclinations. The external torque of the fringe field will try to minimize or eliminate these regions, but it turns out to take very long time to reach the final equilibrium state with acceptable polarization gratings. This process is up to several seconds or even longer. That will severely limit the performance of tuning speed of our device. We have expected the simple “jumping” method to be characterized with faster tuning speed, but unfortunately the above issue would rather lead to the relatively long response time, especially in the case of switching between the longer period.

4.4.3 “Resetting” method

The “resetting method” resets the voltage profile to 0V for all electrodes every time once we want to switch to a different period, and then apply relevant voltage schemes to form a new period.

The resetting method will be described through an example. Consider the surface alignment will designed as shown in Fig. 4.7 with the different domain alternating over every electrode. To initialize the in-plane spiral of grating, similar to the process in Chapter 3, we apply the voltage profile: 10, 12, 10, 12, 10, 12, 10, 12V on the electrodes of bottom substrate; 0, 2, 0, 2, 0, 2, 0, 2V on the top.

To switch the deflection angles between different periods, as shown in the Table 4.3, firstly we reset the voltages on all electrodes to 0V. This step recovers the whole LC director back to the

initial homeotropical state (actually a further speed improvement could be obtained by applying a low frequency (positive mode) voltage between the top and bottom electrodes). Thereafter we are able to apply a different voltage scheme to form another period. For instance, after reset, we apply a field with low voltages (negative mode) on several specific electrodes: 0, 0, 2, 0, 0, 2, 0, 0V on the bottom substrate, with zero voltage is applied on the top. With this “pre-initialization” step, the directors over electrode #3, and also the directors near the electrode #3, i.e., electrode #2 and electrode #4, will all have slight tendencies to tilt towards the $-y$ direction, even though the quasi-vertical alignment over electrode #2 and electrode #4 are towards $+y$ direction. With this formed orientation tendency by the pre-initialization voltage applied on electrode #3 and #6, in the subsequent initialization step, we will be able to form a new period by applying the following voltages (negative mode): 10, 12, 12, 12, 10, 10, 10, 12V on the electrodes of bottom substrate; 0, 2, 2, 2, 0, 0, 0, 2V on the top. The opposite direction of azimuthal angle from the quasi-vertical alignment will not affect the formation of the period since the orientation preferences in these domains have already been determined. With the above procedures, we are able to form the “odd” periods with such length as 1, 3, and 5 etc pixel spacing. By modifying the voltage profile the sense of the helix can be changed so the number of steering angles is twice the number of possible periods.

The resetting method has the fast speed switching capability because it does not involve any disclination motion associated with a topological change. However, the deflection angles by resetting method are limited to several specific states.

The V-COPA device tuning with resetting method is promising to make a digital beam deflector device.

In order to validate the concept of “resetting method” for digital beam deflector, similar procedures (three steps: reset, pre-initialization, and initialization (of final state)) were modeled in Fig. [4.8\(step 0-step 3\)](#). The device parameters are similar to the setup in Chapter 3.4 of single frequency LCPGs device. The voltage profiles applied for each step were listed in Table. [4.3](#). Since no intermediate steps as the continuous tuning method are required for this approach and also no equilibrium states are necessary for step 0 and step 2, the switching speed can be improved to the range of 50 to 100ms.

The modeling results are demonstrated by the polarized microscopy images of the director configuration in x-y plane of the four steps: initialization (of the first period), resetting, pre-initialization, and initialization (of the 2nd period) are shown in Fig. [4.9\(step 0-step 3\)](#) respectively.

It is interesting to study what is the limit of the shortest period. Based on the similar initialization process, we investigate a V-COPA device with 3 μm thickness and three electrodes as a surface alignment group, with the sizes of electrodes and gaps are equal to 1 μm and 0.5 μm respectively. We modeled the initialization of the spiral director configuration in this device and found it formed correctly as shown in Fig. [4.10](#). Note that a full 9 micron period of in-plane spiral director configuration will result in two full waves of phase difference, since the output phase gradient is two times of the gradient of director rotation. Therefore we get a phase grating with period as short as 4.5 μm . The deflection angle for a 4.5 μm period is 19.47 degree at the wavelength of 1.5 μm .

4.5 Dynamics modeling of dual frequency LCPGs

4.5.1 Continuous tuning of dual frequency LCPGs

In Chapter 3, we have introduced the details of modeling results of tuning the single frequency LCPGs device. Since the single frequency tuning is actually a subset of two frequencies LCPGs, we will focus on the continuous tuning of two frequency LC material in this section.

Considering a cell with a 3 μm gap filled with dual frequency liquid crystal *MLC-2048*, which has a positive dielectric anisotropy $\Delta\epsilon$ of +3.22 at 1 kHz and a negative dielectric anisotropy of -3.08 at 50 kHz. The cross-over frequency for *MLC-2048* is slightly exceeds 10 kHz. The electrode stripe's width (along x axis) is 1 μm , and the gap between two electrodes is 0.5 μm . There are totally 25 full electrodes in the simulation region as 37.5 μm . Note that the first electrode and the last one are modeled as two halves of the same electrode. Therefore, totally 26 electrodes appear in the simulation range. The surface alignment has three different domains. The alignment over electrode #1 has the azimuthal angle of 90° and polar angle of 88° , which is also the same alignment as the one over the last electrode. For the other 24 electrodes, denote every 6 electrodes as a group with the same surface alignment. For example, the alignment over electrodes #2 to #7, and #14 to #19, has the azimuthal angle of 270° and polar angle of 88° , while the alignment over electrode #8 to #13, and #20 to #25 has the azimuthal angle of 90° and 88° polar angle. With this alignment setup, we are able to form the initial in-plane spiral director configuration in Fig.4.11(a-b) with the applied voltage profile as: 12, 10, 10, 10, 10, 10, 10, 10, 12, 12, 12, 12, 12, 10, 10, 10, 10, 10, 10, 12, 12, 12, 12, 12, 12, 10V on the electrodes of bottom substrate; 2, 0, 0, 0, 0, 0, 0, 2, 2, 2, 2, 12, 12, 10, 10, 10, 10, 10, 10, 12, 12, 12, 12, 12, 12, 10V on the top. Two full periods of in-plane spiral have been formed.

To tune the period of dual frequency V-COPA device with fast speed, we use two sets of

voltage profile at the same time.

One is in the positive mode to translate the boundaries to the left or right direction. The driving scheme of the low frequency voltage applied on bottom substrate is shown in Table. 4.4, which is also the same value for the electrodes on the top substrate. The voltage profile of each step will last for a user defined time period, such as 50, 25, 15 or 10ms, etc. The liquid crystal directors are only allowed to relax within this time period. And then the voltage profile will be updated in the next step as shown in the table.

Another is in the negative mode to shift the center to the left or right direction. The relevant driving scheme on top substrate is shown in Table 4.5. As for the voltages of bottom substrate, all the relevant voltages are added with an additional 80V compared with the voltages on top substrate.

Both the low frequency voltage profile and the high frequency one are updated with the same speed rate. If the boundaries and centers are able to follow the update rate of the applied voltage, these specific regions will transit with an equivalent translation speed. Then the user defined time period for updating voltage profiles can be regarded as a “good” response time for the device. From the modeling for the above setup, we find 10 ms is the minimum time period that is “good” for the device. The in-plane director configurations in the middle plane of the cell (in x-y plane) are listed in Fig. 4.12(a-f) from step 1 to step 6. The odd shadowed regions (1st, 3rd, etc) are over the electrodes that provide the low frequency (positive mode) voltage, while the even shadow regions provide the high frequency (negative mode) offset voltage. The length of each period changes from the initial 18.75 μm to 13.75 μm after 6 steps.

The new period can be further suppressed to about 9.75 μm by another 6 steps, which is

almost half of the original one by the driving scheme listed in Table 4 and 5, with 10 ms time period between each step. When the average period is squeezed, it turns out the torque from the low frequency voltage will increase much faster than the high frequency one. To maintain the balance between them, we decrease the low frequency voltage offset to 5V. From Fig. [4.13](#), we note that during the period suppression process, in the fixed simulation region, some blank areas with no period will be formed as a result of period shrinking. The directors are oriented all the way towards $-x$ axis direction. To obtain as high diffraction efficiency as possible, we need continuous periods without any blank regions.

4.5.2 Nucleation of spirals

If we are able to nucleate some additional periods with correct rotation sense and same period width in these blank regions, we will keep the continuous in-spiral gratings. The basic concept to nucleate some addition periods is based on the similar procedures as the initialization. To save some tuning time, we began to relax these blank regions from step 4 to 6 in Table [4.6-4.7](#) which are the voltage profiles in the top substrate. The tuning results with relaxation of the blank regions are shown in Fig. [4.13\(a-f\)](#). Applying a high frequency voltage as 12, 10, 10, 10, 10, 10, 10, 12, 12, 12, 12, 12, 10, 10, 10, 12, 12, 12, 10, 10, 10, 12, 12, 12, 10V on the bottom, while apply 2, 0, 0, 0, 0, 0, 2, 2, 2, 2, 2, 2, 0, 0, 0, 2, 2, 2, 0, 0, 0, 2, 2, 2, 0V on the top. We will form another one full period of grating in the blank region along with the squeezed two full periods in Fig. [4.14](#).

While in Fig. [4.14](#) we show that the nucleation area is half of the total area of the device, but we visualize that the in an actual device the nucleation area is a small fraction of the total device area. In the case of a shrinking period, new spirals will be nucleated in the nucleation area and

shifted out into the active area, while in the case of a expanding period spirals will be shifted into the blank area which as no voltage applied so that the director alignment is vertical and the spirals are absorbed.

4.6 Summary

In chapter 3, the single frequency LCPGs device that we fabricated has shown high efficiency with variable steering angle as predicted by numerical modeling. But it also has the limitation of response time in the range of 650 ms and up to several seconds. A faster tuning beam steering device using “two frequency” liquid crystals has been proposed and modeled in this chapter. By tuning the dual frequency LCPGs device in both of negative mode and positive mode, we are able to translate the boundary and the center of the in-plane spiral of grating with a shorter response time. The total switching time is about 120 ms from initial period of $18.75\ \mu\text{m}$ to $9.75\ \mu\text{m}$ for a LCPGs device with $3\ \mu\text{m}$ thick and $1.5\ \mu\text{m}$ pixel spacing. In addition, the modeling of LCPGs device with period of $9\ \mu\text{m}$ shows a high efficiency digital beam deflector with large angle that is up to 19.47 degrees for $1.5\ \mu\text{m}$ light. We have also shown how spirals can be nucleated or absorbed in isolated regions of an aperture.

Other studies based on the LC3D modeling technology, such as the electro-optic liquid crystal lenses, was one extension of the work.

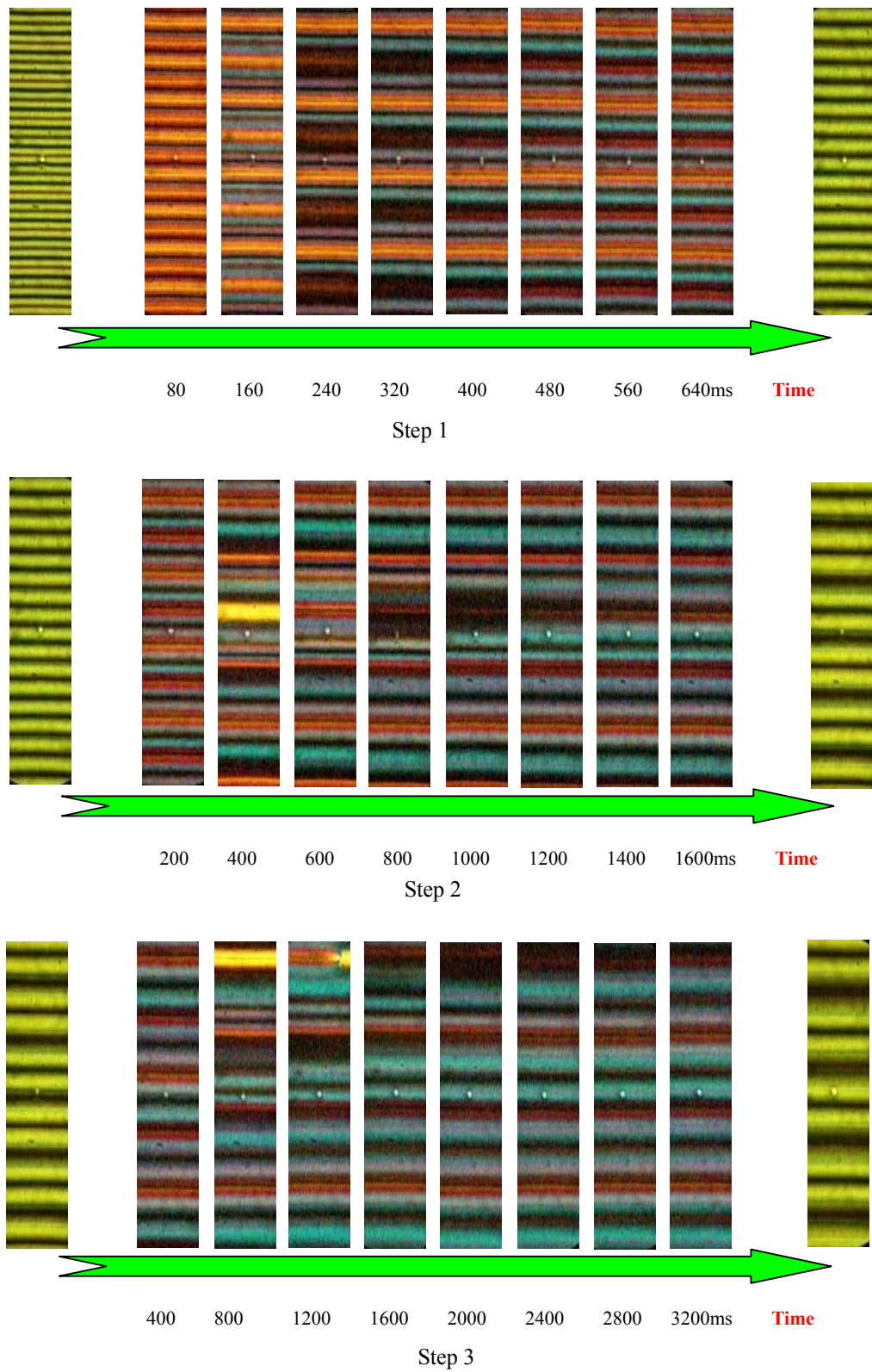


Fig. 4.1 POM Snapshots of tuning between different states of LCPGs

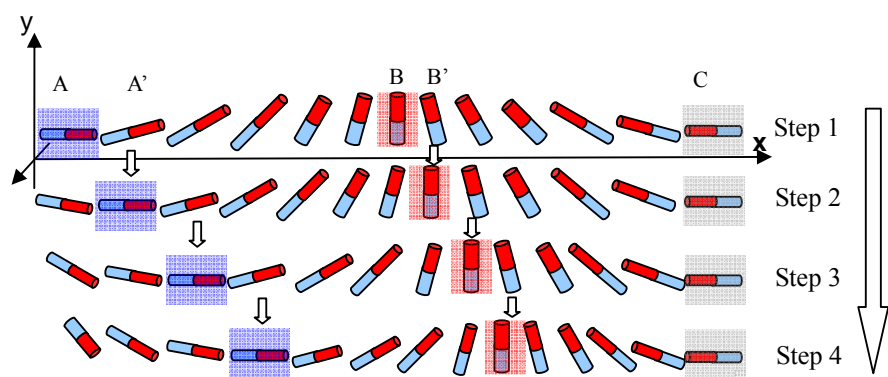


Fig. 4.2 Period tuning of dual frequency LCPGs by “walking” method

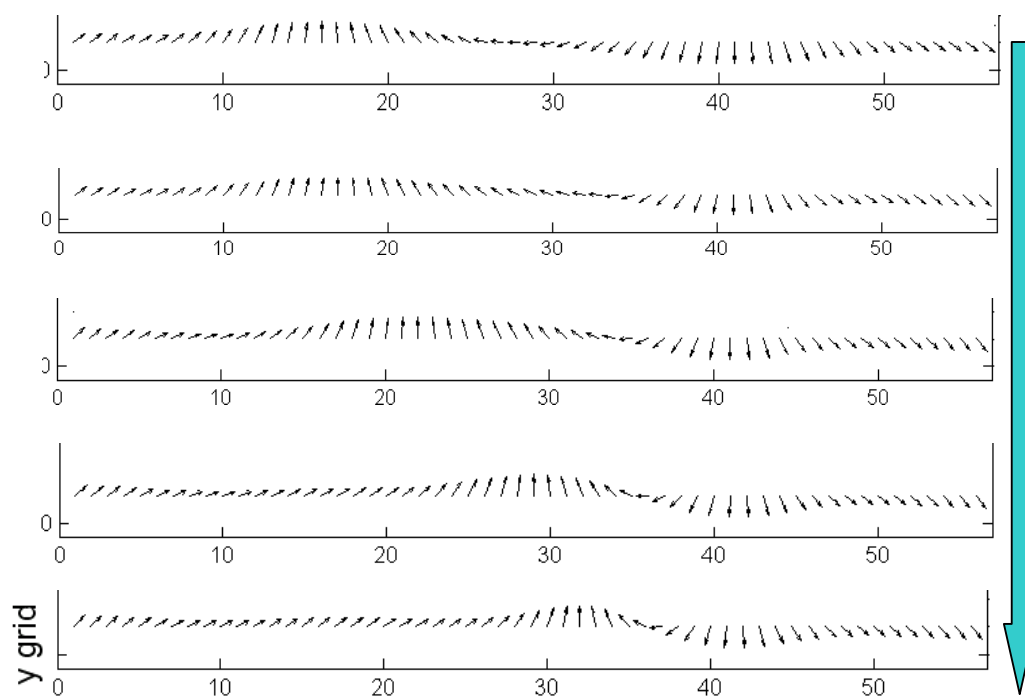


Fig. 4.3 Period tuning by “walking” method in x-y plane (middle of cell)

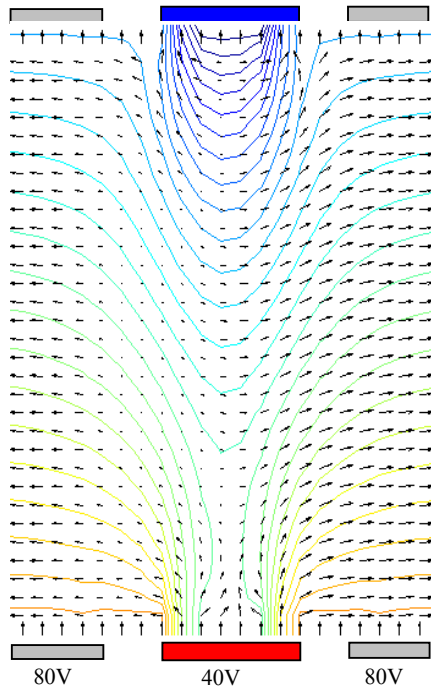


Fig. 4.4 Translation of the center in negative mode of dual frequency LCPGs

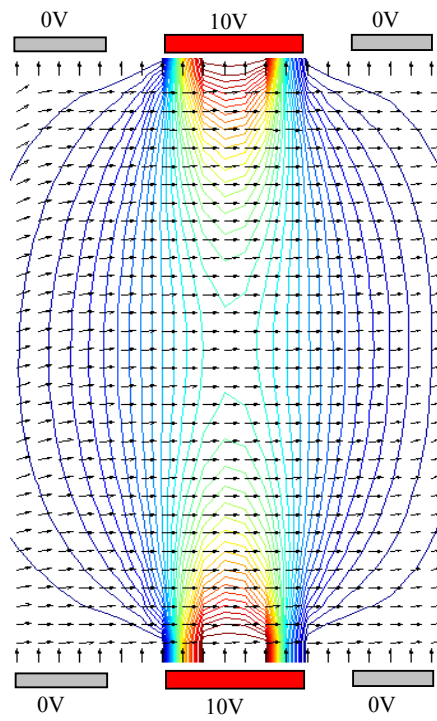


Fig. 4.5 Translation of the boundaries in positive mode of dual frequency LCPGs

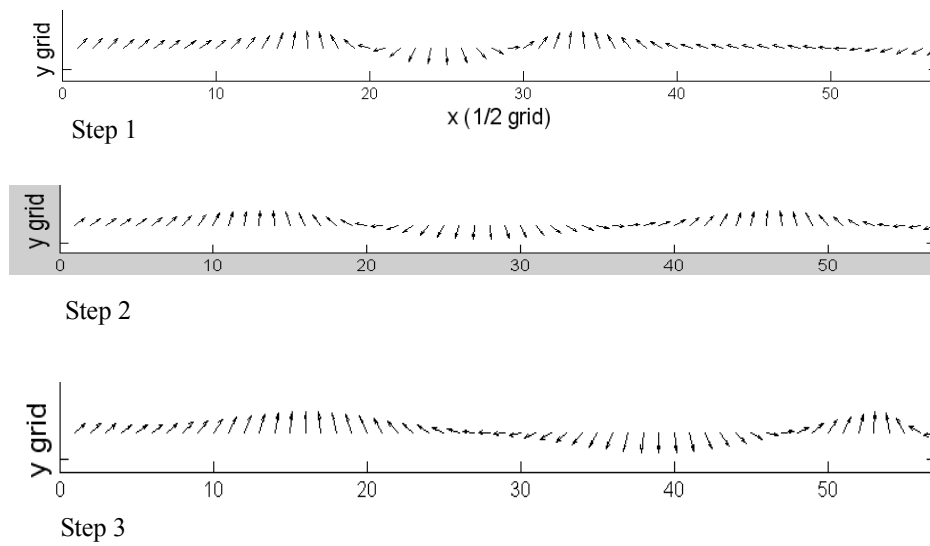


Fig. 4.6 Period tuning by “Jumping” method

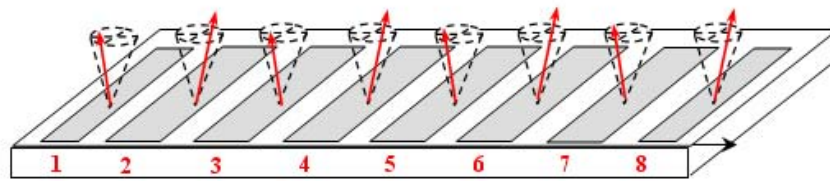


Fig. 4.7 Surface alignment of a large angle digital beam deflector

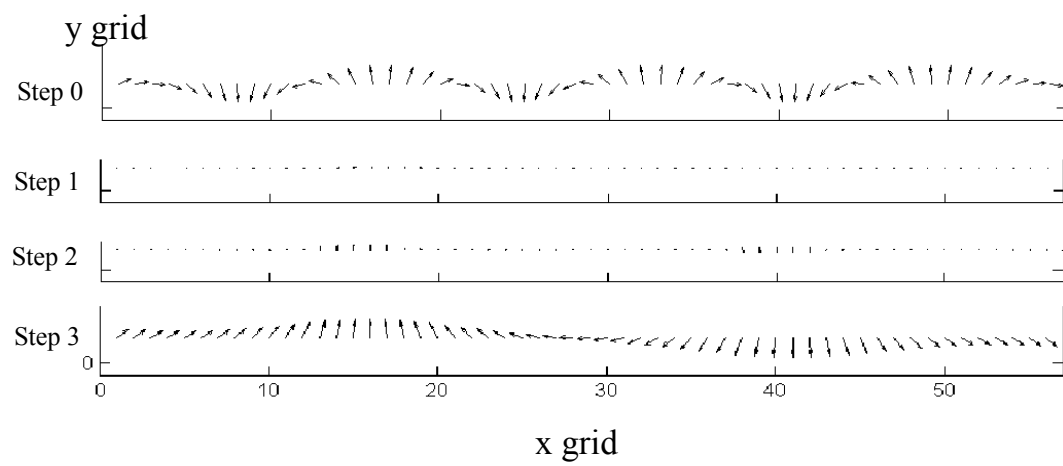


Fig. 4.8 Modeling of resetting method for a digital beam deflector

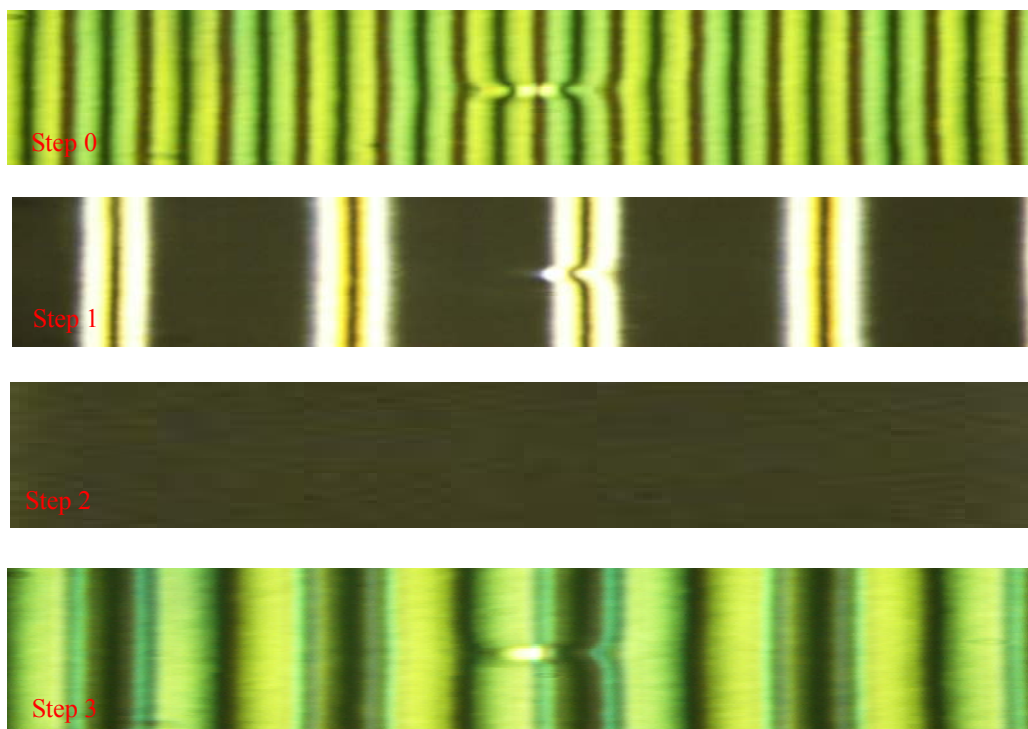


Fig. 4.9 Polarized optical microscopy of resetting method

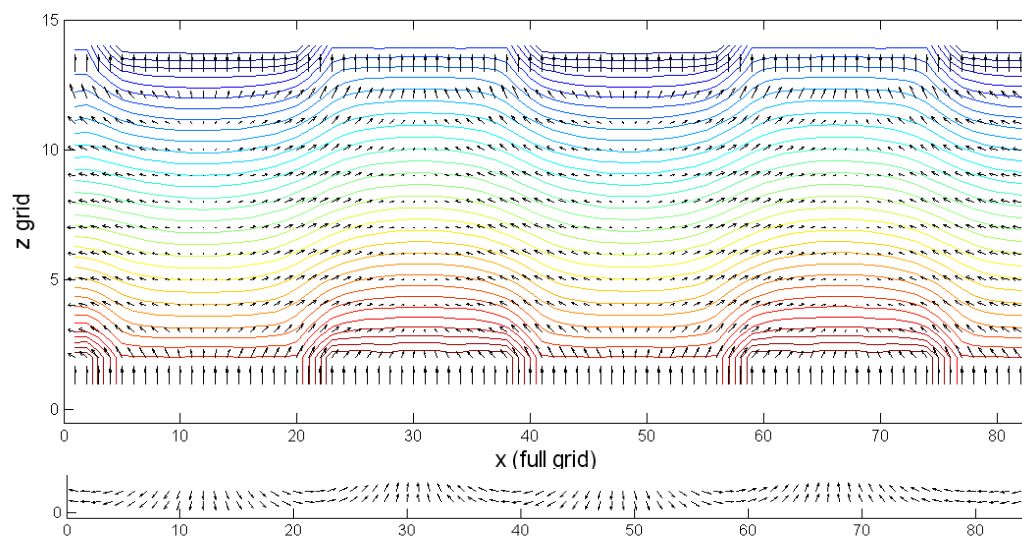


Fig. 4.10 A digital beam deflector with full period of $9\text{ }\mu\text{m}$

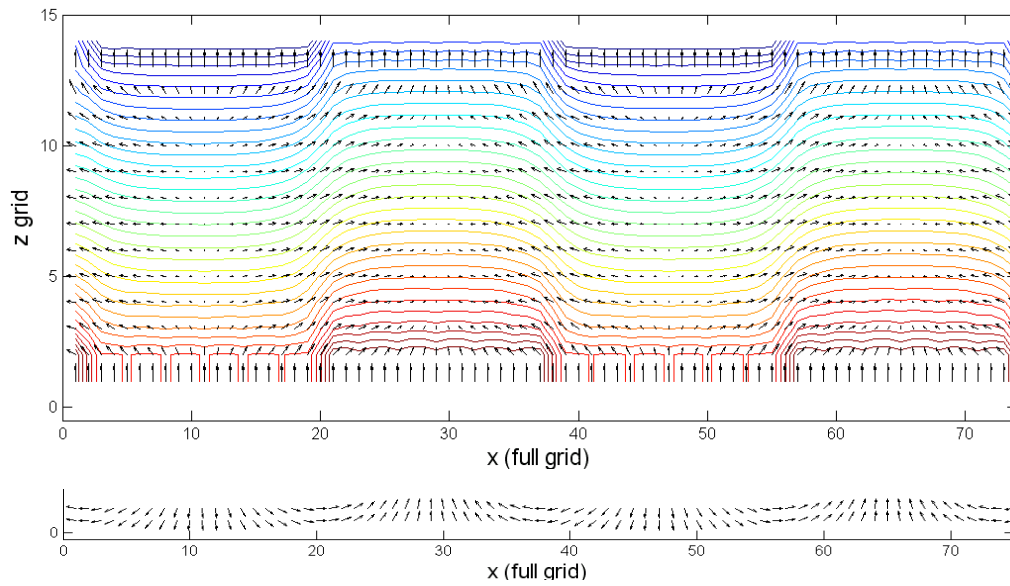


Fig. 4.11 Initialization of a dual frequency LCPGs in the negative mode

- (a) director configuration in x-z plane with equi-potential field line
- (b) director configuration in x-y plane

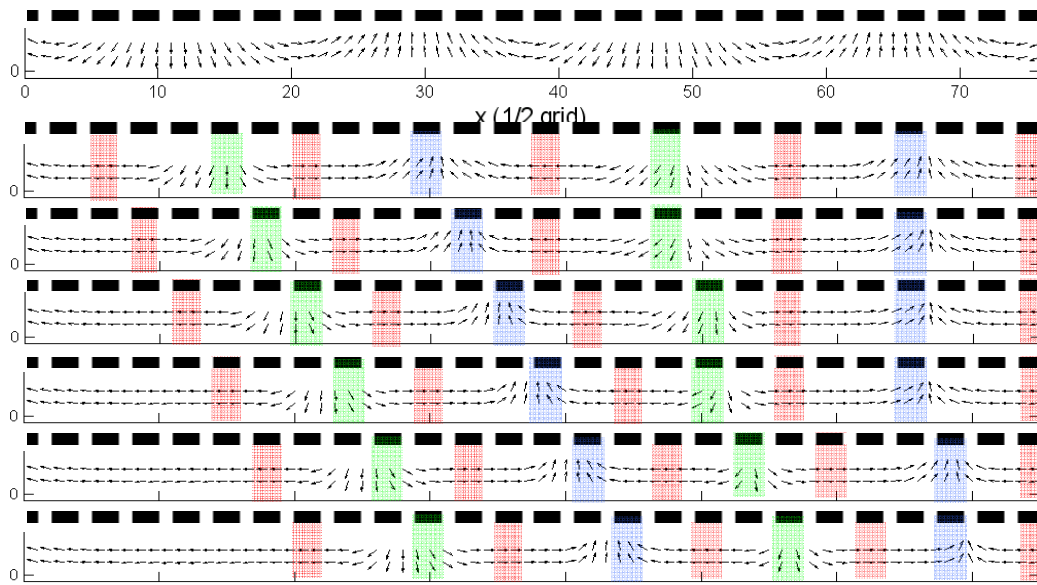


Fig. 4.12 Period tuning of dual frequency LCPGs device (director configuration
in x-y plane of middle of the cell) with 15ms time period between each step

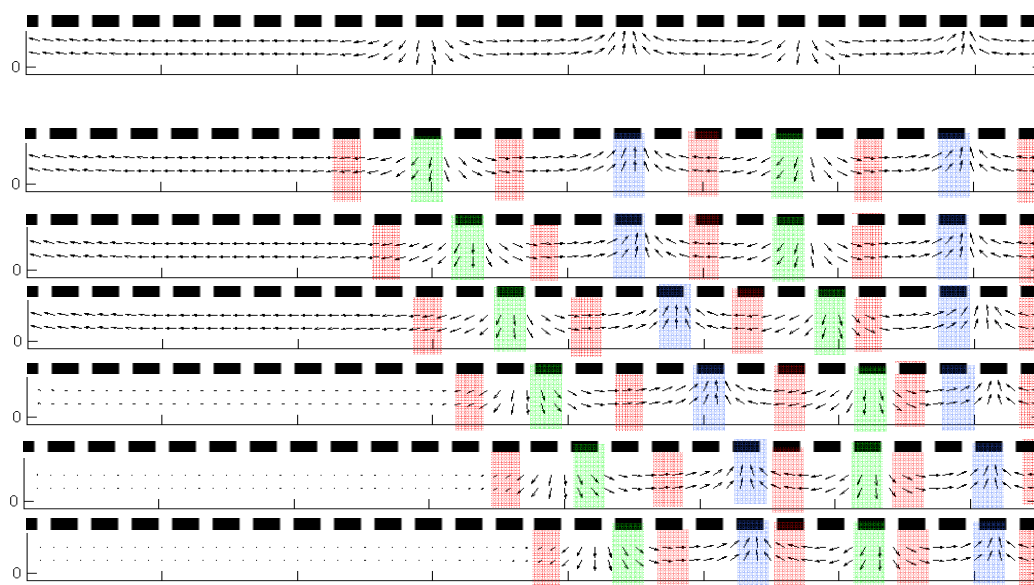


Fig. 4.13 Continue to squeeze the period of LCPGs device with relaxation to vertical

state in the blank region with 15ms time period between each step

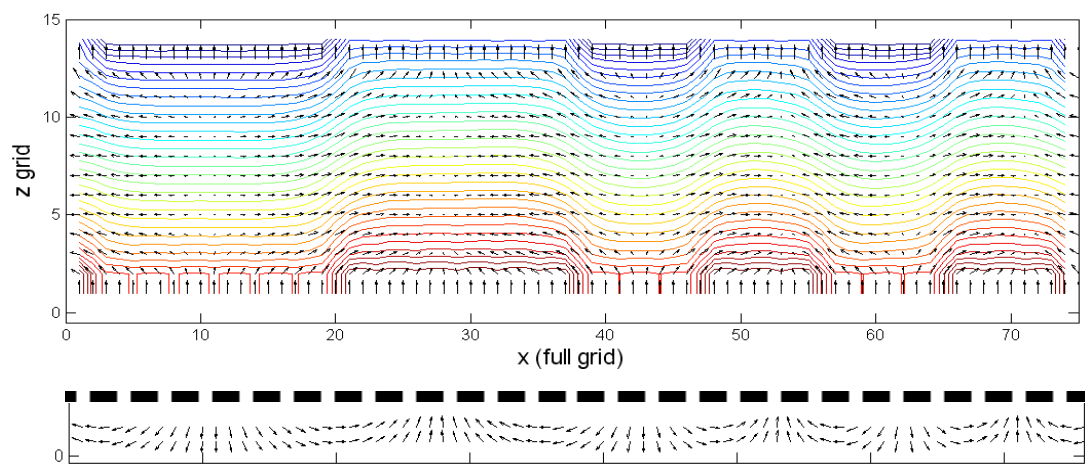


Fig. 4.14 Two squeezed full period of grating with a nucleated full period of grating in
the previous blank region

Electrode #	1	2	3	4	5	6	7	8
Step 0	10	12	12	12	10	10	10	12
Step 1	10	12	12	12	12	10	12	12
Step 2	10	10	12	12	12	10	12	12
Step 3	10	10	10	12	12	10	12	12
Step 4	10	10	10	10	12	10	12	12

(a) Voltage on bottom substrate (V)

Electrode #	1	2	3	4	5	6	7	8
Step 0	0	2	2	2	0	0	0	2
Step 1	0	2	2	2	2	0	2	2
Step 2	0	0	2	2	2	0	2	2
Step 3	0	0	0	2	2	0	2	2
Step 4	0	0	0	0	2	0	2	2

(b) Voltage on top substrate (V)

Table 4.1 Driving scheme of walking method

Electrode #	1	2	3	4	5	6	7	8
Step 0	10	10	12	10	12	10	10	10
Step 1	10	12	12	10	10	12	12	10
Step 2	10	12	12	12	10	10	10	12

(a) Voltage on bottom substrate

Electrode #	1	2	3	4	5	6	7	8
Step 0	0	0	2	0	2	0	0	0
Step 1	0	2	2	0	0	2	2	0
Step 2	0	2	2	2	0	0	0	2

(b) Voltage on top substrate

Table 4.2 Driving scheme of Jumping method

Electrode #	1	2	3	4	5	6	7	8
Step 0	10	12	10	12	10	12	10	12
Step 1	0	0	0	0	0	0	0	0
Step 2	0	0	2	0	0	2	0	0
Step 3	10	12	12	12	10	10	10	12

(a) Voltage on bottom substrate

Electrode #	1	2	3	4	5	6	7	8
Step 0	0	2	0	2	0	2	0	2
Step 1	0	0	0	0	0	0	0	0
Step 2	0	0	0	0	0	0	0	0
Step 3	0	2	2	2	0	0	0	2

(b) Voltage on top substrate

Table 4.3 Driving scheme of resetting method

		Electrodes Number																									
Step Number		1	2	3	4	5	6	7	8	9	10	11	12	13	14	15	16	17	18	19	20	21	22	23	24	25	26
	1	0	0	10	0	0	0	0	10	0	0	0	0	0	10	0	0	0	0	0	10	0	0	0	0	0	10
	2	0	0	0	10	0	0	0	0	10	0	0	0	0	10	0	0	0	0	0	10	0	0	0	0	0	10
	3	0	0	0	0	10	0	0	0	0	10	0	0	0	0	10	0	0	0	0	10	0	0	0	0	0	10
	4	0	0	0	0	0	10	0	0	0	0	10	0	0	0	0	10	0	0	0	10	0	0	0	0	0	10
	5	0	0	0	0	0	0	10	0	0	0	0	10	0	0	0	0	10	0	0	0	10	0	0	0	0	10
	6	0	0	0	0	0	0	0	10	0	0	0	0	10	0	0	0	0	10	0	0	0	10	0	0	0	10

Table 4.4 driving scheme for translating the boundaries in positive mode (first six steps, unit:

V)

		Electrodes Number																									
Step Number		1	2	3	4	5	6	7	8	9	10	11	12	13	14	15	16	17	18	19	20	21	22	23	24	25	26
	1	0	0	0	0	0	0	0	0	5	0	0	0	5	0	0	0	0	5	0	0	0	5	0	0	0	5
	2	0	0	0	0	0	0	0	0	0	5	0	0	0	5	0	0	0	5	0	0	0	5	0	0	0	5
	3	0	0	0	0	0	0	0	0	0	0	5	0	0	0	5	0	0	0	5	0	0	5	0	0	0	5
	4	0	0	0	0	0	0	0	0	0	0	0	5	0	0	0	5	0	0	0	5	0	0	5	0	0	5
	5	0	0	0	0	0	0	0	0	0	0	0	0	5	0	0	0	5	0	0	5	0	0	5	0	0	5
	6	0	0	0	0	0	0	0	0	0	0	0	0	0	5	0	0	5	0	0	5	0	0	5	0	0	5

Table 4.6 driving scheme for translating the boundaries in positive mode (next six steps, unit: V)

		Electrodes Number																									
Step Number		1	2	3	4	5	6	7	8	9	10	11	12	13	14	15	16	17	18	19	20	21	22	23	24	25	26
	1	0	0	0	0	0	0	0	0	0	0	-40	0	0	0	0	40	0	0	0	-40	0	0	0	40	0	0
	2	0	0	0	0	0	0	0	0	0	0	0	-40	0	0	0	40	0	0	0	-40	0	0	0	40	0	0
	3	0	0	0	0	0	0	0	0	0	0	0	0	-40	0	0	0	40	0	0	0	-40	0	0	0	40	0
	4	0	0	0	0	0	0	0	0	0	0	0	0	0	-40	0	0	0	40	0	0	0	-40	0	0	40	0
	5	0	0	0	0	0	0	0	0	0	0	0	0	0	0	-40	0	0	0	40	0	0	-40	0	0	40	0
	6	0	0	0	0	0	0	0	0	0	0	0	0	0	0	0	-40	0	0	40	0	0	-40	0	0	40	0

Table 4.7 driving scheme for translating the center in negative mode (next six steps, unit: V)

V-COPA v3.0 Program Overview

1. Introduction

V-COPA v3.0 is a user friendly numerical program with GUI based on MATLAB for numerical modeling the tunable liquid crystal polarization gratings (LCPGs) device. It integrates equilibrium LC3D modeling, dynamics LC3D modeling, LC director visualization, Polarized optical microscopy visualization, and optical simulation based on scalar integral method or FDTD method in an easy-to-use graphic environment. Its typical function includes:

- Device parameter setup
- Control parameters setup
- Optical parameters setup
- Voltage pattern setup and design
- LC3D simulation
- 2D scalar integral
- FDTD simulation
- Liquid crystal director visualization
- Polarized optical microscopy visualization

V-COPA is a numerical modeling program based on MATLAB environment that allows the user to design, investigate and demonstrate the features related to the liquid

crystal polarization gratings, especially with different options, such as single frequency LCPGs, dual frequency LCPGs. Both the equilibrium and dynamics modeling are encoded in the package to study different perspective of LCPGs device.

2. V-COPA v3.0 System

On Windows platforms, such as Windows XP, and Vista, there are two ways to start the V-COPA program. One is run the executable file in the folder of V-COPA v3.0. Another is first starting MATLAB v7.1 (or any later version), then run the Matlab .m file from the Matlab Editor. The first method can simply start the program by clicking the VCOPA_main.exe. However, it requires the Windows platform to be installed compatible MCRInstaller.exe first as shown in Fig. [7.1](#). The second method is shown in Fig. [7.2](#). Run the program VCOPA_main.m from the Matlab editor.

After run the program, the main graphic interface will pop up as shown in Fig. [7.3](#). The main dialog consists eight functional buttons, including device setting, control setting, optical setting, voltage input, V-COPA OPM, run 2D scalar, director draw, and polarized optical microscopy. In general, the user can set up the device parameter, control setup, optical setup. Then design the input voltage profile on the bottom substrate and top substrate. Next run VCOPA_OPM to implement the Liquid crystal director modeling. Given the LC director configuration, 2D scalar integral is able to investigate the optical performance, such as the near field and far field phase profile, diffraction pattern, etc. To visualize the results, LC director draw and Polarized optical microscopy draw are several important features of the V-COPA

program. Such buttons as “about”, “updates”, “demo”, and “help” are also provided to guide the user to start the program.

- **Device setting**

Click the “device setting” button in the main window, the program is proceeding to the device setting panel as shown in Fig. [7.4](#). The device configuration features with liquid crystal material properties, LC panel properties, and specific surface alignment.

Liquid crystal material properties:

Liquid Crystal Name: input the LC material name, such as MLC-2048, MLC-2049 or some other materials.

Elastic constant: input the value of splay, bend, and twist elastic constant, and q_0 .

Dielectric anisotropy: the top one is the default dielectric anisotropy if using single frequency LC material; If checked with dual frequency option, the top one is the default positive dielectric anisotropy with low frequency electric field, while the bottom one is the negative dielectric anisotropy with high frequency electric field.

Birefringence (refractive index): the ordinary and extraordinary refractive index, no dispersion considered in the V-COPA program.

n_glass/ep_glass: relevant refractive index, and dielectric constant for simple glass

LC panel properties:

Thickness: cell gap (thickness) of the V-COPA LC cell.

Surface alignment: the pretilted and rubbing angle of top and bottom substrate respectively. If checked with the option of detailed alignment design, and click the button of details, the program will pop up the surface alignment design panel that has the capability of multi domain alignment with different pixel groups. Details of designing surface alignment will be introduced in the next section.

Option to extrapolate the surface alignment to bulk: If checked, the program will extrapolate the surface alignment configuration to the bulk of LC cell. Otherwise, will simply using the initial vertical alignment.

Electrode width: width of each electrode in the substrate

Gap width: width between two electrodes

Electrode number: define the number of electrodes that will be modeled in the top or bottom substrate. Note that to meet the periodical boundary condition in some cases, we split the first electrode into half, place the first half as the first electrode, and the second half as the last one. For example, input 10 electrodes, the system will generate 0.5, 9, and 0.5 electrodes. From the visual viewpoint, it seems like 11 electrodes in the system.

Save/load: in general, all the parameter setting panels have the functions to save/load the parameter configuration to the user defined directory and filename, as shown in Fig. [7.5](#).

Specific surface alignment:

Check the option of design specific alignment, and click the details button, the

program will pop up the specific surface alignment panel as shown in Fig. [7.6](#). According to the defined electrode number, e.g., 10, and the pixel size (electrode width, gap width), the surface alignment panel will automatically load the electrodes and gaps as shown in the Fig. [7.6](#). Extra one will be shown because of the periodical boundary condition definition.

Click every electrode number in the left listbox, or the gap number in the right listbox, the relevant values of the polar angles and azimuthal angles in that electrode or gap region will be shown in the right of listbox. User is able to input or change the value according to the design. The revision or input will be automatically updated and saved into the database of the system. Additional reset functions are added to make it easy to access and define all the angles of top or bottom electrodes in Fig. [7.7\(a\)](#). Duplicate functions are provided to fast copy the design from the top/bottom to the bottom/top substrate in Fig. [7.7\(b\)](#). Once the user is done with the surface alignment design, click the alignment table button, one can check and view the surface alignment tables as shown in Fig. [7.8](#). If there are any typo or mistakes when inputting the values, the user is able to figure it out easily.

● Control setting

To numerical model the program, we need to define the control parameters required for the simulation program, as shown in the Fig. [7.9](#). It includes LC3D control settings, boundary conditions, initial condition control, fixed parameters, and modeling methods.

LC3D control settings:

X/Y/Z grid size: define the grid size of the lattice along x, y and z axis of each micron.

C: define the relaxation speed of LC3D modeling.

tol: define the stopping condition of the relaxation loops if the convergence condition is satisfied.

Maxloops: define the stopping condition of the relaxation loops if the convergence condition is not meet and the number of total iterations will be processed in the simulation.

W, maxVerr, MaxViter: define the corresponding parameters in the voltage relaxation process, similar as c, tol, maxloops respectively.

Boundary condition:

Boundary Condition (B.C.) for x: if check the option, the system will use free boundary condition, that is, at the boundary, the virtual grids (using for the calculation) is linear extrapolated from the two closest grids near the boundary. If not check, the system will employ the periodical boundary condition, that the left/right boundary ($x=1$ or Numx) is equal to the right one (Numx or 1).

Boundary condition for V: if check the option, along z axis, $dV/dz = 0$ at the boundary of glass substrate region in top or bottom. If not check, $V = 0$ at the boundary along z axis.

Initial condition control:

Restart/continue: If check the box, the system will load the previous simulation results of director configuration as the initial condition for the current simulation. If not, the system will initialize the director configuration based on the surface alignment or vertical configuration.

Initial voltage: If check the box, the system will first run and relax the applied voltage without considering the LC configurations. If not, the system will load the voltage profile obtained from the previous simulation.

Display figures: If check the box, after the simulation, the results will be popped up as displayed figures. If not, figures will not be shown to reduce the memory requirement of system.

Fixed parameters:

There are several fixed parameters originated from the Fortran code of LC3D. The user can not revise these parameters unless the Fortran code is revised on these parameters and compile with the dll file for Matlab program again. The fixed setting includes: Dimension of simulation (2D in V-COPA program), the maximum size of the lattice in x, y and z axis. (sizex = 300, sizey = 10, sizez = 70)

Calculation methods:

Vector method: using nx, ny, and nz to represent the free energy of LC, the order parameter S is fixed. If check the option of using dynamics method, the system will

employ the dynamics simulation of LC3D, instead of equilibrium simulation of LC3D.

[Dickman's Q tensor/Berreman's Q tensor method](#): not applicable in the current version of VCOPA program.

- **Optical control setting**

The parameters as shown in Fig. [7.10](#) will be employed in the scalar optics simulation or Finite difference Time domain (FDTD) simulation. The settings include:

[Wavelength](#): define the wavelength of incident Gaussian beam

[RHC or LHC](#): define the polarization state of the incident light, right hand circular polarization or left hand.

[Beam width/aperture](#): define the percentage of the clear aperture.

[Near field resolution](#): define the grid size in the near field of the model

[Far field resolution](#): define the grid size in the far field transformation.

[Far field angle range](#): define the total angle range in the far field.

Several typical parameters are employed in the FDTD simulation as shown in Fig. [7.10](#).

- **Voltage pattern design**

In the device setting panel, the user may choose which kind of LC materials to be used in the modeling, single frequency LC or dual frequency LC material. If choosing single frequency LC, click the voltage input panel, the voltage design panel will be

popped up as shown in Fig. [7.11](#). If choose dual frequency, another two options will be displayed, one is voltage profile of dual frequency LC in equilibrium relaxation of LC3D as shown in Fig. [7.12](#). Another is defined based on the dynamics relaxation routine, as shown in Fig. [7.13](#). Step number is to define how many different voltage profiles are employed in the total simulation of the dynamics processing. Time delay is the parameter defined for the period of time for each applied voltage profile. It features the tuning speed of the system. If the LC director is able to follow the updating of applied voltage profile, the time delay is the available response time, otherwise, the user has to modified the time delay to figure out the appropriate response time.

For single frequency voltage profile design, click input voltage button, the system will pop up the voltage input panel as shown in Fig. [7.14](#). Click each electrode number, the user is able to define the voltage value in the top and bottom substrate respectively. Additional reset function is provided to be easily access and control all the electrodes in top or bottom substrates. As for the equilibrium relaxation of dual frequency LC material, the voltage input is shown in Fig. [7.15](#). Each electrode has the inputs for both low frequency voltage value and high frequency voltage value on top and bottom substrate. As far as the dynamics relaxation is concerned to study the tuning speed of the V-COPA, the voltage input will be modified as Fig. [7.16](#). Several steps of voltage input are listed from the left to the right.

To check the input voltage profile on top or bottom substrate, click view voltage profile button, the system will pop up the current voltage design as shown in Fig. [7.](#)

[17](#) (equilibrium modeling), and Fig. [7.18](#) (dynamics modeling). Given the designed voltage profile, click the button of “initialize the input voltage profile”, the program will actually apply the voltage profile to the lattice of model. For a single frequency LC, no low frequency voltage is required in Fig. [7.19\(a\)](#), while the negative mode with high frequency field is shown in Fig. [7.19\(b\)](#).

- **VCOPA OPM: LC3D simulation**

This function features with the numerical modeling of LC director configuration by LC3D from Fortran subroutine.

When the user click the VCOPA OPM button in the main window, based on the defined device settings, control settings, and the voltage profile applied to the system, the program will try to reach the equilibrium state of LC director configuration. At first, the system will initialize the director configuration (or load the previous director configuration if the related option is selected). A three domain surface alignment on top or bottom substrate is shown in Fig. [7.20\(a\)](#) (top view) and Fig. [7.20\(b\)](#) (side view). Secondly, the LC3D will relax the applied voltage profile, and have an initialized voltage profile on the lattice, as shown in the side view of equi-potential field line in Fig. [7.21](#). According to the stopping condition, either convergence to the defined tolerance or reaching the maximum loop numbers, the program will obtain a final director configuration based on the designed voltage profile and surface alignment. For example, a typical liquid crystal polarization gratings is implemented in Fig. [7.22\(a-b\)](#).

- **Run 2D scalar modeling**

With the simulated director configuration of liquid crystal cell, we may study the optical properties if incident a circular polarized light into the V-COPA cell. The program will automatically pick one whole period of polarization grating (from one left boundary to the next right boundary), duplicate the period by 5 times or more, perform the Jones calculus through the cell and scalar integral from the near field to far field. The phase retardation of LCPGs is closed to half wave of the light as shown in Fig. [7.23](#). The deviation in Fig. [7.23](#) in some regions will cause the downgrade of the final efficiency. The near field intensity and phase profile are shown in Fig. [7.24\(a, b\)](#). By scalar integral from the near field to far field, the final diffraction efficiency can be obtained in Fig. [7.24\(c\)](#).

- **Run FDTD modeling**

Since Dr. Bin Wang has developed a robust FDTD subroutine, we will simply load the subroutine to simulate the FDTD, and compare with the results from Scalar integral. Click run FDTD, the program will start the FDTD modeling panel as shown in Fig. [7.25\(a\)](#). Load the modeled director configuration (in matlab data file with extension .mat) in Fig. [7.25\(b\)](#), convert to the required format (data file with extension .dat) of the FDTD subroutine as shown in Fig. [7.25\(c\)](#). Denote the directory to save the data, click “calculate” button, and the subroutine will perform the FDTD simulation and obtain the optical performance of the device.

- **Director draw**

To investigate the LC director configuration, a simple tool named as director draw is shown in Fig. [7.26](#). The user can pick up and view the x-y, x-z, and y-z plane of LC director configuration that modeled by the VCOPA_OPM subroutine.

- **Polarized optical microscopy draw**

As shown in Fig. [7.27](#), to compared with the experiment results, a visualization tool of polarized optical microscopy draw is also one of the program's features.

3. General simulation procedures

Based on the above functions of VCOPA v3.0, we can design or demonstrate a VCOPA device as shown in the flow diagram of Fig. [7.28](#).

4. Summary

In this section, we browse and surf the V-COPA v3.0 program programmed for the LCPGs device. With this user friendly program with GUI, the user can easily demonstrate the current design of liquid crystal polarization gratings, or propose, design, and develop other potential model. Since the program is based on the multi-domain surface alignment design and interdigital electrode pattern, the application of the V-COPA v3.0 is not only limited to the applications of LCPGs, other study can also employ this graphic program.

VCOPA_main	11 KB	Application	5/8/2009 6:34 AM
VCOPA_main	792 KB	MATLAB figure file	5/7/2009 10:39 PM
VCOPA_main	9 KB	MATLAB M-file	5/8/2009 5:33 AM
VCOPA_main.a	8 KB	ASV File	5/8/2009 4:32 AM
VCOPA_main.c	4 KB	CTF File	5/8/2009 6:34 AM
VCOPA_main_main	3 KB	C File	5/8/2009 6:34 AM
MCRInstaller	122,677 KB	Application	2/4/2006 1:03 AM
mccExcludedFiles	45 KB	Text Document	5/8/2009 6:34 AM
LC3D_Qtensor.f	1 KB	Fortran Source File	10/10/2006 4:36 PM
LC3D_Qtensor.c	5 KB	Application Extension	5/8/2009 1:54 AM
LC3D_PG_dyn	8 KB	Fortran Source File	11/14/2008 4:16 PM
LC3D_PG_dyn	2 KB	Application Extension	11/14/2008 4:17 PM
LC3D_PG_dual.f	5 KB	Fortran Source File	11/14/2008 3:45 PM

Fig. 7.1 Executable VCOPA_main.exe in the program folder

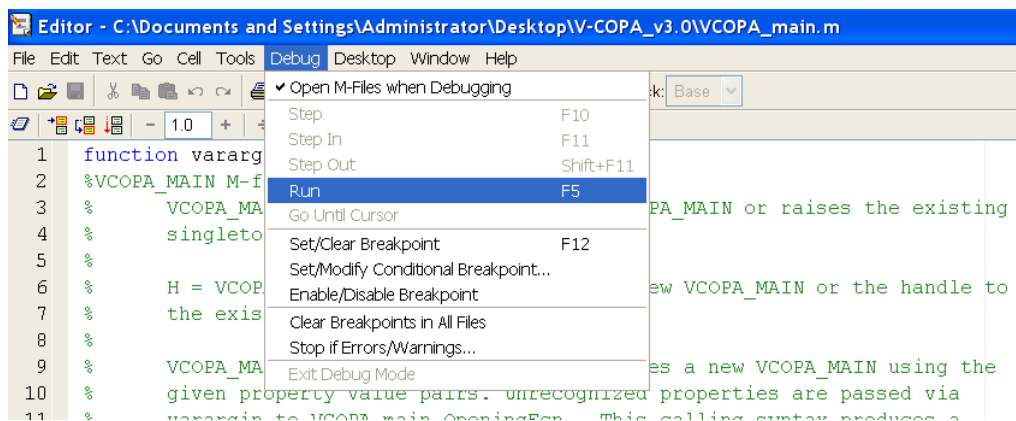


Fig. 7.2 Start the VCOPA program from Matlab editor

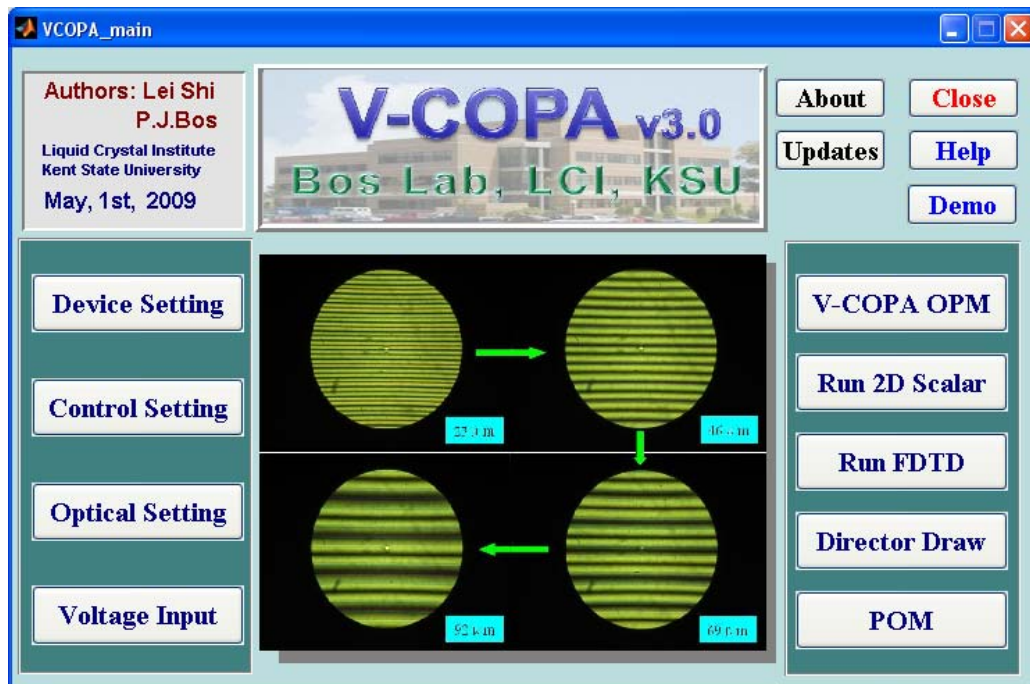


Fig. 7.3 Main window of VCOPA v3.0 program

VCOPA_configure

V-COPA Device Parameter Setting

Authors: Lei Shi, P.J. Bos, Bos Lab, LCI, Kent State Univ. All Rights Reserved

Liquid Crystal Features

Liquid Crystal Name: **MLC-2048**

Elastic Constant

K11	K22	K33	q0
16.7	7	18.1	e-12 N

Dielectric Anisotropy

$\epsilon_{//}$	ϵ_{\perp}	ϵ_0
6.32	3.1	

☒ **Dual Frequency LC? For high frequency:**

$\epsilon_{//}$	ϵ_{\perp}	ϵ_0
3	6.08	

Refractive Index

ne	no
1.5514	1.4737

n_glass: 1, ϵ_{glass} : 4.5, ϵ_0 : 8.8542 e-12

Panel Feature

Thickness: 5 μm

Surface Alignment

Top Pretilt Angle	Bottom Pretilt Angle
90	90

Top Azimuthal Angle	Bottom Azimuthal Angle
90	90

☒ **Design Specific Alignment?** Details

☐ **Surface extrapolate to bulk initially?**

Electrode width: 2 μm , Gap width: 1 μm , Electrode Num: 10

C:\Documents and Settings\Administrator\Desktop\V-COPA_v3.0

Save
Save as ...
Load ...
Help
Back

Fig. 7.4 Device setting of VCOPA v3.0 program

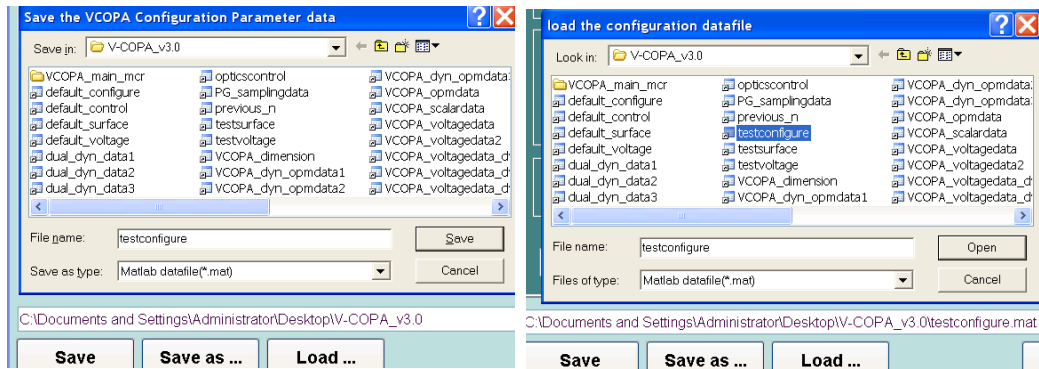


Fig. 7.5 Save and load function of VCOPA v3.0 program

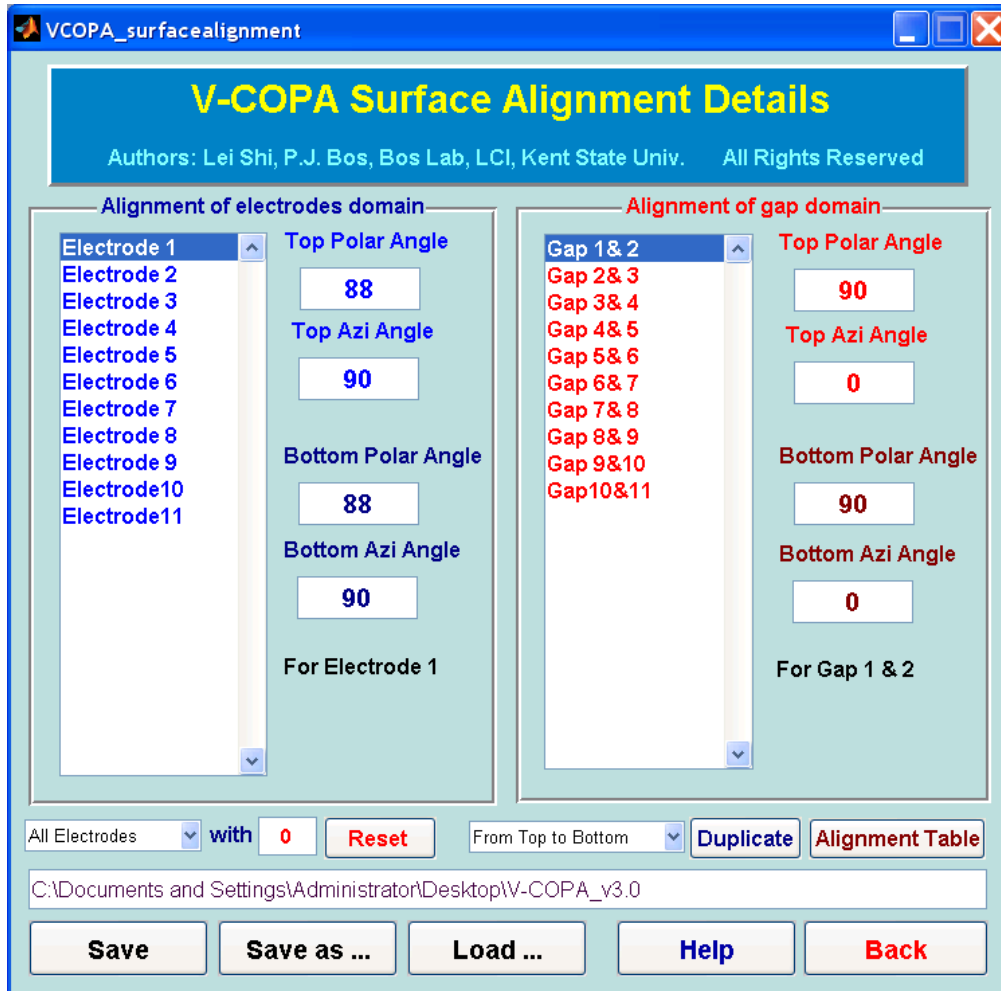


Fig. 7.6 Surface alignment design panel of VCOPA v3.0

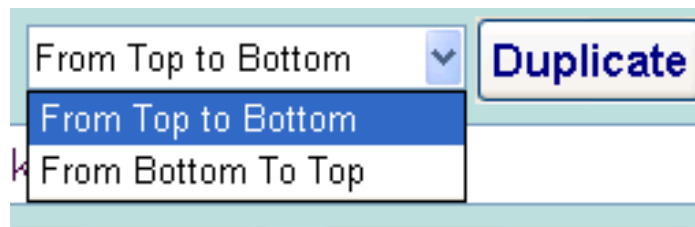
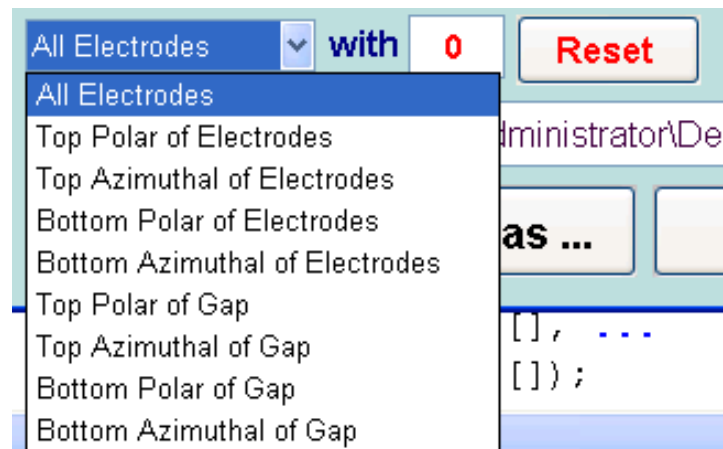


Fig. 7.7 (a) Reset function of surface alignment

(b) Duplicate function of surface alignment

view_surface

Table of Surface Alignment in Electrodes Region

Electrode #	1	2	3	4	5	6	7	8	9	10	11
Polar Angle (Top)	88	88	88	88	88	88	88	88	88	88	88
Azi Angle (Top)	90	270	270	270	90	90	90	270	270	270	90
Polar Angle (Bot)	88	88	88	88	88	88	88	88	88	88	88
Azi Angle (Bot)	90	270	270	270	90	90	90	270	270	270	90

Table of Surface Alignment in Gaps Region

Gap #	1	2	3	4	5	6	7	8	9	10
Polar Angle (Top)	90	90	90	90	90	90	90	90	90	90
Azi Angle (Top)	0	0	0	0	0	0	0	0	0	0
Polar Angle (Bot)	90	90	90	90	90	90	90	90	90	90
Azi Angle (Bot)	0	0	0	0	0	0	0	0	0	0

Back

Fig. 7.8 View table of surface alignment on electrodes and gaps

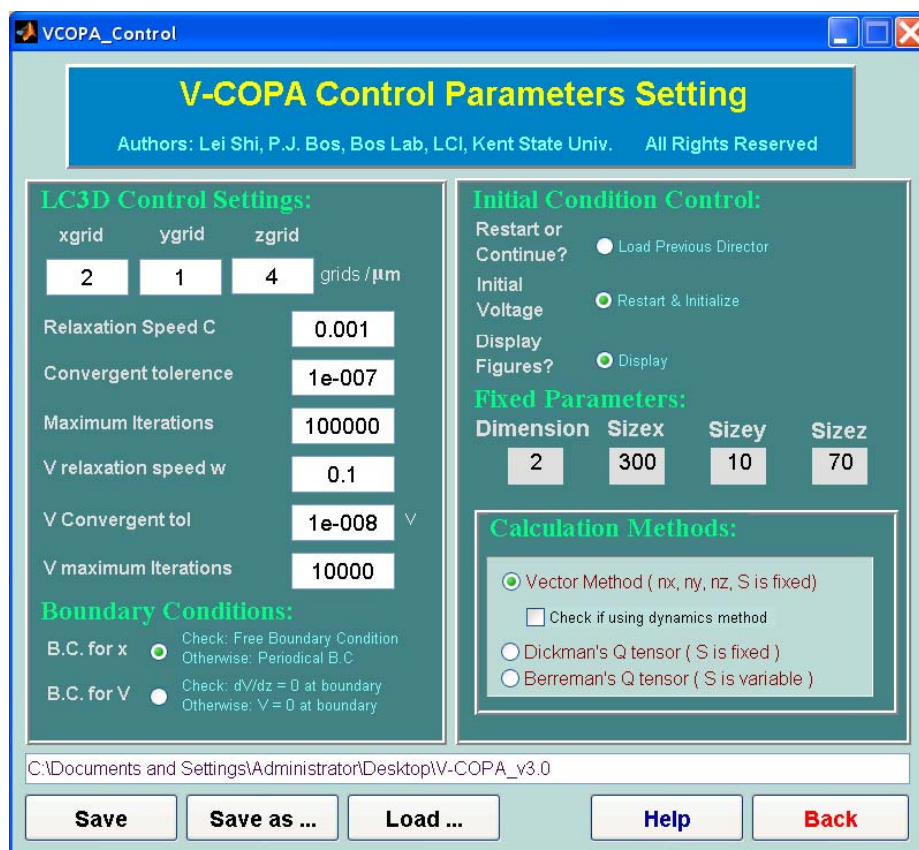


Fig. 7.9 Control settings of VCOPA v3.0 program

VCOPA_opticalcontrol

V-COPA Optical Control Parameters

Authors: Lei Shi, P.J. Bos, Bos Lab, LCI, Kent State Univ. All Rights Reserved

Light Information

Wavelength μm

Polarization State ☒ LHC ☐ RHC

Scalar Optics Control:

Optical Beam Width/Aperture

Optical Near Field Resolution

Optical Far Field Angle Range

Optical Far Field Sampling Pts.

FDTD Control:

Conductivity

Permeability

Magnetic Loss

FDTD Resolutio Pts./Wave

PML Thickness Points

PML Reflector

Decay Factor

Structure Bottom grids

Help
Save & Back

Fig. 7.10 Optical control settings of VCOPA v3.0 program

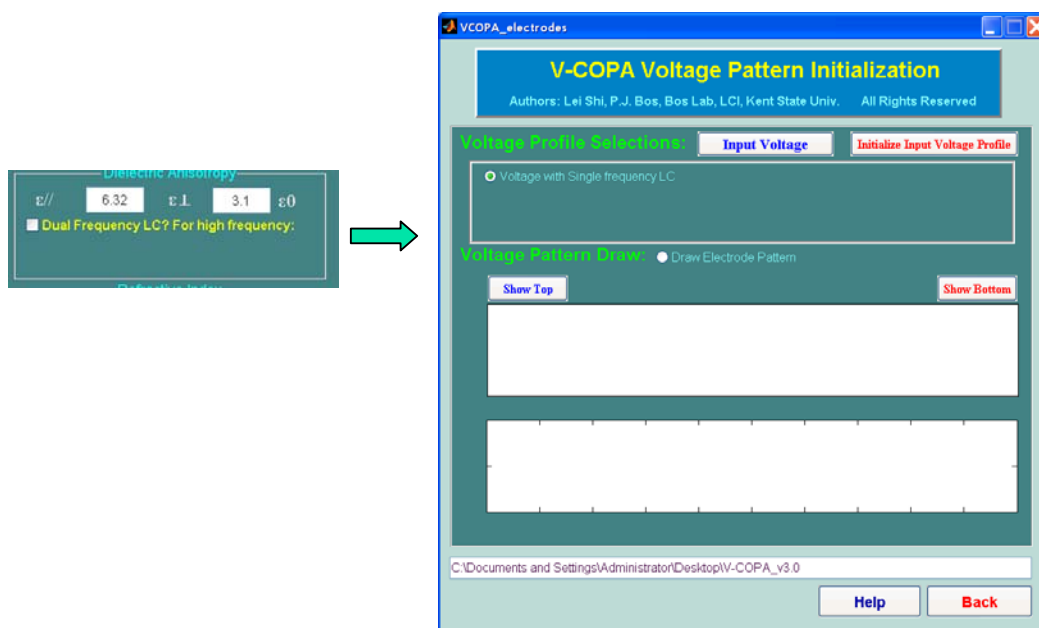


Fig. 7.11 Voltage initialization panel of single frequency LC

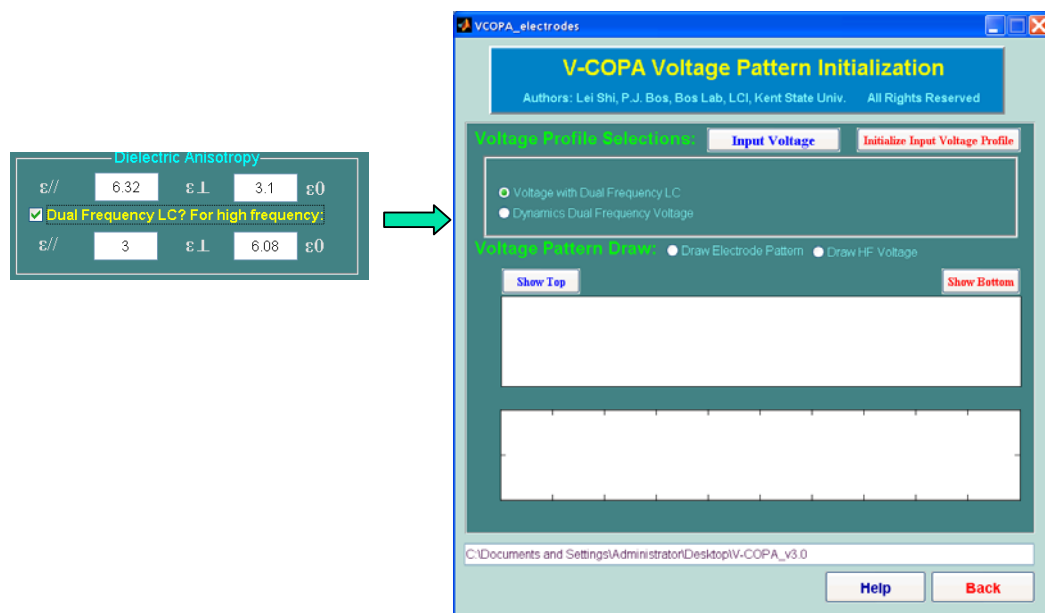


Fig. 7.12 Voltage initialization panel of dual frequency LC
in equilibrium modeling

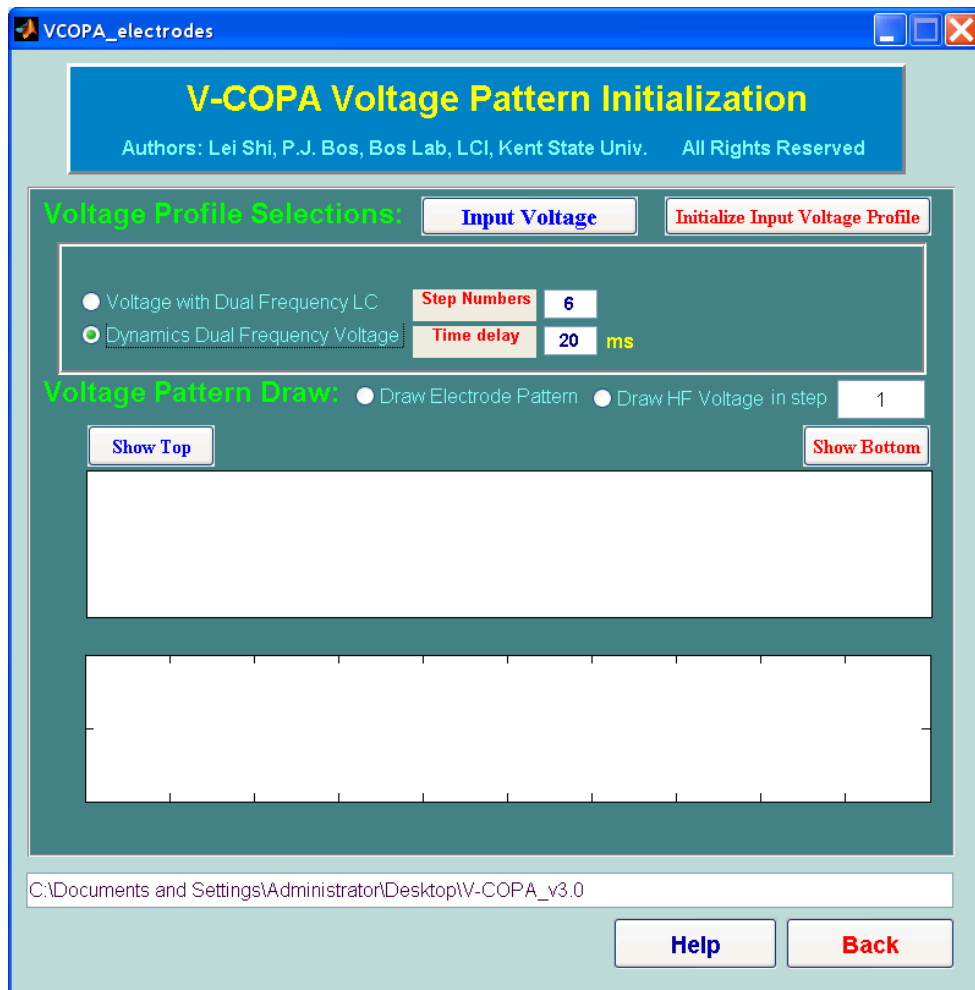


Fig. 7.13 Voltage initialization panel of dual frequency LC
in dynamics modeling

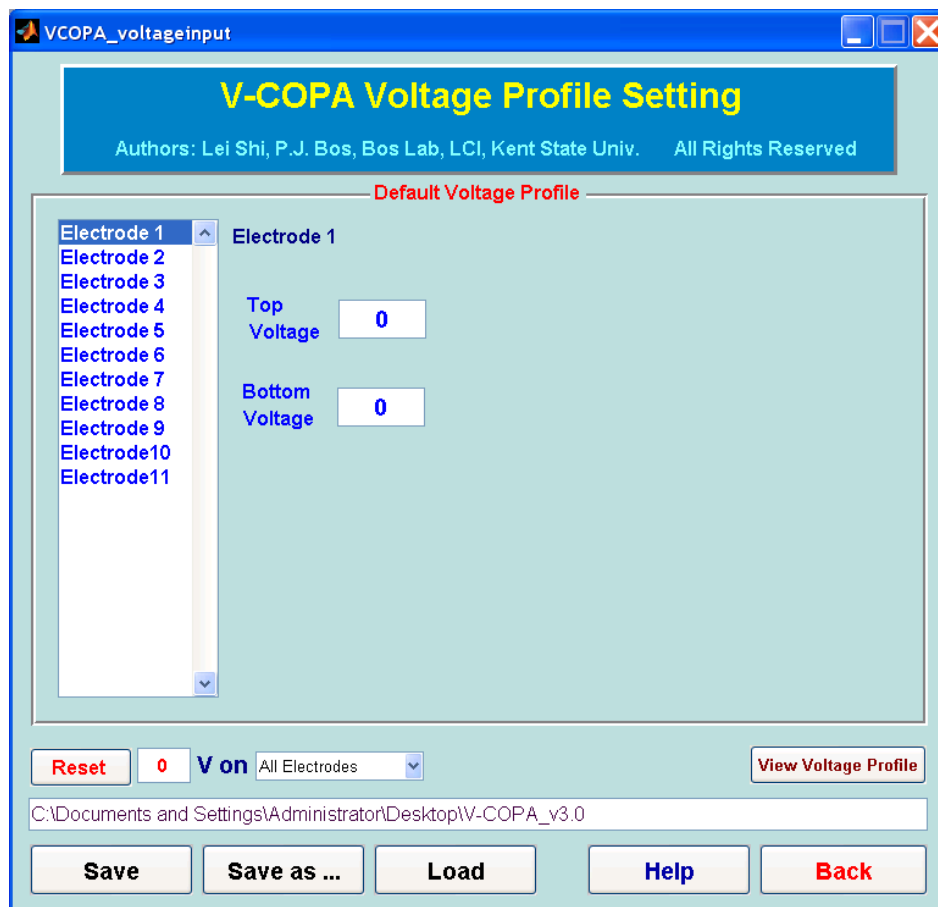


Fig. 7.14 Voltage profile settings in single frequency VCOPA

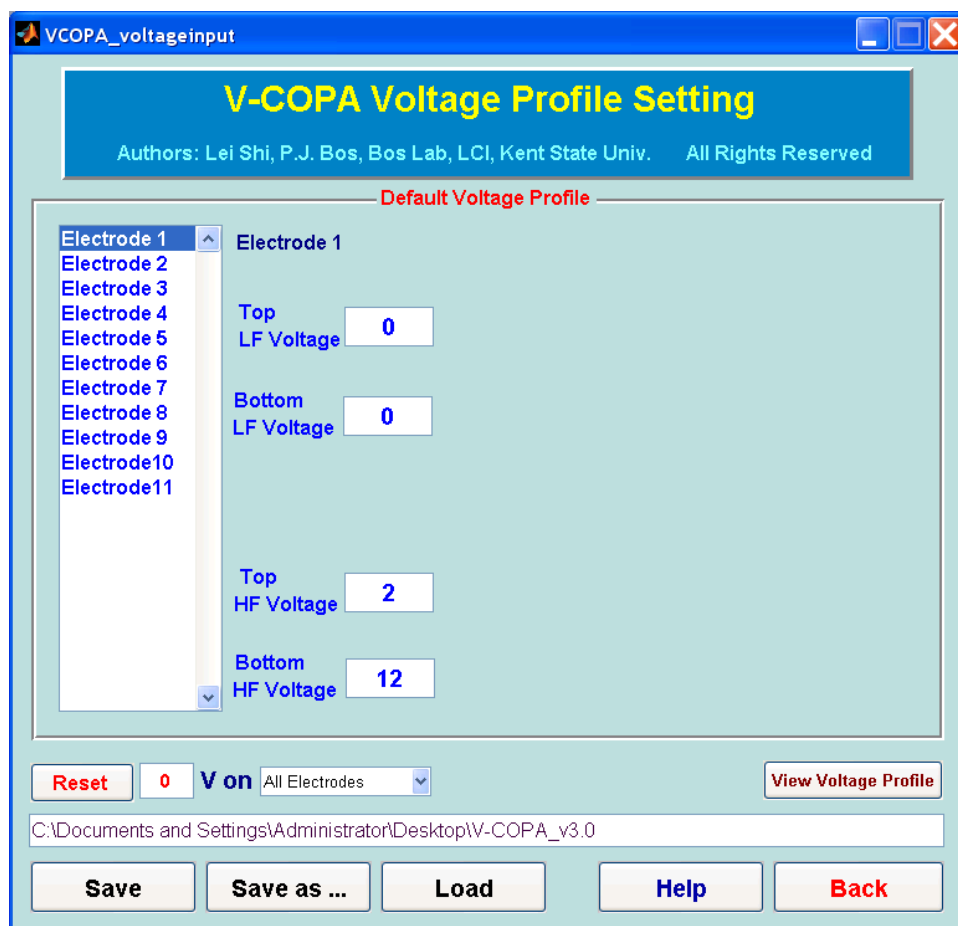


Fig. 7.15 Voltage profile settings in dual frequency VCOPA in equilibrium modeling

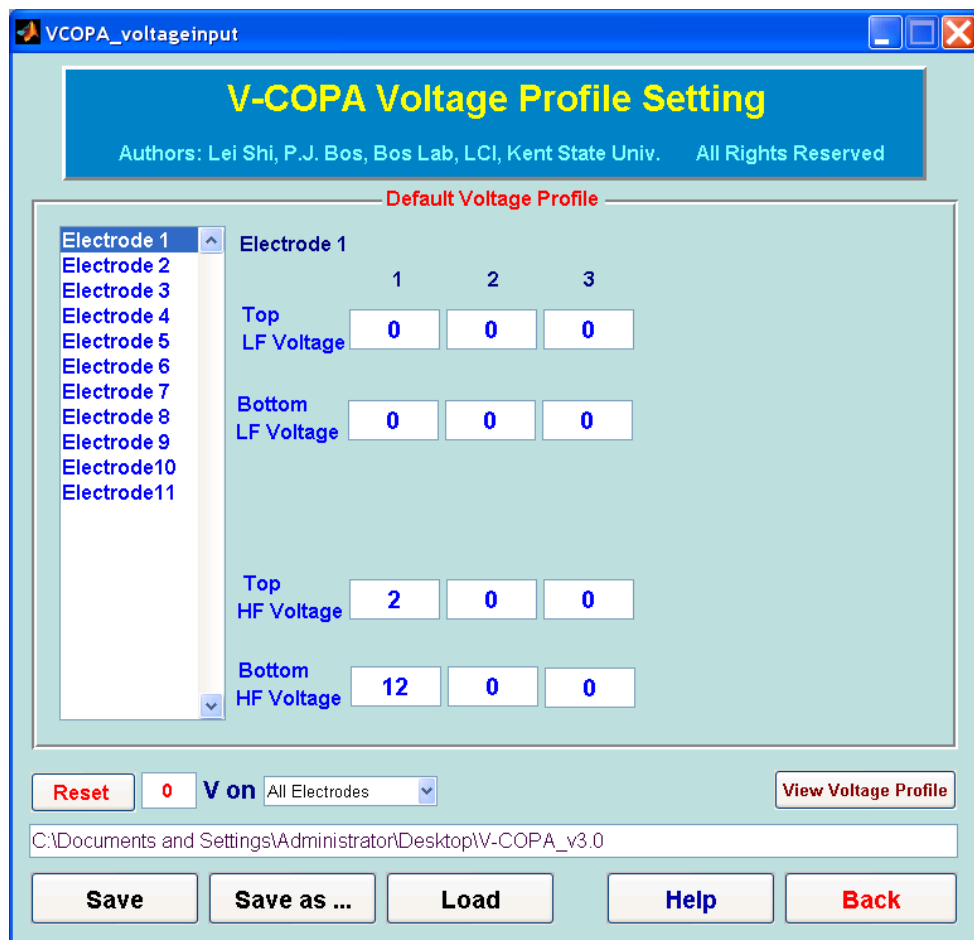


Fig. 7.16 Voltage profile settings in dual frequency VCOPA in dynamics modeling

Electrode #	1	2	3	4	5	6	7	8	9	10	11
LF Top	0	0	0	0	0	0	0	0	0	0	0
LF Bot	0	0	0	0	0	0	0	0	0	0	0
HF Top	2	0	0	0	2	2	2	0	0	0	2
HF Bot	12	10	10	10	12	12	12	10	10	10	12

Back

Fig. 7.17 Voltage table of single/dual frequency VCOPA in equilibrium modeling

The screenshot shows a software window titled "view_voltage" with a standard Windows-style title bar. Inside the window, there is a section titled "Voltage Input Table". This section contains a table with 11 columns labeled "Electrode #" (1 through 11) and 3 rows labeled "Step 1", "Step 2", and "Step 3". All cells in the table contain the value "0". Below the table, there are four radio buttons: "LF Top" (which is selected), "LF Bottom", "HF Top", and "HF Bottom". To the right of these buttons is a "Back" button.

Electrode #	1	2	3	4	5	6	7	8	9	10	11
Step 1	0	0	0	0	0	0	0	0	0	0	0
Step 2	0	0	0	0	0	0	0	0	0	0	0
Step 3	0	0	0	0	0	0	0	0	0	0	0

☒ LF Top
 ☐ LF Bottom
 ☐ HF Top
 ☐ HF Bottom
 Back

Fig. 7.18 Voltage table of single/dual frequency VCOPA in dynamics modeling

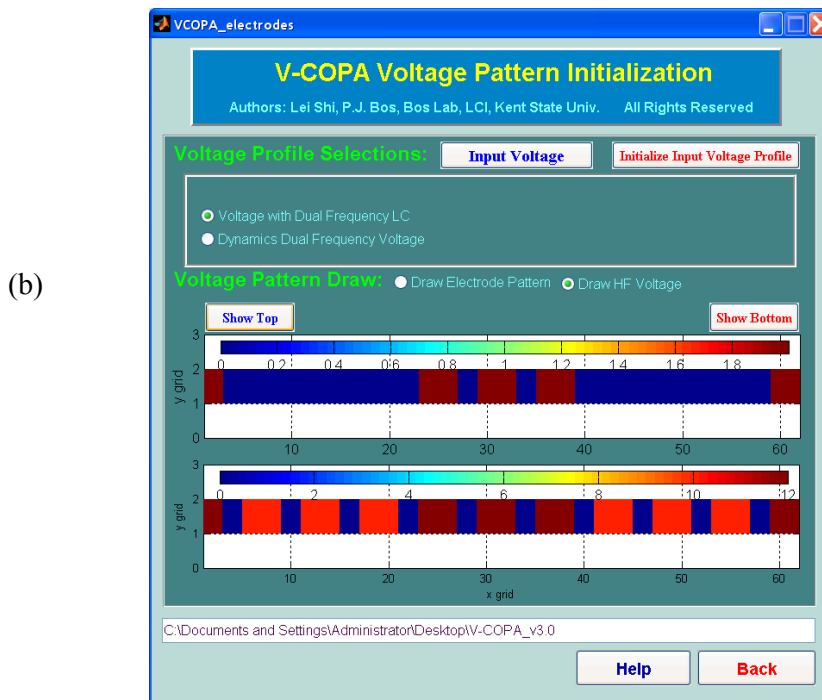
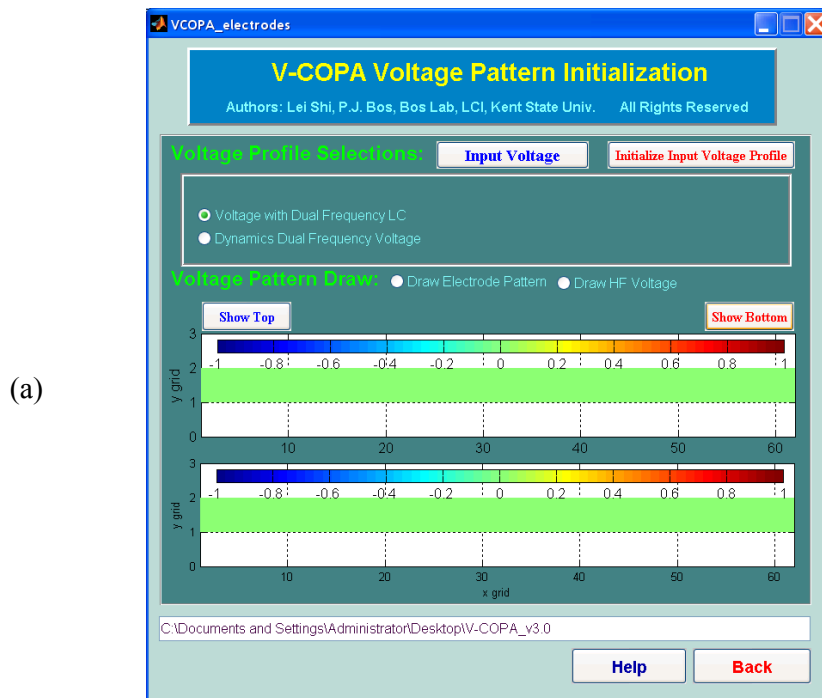


Fig. 7.19 (a) Voltage pattern of low frequency field
(b) voltage pattern of high frequency field

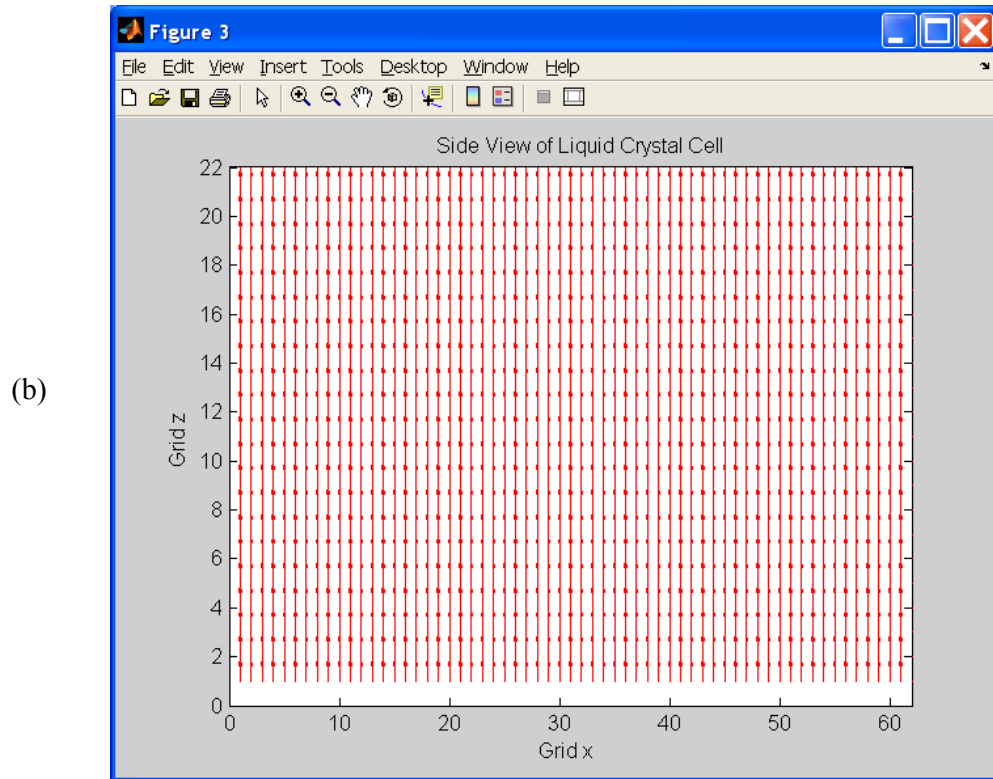
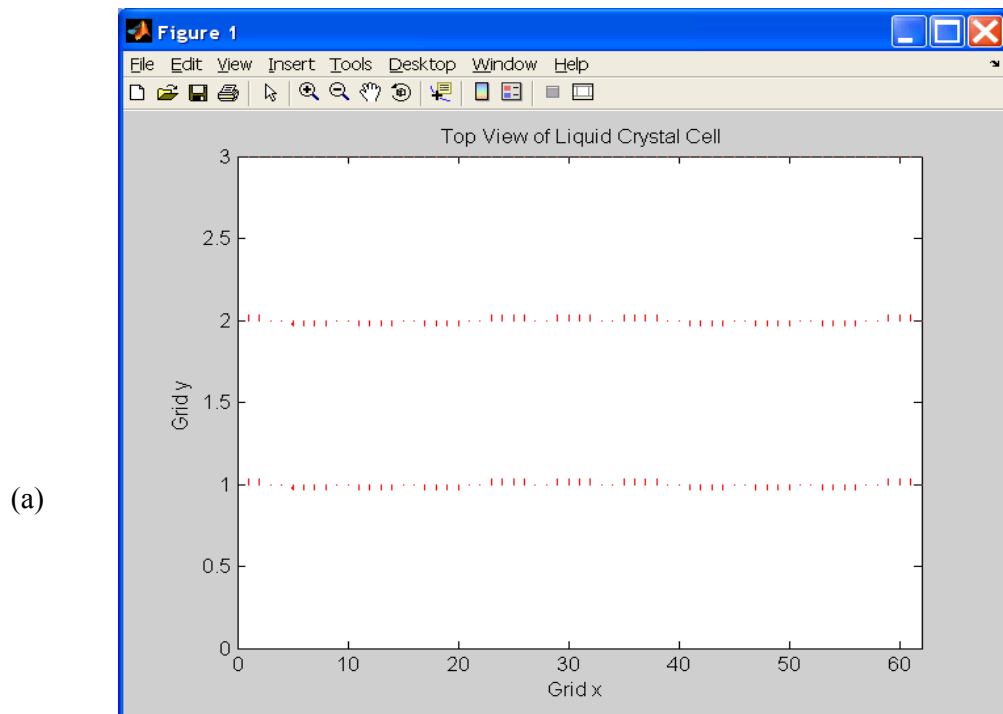


Fig. 7.20 (a) Top view of initial LC director configuration at one substrate; (b) Side view of initial LC director configuration

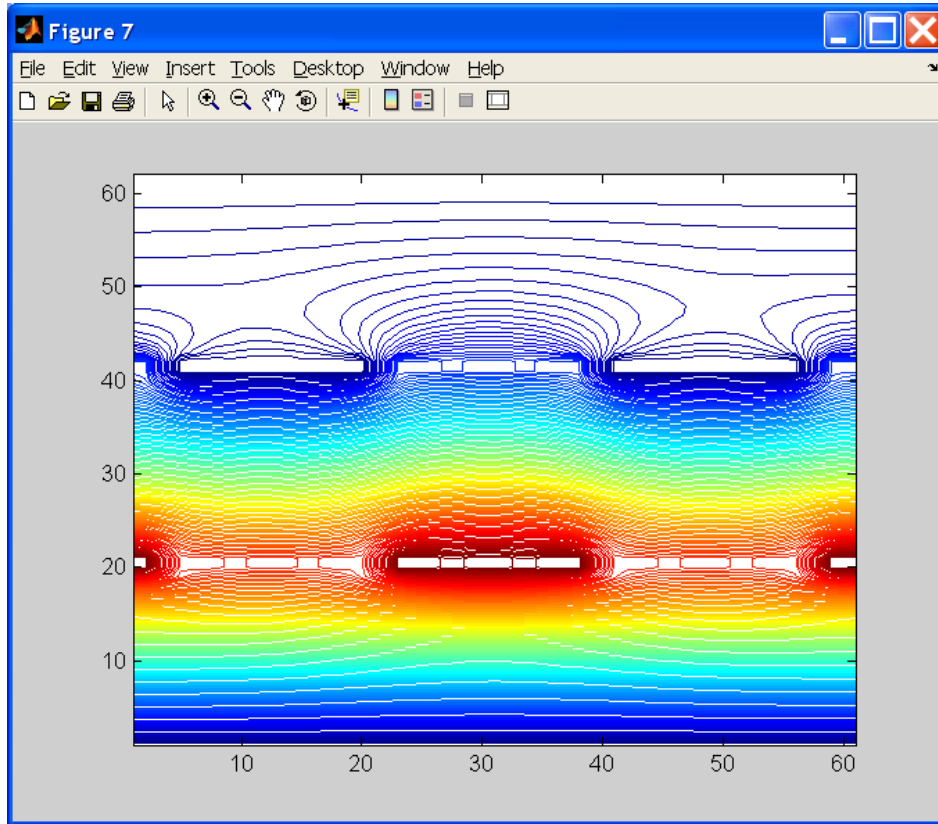
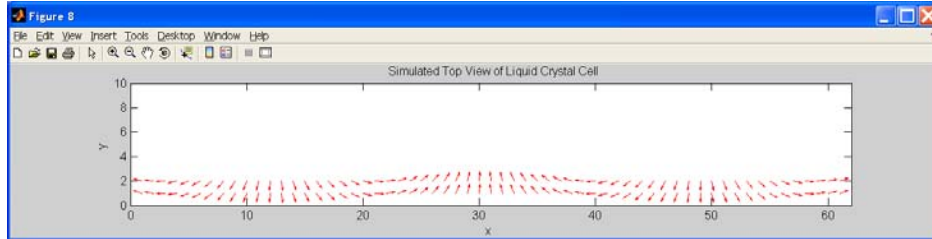


Fig. 7.21 Equi-potential field with high frequency voltage in x-z plane of dual frequency VCOPA

(a)



(b)

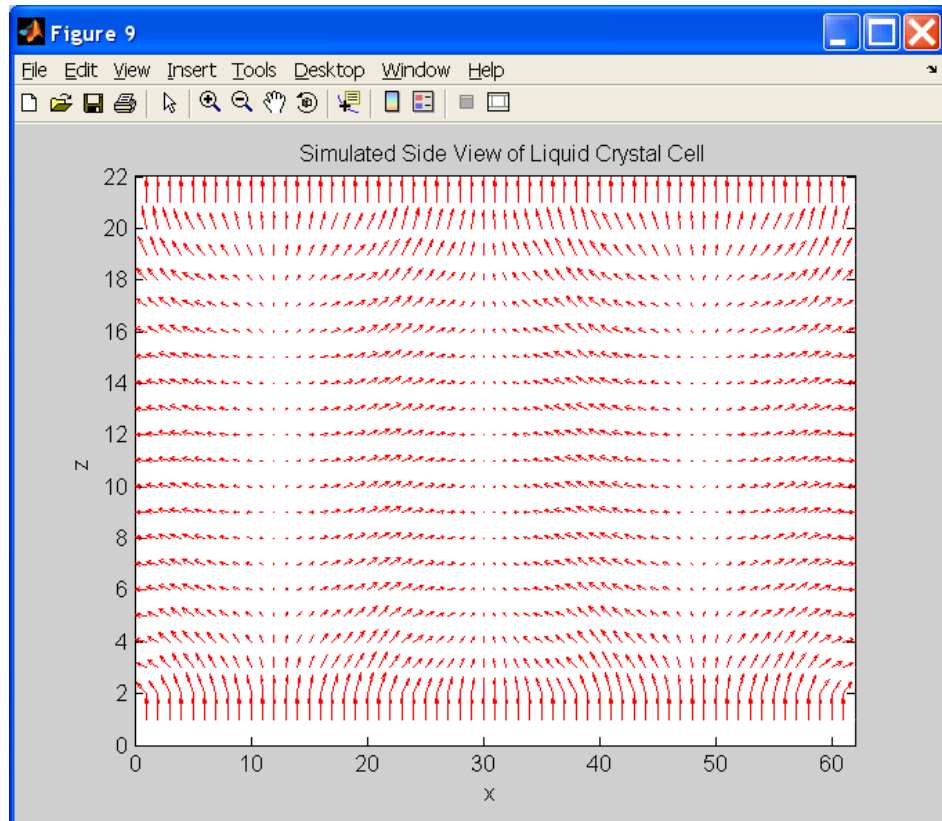


Fig. 7.22 (a) Top view of modeled VCOPA director configuration

(b) Side view of modeled VCOPA director configuration

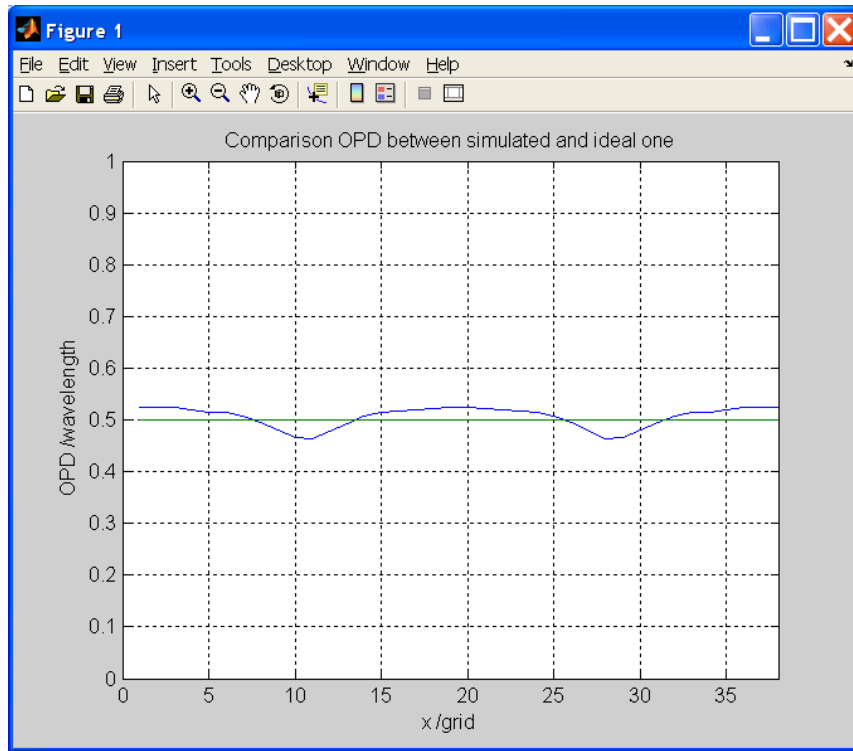
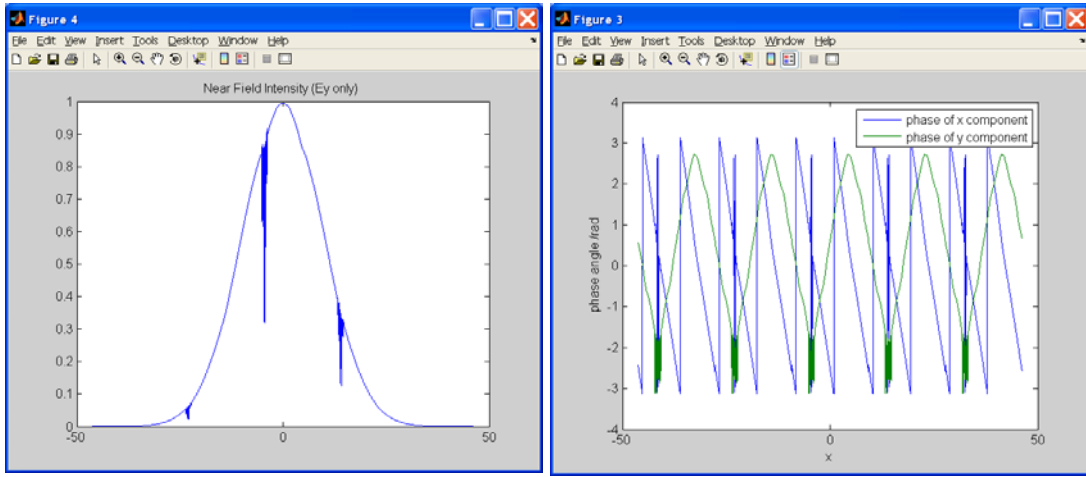
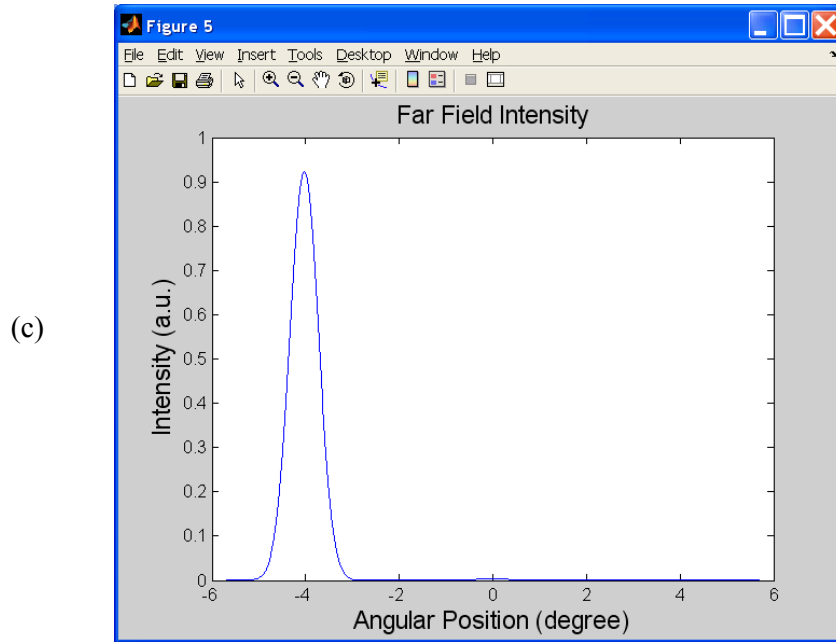


Fig. 7.23 Phase retardation of VCOPA along x and comparison with half-wave retardation



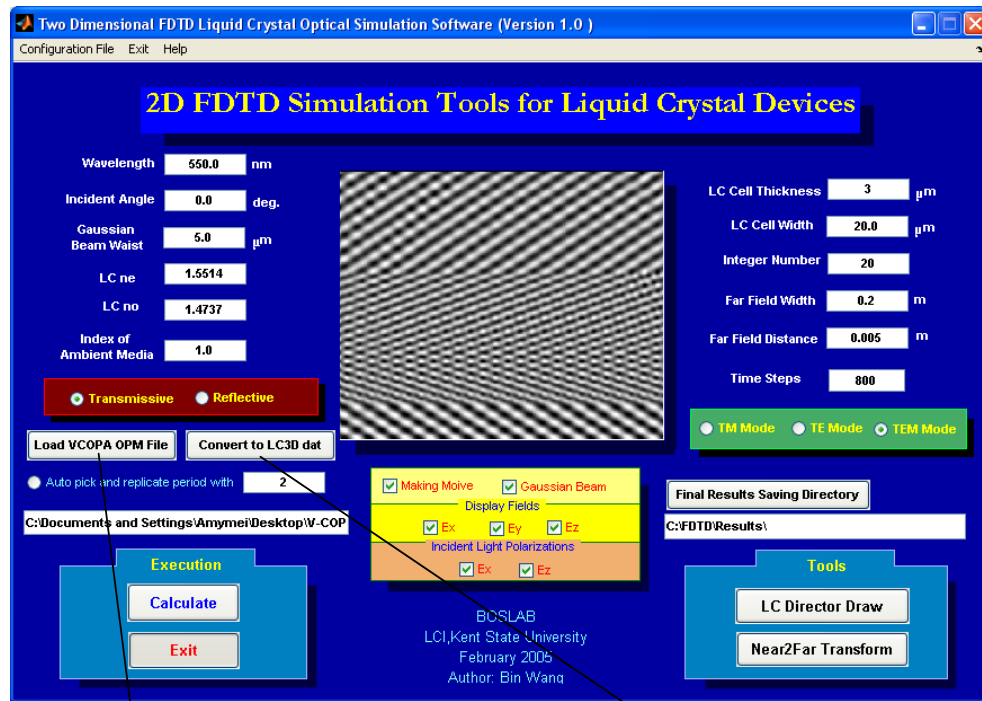
(a)

(b)

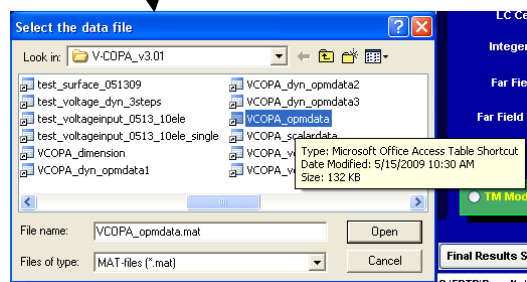


(c)

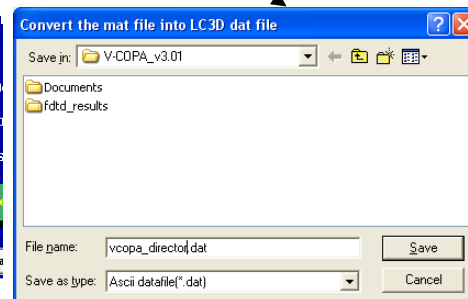
Fig. 7.24 (a) Near field intensity pattern of VCOPA; (b) Near field phase profile of VCOPA; (c) Far field intensity pattern of VCOPA



(a)



(b)



(c)

Fig. 7.25 (a) FDTD subroutine programmed by Dr. Bin Wang

(b) load the .mat file from VCOPA v3.0

(c) convert the .mat file to .dat file that can be used in FDTD

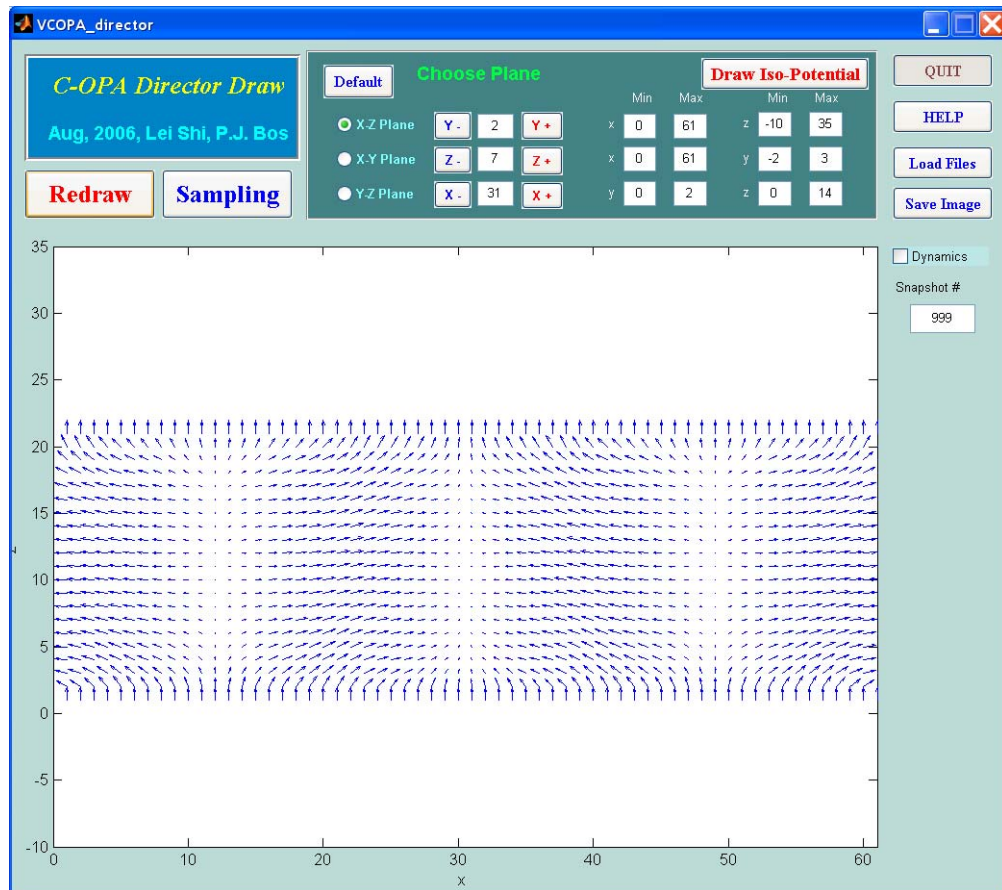


Fig. 7.26 LC director draw of VCOPA v3.0 program

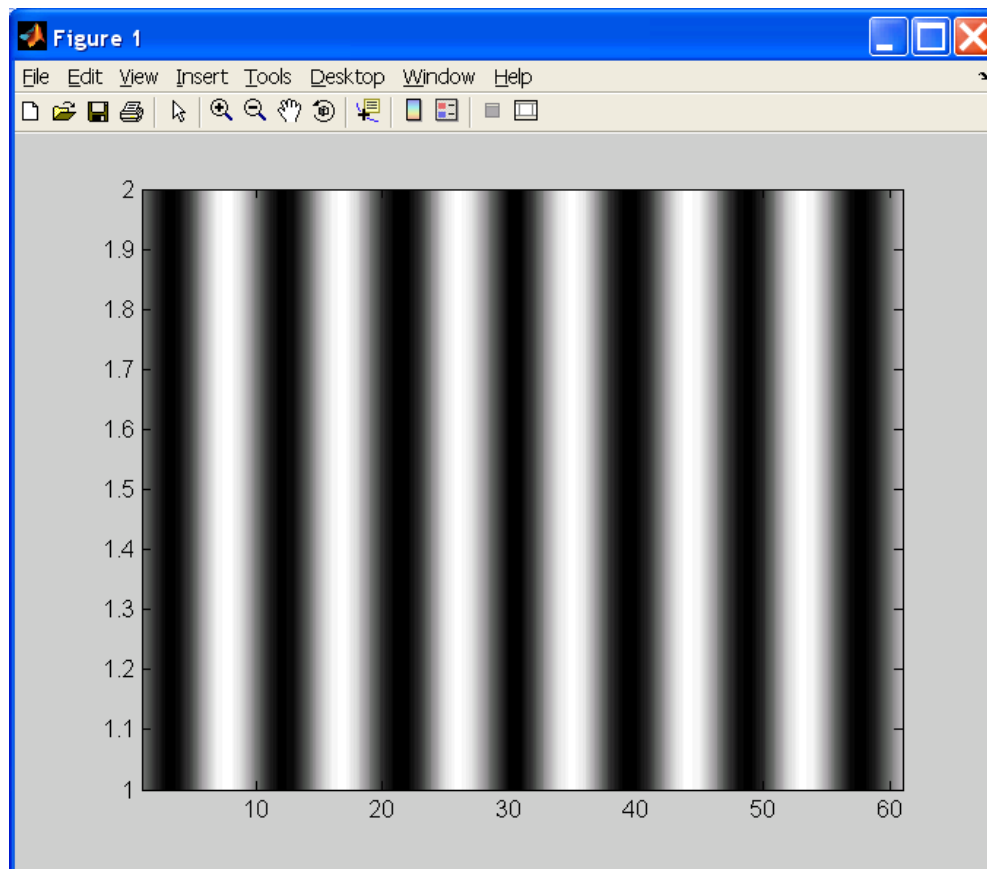


Fig. 7.27 Polarized optical microscopy draw of VCOPA v3.0

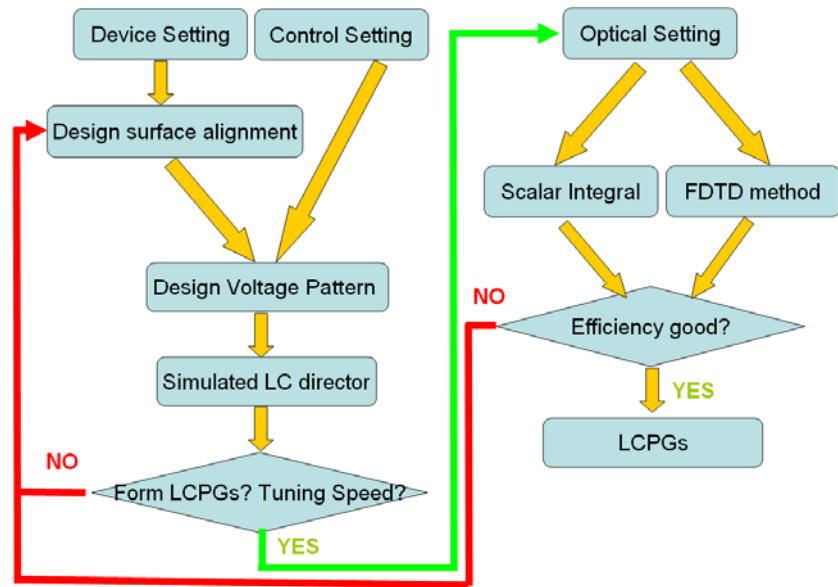


Fig. 7.28 Flow chart diagram of VCOPA simulation procedures

REFERENCES

- ¹ K. Hirabayashi, T. Yamamoto, and M. Yamaguchi, Appl. Opt. **34**, 2571 (1995).
- ² E. A. Watson, D. T. Miller, and P. F. McManamon, SPIE **3633**, 216 (1999).
- ³ B. D. Duncan, P. J. Bos, and V. Sergan, Opt. Eng. **42**, 1038 (2003).
- ⁴ P. F. McManamon, E. A. Watson, T. A. Dorschner, and L. J. Barnes, Opt. Eng., **32**, 2657 (1993).
- ⁵ J. Thomas, M. Lasher, Y. Fainman, P. Soltan, Proc SPIE **3131**, 124 (1997).
- ⁶ P. F. McManamon, T. A. Dorschner, D. L. Corkum, L. J. Friedman, D. S. Hobbs, M. Holz, S. Liberman, H. Q. Nguyen, D. P. Resler, R. C. Sharp, and E. A. Watson, Proc IEEE **84**, 268 (1996).
- ⁷ L.F. DeSandre, Proc SPIE, **1625**, 62 (1992)
- ⁸ Federal Standard 1037C, Telecommunications: Glossary of Telecommunication Terms, August, 1996
- ⁹ L.J. Hornbeck, and W.E.Nelson, OSA Technical Digest Series, vol 8, 107 (1988)
- ¹⁰ L.J. Hornbeck, Spatial Light Modulators and Applications III, SPIE Critical Reviews, vol 1150, 86-102 (1989)
- ¹¹ J.B.Sampsell, "The Digital Micromirror Device", 7th ICSS&A, Yokohama, Japan (1993)
- ¹² D. M. Bloom, Proc. SPIE **3013**, (1998)
- ¹³ W. Kulcke, et. al., IBM Journal of. Research and Development, v8, 64-67, (1964)
- ¹⁴ R. A. Soref and D. H. McMahon, Applied Optics, v 5, 425-434, (1965)

- ¹⁵ T. J. Nelson, *Bell Syst. Tech. J.* **43**, 821-845, (1964)
- ¹⁶ U. J. Schmidt, *Phys. Lett.* **12**, 205-206, (1964)
- ¹⁷ Motamedi M.E., Wu M.C., Pister K.S.K., *Opt. Eng.*, **36**, no. 5, 1282-97(1997).
- ¹⁸ Motamedi M.E., Sangtae Park, Wang A., Dadkhah M., Andrews A.P., Marcy H.O., Khoshnevisan M., Chiou A.E., Huhn R.J., Sell C.F., Smits J.G, *Opt. Eng.*, **36**, no.5, 1346-53(1997).
- ¹⁹ Kurzweg T.P., Martinez J.A., Levitan S.P., Shomsky M.T., Marchand P.J., Chiarulli D.M., *J. Modeling Simu. Microsyst.*, **2**, no. 1, 21-34(2001).
- ²⁰ Milanovic V., Last M., Pister K.S.J., *IEEE Photonics Technol. Lett.*, **15**, no. 2, 245-7(2005).
- ²¹ P.F.McManamon, T.A.Dorschner, D.L.Corkum, L.J.Friedman, D.S.Hobbs, M.Holz, S.Liberman, H.Q.Nguyen, D.P.Resler, R.C.Sharp, and E.A.Watson, *Proc. IEEE*, **84**(2), 268-298(1996).
- ²² D.M.Burns et al., *SPIE* **3131**, 99-110(1997)
- ²³ D.Resler, D.Hobbs, R.Sharp, L.Friedman, T.Dorschner, *Opt. Lett.*, **21**, No.9, 689-611(1996).
- ²⁴ E.A.Watson, *Opt. Eng.* **32**(11), 2665-2670(1993)
- ²⁵ P.F. McManamon, and E.A. Watson, *SPIE* **3131**, 90-98(1997)
- ²⁶ H. Dammann, *Optik*, **31**, 95 (1970)
- ²⁷ S. Pancharatnam, in *Proceedings of the Indian Academy of Sciences*, vol **XLI**, no. 4, sec. A, 137, (1955)
- ²⁸ U. Schmidt and W. Thust, U.S. Patent 3 572 895, Dec. (1986).

- ²⁹ H. Meyer, D. Riekman, K. P. Schmidt, U. J. Schmidt, M. Rahlff, E. Schrbder, and W. Thust, *Appl. Opt.*, vol. 11, no. 8, pp. 1932–1736, Aug. 1972.
- ³⁰ M. A. Karim, D. Cook, and P. F. McManamon, Tech. Dig. 1988 Annul Meeting Opt. Soc. Amer., Santa Clara, CA, pp. 118, Oct (1988)
- ³¹ C. M. Titus, P. J. Bos, and O. D. Lavrentovich, *Proc. SPIE*, 1999, v. 3633, pp. 244.
- ³² M. Honma, and T. Nose, *Jpn. J. Appl. Phys.* **44**, 287 (2005).
- ³³ G. P. Crawford, J. N. Eakin, M. D. Radcliffe, A. C. Jones and R. A. Pelcovits, *J. Appl. Phys.* **98**, 123102 (2005).
- ³⁴ M. J. Escuti, and W.M. Jones, *SID Symposium Digest*, **37**, 1443 (2006).
- ³⁵ L. Shi, P. F. McManamon, P. J. Bos, *J. Appl. Phys.* **104**, 033109 (2008)
- ³⁶ J.R. Shi, Doctoral Dissertation, Kent State University (2005).
- ³⁷ E. Hecht, “*Optics*”, 2nd ed, Addison-Wesley, Reading, MA, 459-463, (1987).
- ³⁸ Robert Guenther, “*Modern Optics*”, John Wiley & Sons, NY, 345-346 (1990).
- ³⁹ L. Nikolova, T. Todorov, *Optica Acta*, vol. 31, pp. 579-588 (1984)
- ⁴⁰ J. Tervo, J. Turunen, *Opt. Lett.*, Vol. 25, pp. 785-786 (2000)
- ⁴¹ W. H. de Jeu, *Physical properties of liquid crystalline materials*, Gordon and Breach Science Publishers Ltd., 1980.
- ⁴² M. Born, and E. Wolf, “*Principles of Optics*”, Oxford: Pergamon, 1970.